Circuits and Systems
Mekelweg 4,
2628 CD Delft
The Netherlands
http://ens.ewi.tudelft.nl/

CAS-MS-2014-09

M.Sc. Thesis

Long-range 3D Range Detector Based on Time-correlated Single-photon Counting

Dali Zhang

Abstract

Three-dimensional (3D) range detectors enabling 3D computer vision is now popular in automotive industry. With their participation, automobile safety has been further enhanced, autonomous driving has become realizable. Time-correlated single-photon counting (TCSPC) technique utilizing complementary metal-oxide semiconductor (CMOS) single photon detectors (SPDs) and time-to-digital converters (TDCs) embodies the proper participant of automotive 3D vision, with low power consumption, low cost, high speed, high robustness, small size, and portability.

In this thesis, a TCSPC 3D range detector for automotive application was studied and modeled. The model covered all main components of a TCSPC system, including the TCSPC range detection process, the signal, and the noise. It was designed to predict the behavior of TCSPC systems and help future designers optimize the performance in accordance with the targeted application.

To verify the model, an experimental setup was designed, implemented, and characterized. The setup consists of a data acquisition system, data processing procedures, and an optical-mechanical system. Measurements performed using the setup have confirmed that the model was designed correctly. For further exploration, range detections from 0.2 m to 60 m were carried out.

Long-range 3D Range Detector Based on Time-correlated Single-photon Counting

Modeling, Characterization, and Implementation

THESIS

submitted in partial fulfillment of the
requirements for the degree of

MASTER OF SCIENCE

in

MICROELECTRONICS

by

Dali Zhang
born in Harbin, P.R.China

This work was performed in:

Circuits and Systems Group
Department of Microelectronics & Computer Engineering
Faculty of Electrical Engineering, Mathematics and Computer Science
Delft University of Technology

Delft University of Technology

Delft University of Technology
Department of
Microelectronics & Computer Engineering

The undersigned hereby certify that they have read and recommend to the Faculty of Electrical Engineering, Mathematics and Computer Science for acceptance a thesis entitled **"Long-range 3D Range Detector Based on Time-correlated Single-photon Counting"** by **Dali Zhang** in partial fulfillment of the requirements for the degree of **Master of Science**.

Dated: 29 August 2014

Chairman: _____
prof.dr.ir. Edoardo Charbon

Advisor: _____
prof.dr.ir. Edoardo Charbon

Committee Members: _____
assoc. prof. Ryoichi Ishihara

_____
dir. Lucio Carrara

Abstract

Three-dimensional (3D) range detectors enabling 3D computer vision is now popular in automotive industry. With their participation, automobile safety has been further enhanced, autonomous driving has become realizable. Time-correlated single-photon counting (TCSPC) technique utilizing complementary metal-oxide semiconductor (CMOS) single photon detectors (SPDs) and time-to-digital converters (TDCs) embodies the proper participant of automotive 3D vision, with low power consumption, low cost, high speed, high robustness, small size, and portability.

In this thesis, a TCSPC 3D range detector for automotive application was studied and modeled. The model covered all main components of a TCSPC system, including the TCSPC range detection process, the signal, and the noise. It was designed to predict the behavior of TCSPC systems and help future designers optimize the performance in accordance with the targeted application.

To verify the model, a experimental setup was designed, implemented, and characterized. The setup consists of a data acquisition system, data processing procedures, and an optical-mechanical system. Measurements performed using the setup have confirmed that the model was designed correctly. For further exploration, range detections from 0.2 m to 60 m were carried out.

Acknowledgments

I wish to express my gratitude to my professor, Edoardo Charbon for offering me the opportunity of working on this interesting project. His continued support and encouragement motivated me thorough the whole project. His research methodology and ways of thinking strongly affected my career. I would also like to appreciate the time and effort that Dr. Shingo Mandai, Chockalingam Veerappan, and Esteban Venialgo spent with me on this project. This thesis would not have been successful without their timely help.

I would also like to thank Augusto Carimatto, Pengfei Sun, Ivan Antolović, Chao Zhang, Myung-Jae Lee, Masahiro Akiyama, Tim Gong, Claudia Damiani, and Harald Homulle. With their presence, the group becomes such a nice team that I was proud and happy to work as a member.

I would like to thank Antoon Frehe for the computing facilities and support at the beginning of the thesis. I would also like to thank Andre Bossche, Minaksie Ramsoekh, and Joanna Daudt for their help in all the paperwork and arrangement.

I would like to use this opportunity to thank my friends Kaixiang Zhang, Cheng Chen, Jianjun Tang, Si Xiao, Junjie Liu, Yanshuang Jiang, Miao Zhang, Hailin Li, Luis Robles, Derk van Dieten, Alper Nizamoğlu, João Silva, and Bishnu Patra for the joy and support they gave me during the course of thesis.

I would like to thank Junyi Zhang for the proofreading of my thesis and the happiness she brought.

Finally, I would like to thank my grandma, my parents, my cousins, and all my family members back in China for their support and encouragement throughout my course of study at TU Delft.

Dali Zhang B.Eng.
Delft, The Netherlands
29 August 2014

Contents

List of Figures

List of Tables

1 Introduction

Human beings start developing binocular three-dimensional (3D) vision from an early age. With the development of visual cortical neurons and the help of experience and knowledge, we are able to obtain 3D information instinctively [1]. However, in the age of information, so many images are being generated that we cannot afford reading and analyzing all of them manually. As a result, computer vision is introduced to automate the acquisition and analysis of images. Unfortunately, computers have a number of difficulties when acquiring 3D information from normal two-dimensional (2D) images. To avoid ambiguity caused by the loss of depth information, 3D rangefinders, or 3D image sensors, were introduced to computer vision systems, which enable computers to capture 3D structure of senses and objects [2].

From a historical point of view, 3D image sensors have been used for centuries. However, the practical development of the electro-optic 3D image sensors system that we are using today started in the 1970s. After the initial stage of research in the 1980s and the demonstrations of applications during the 1990s, now we can find numerous commercialized 3D image sensors in the market, such as single-point laser scanners, slit scanners, pattern projection scanners, and time-of-flight(TOF) systems [3]. Applications of 3D image sensors can be found in automotive industry [4], medical instruments [5], biometric equipment [6], security facilities [7], entertainment products [8], archeology research [9], and many other fields.

This thesis explains the theory, the model, the characterization, and the implementation of a TOF 3D range sensing system based on Time Correlated Single Photon Counting (TCSPC) principle.

A mathematical model of TCSPC range detection system is built and verified with measurements. An electro-optical system based on a single photon detector (SPD) array manufactured in 0.35 μm complementary metal-oxide semiconductor (CMOS) technologies is implemented as the basic platform of this project. Short-distance and Long-distance range detection are performed to characterize and verify the performance of the system.

In this introductory chapter, a brief overview of common implementations of 3D imaging systems is given at the beginning in Section 1.1. Later, in Section 1.2, we analyze the targeted application of this project and give the motivation of utilizing the TCSPC principle. Afterwards, we give a brief introduction to state-of-the-art TCSPC long range sensing systems in Section 1.3. At the end, we will present the main contributions of this project and the overview of this thesis in Section 1.4 and Section 1.5.

1.1 Overview of 3D Imaging System Implementations

Generally speaking, 3D imaging systems are systems that project/acquire electromagnetic energy onto/from an object and acquire the 3D shape information of the object by recording the transmitted/reflected energy [2]. A relatively high-number of technologies are being used to implement 3D imaging systems nowadays. According to the basic physical principles involved, different classifications exist [10]. In this project, we differentiate between passive and active methods for 3D imaging.

Passive 3D imaging acquires 3D information from the ambient-lit scene only, without the assistance of any extra light source. To some extent, passive 3D imaging techniques are 2D imaging techniques with extra set-ups and algorithms that can help the system extract 3D information from standard 2D images. Basically, passive 3D imaging technology can be categorized as multiple view approaches and single view (or monocular) approaches[10, 2, 11].

In contrast to passive 3D imaging, active 3D imaging acquires 3D information with the help of additional light sources. The additional optical input triggered by controlled signal sources provides the system with direct information of the shape of the target. The three most popular commercially available active 3D imaging techniques are the time-of-flight, the interferometry and the triangulation[2]. Based on the review of 3D imaging development from 1984 to 2004 in [3] and the state-of-the-art study in [11], some widely used 3D imaging systems are summarized in Table 1.1.

	Principle	Category	Acquisition	Information
Laser Trangulators	Triangulation	Active	Direct	Range
Structured Light	Triangulation	Active	Direct	Range
Stereo Vision	Triangulation	Passive	Direct	Range
Photogrammetry	Triangulation	Passive	Direct	Range
TOF	Time Delay	Active	Direct	Range
Interferometry	Time Delay	Active	Direct	Range
Moir Fringe	Monocular	Active	Indirect	Range
Shape from Focusing	Monocular	Both	Indirect	Range
Shape from Shadows	Monocular	Active	Indirect	Range
Texture Gradients	Monocular	Passive	Indirect	Surface
Shape from Shading	Monocular	Active	Indirect	Surface
Shape from Photometry	Monocular	Active	Indirect	Surface

Table 1.1: Classification of Common 3D Imaging Techniques

These 3D imaging techniques are based on the principle of triangulation, time delay, or the use of monocular images. With the different 3D information acquisition, some techniques acquire range data directly, while others acquire range data indirectly from monocular images. The final information output of these techniques is either range data or surface orientation data. Determined by the targeted application of this project, we will focus on the TOF technique in the following sections.

1.2 Motivation of the Choice

The targeted application of the 3D imaging model and system built in this project is automotive driver assistance system. To fulfill the requirements and limits of this targeted application, one particular technique is chosen from numerous approaches of TOF 3D imaging, known as TCSPC.

1.2.1 The Application

Driven by endless demands from customers and society, the pursuit of perfect automobile safety system has never stopped. One of the most important components of current and future automobile safety system is called the Advanced Driver Assistance Systems (ADAS).

ADAS is designed to help the driver. It works as a co-driver who can enhance drivers senses, improve driver-vehicle interactions, provide early warning, give optimal suggestions, etc. Enhancement in driving safety, road safety, traffic efficiency and driving experience is to be achieved with its presence [12, 13].

As a co-driver, ADAS needs to collect distance information of unpredictable surrounding environment, including barriers, other vehicles, pedestrians, etc. Several techniques can be employed for this function, such as global positioning system (GPS), radio detection and ranging (Radar), sound navigation and ranging (Sonar), passive 3D imaging, light detection and ranging (Lidar), etc. Advantages and drawbacks of these techniques are shown in Table 1.2 [14].

For an ADAS system, distance measurement is performed when the vehicle is moving at low or high speed. So high speed measurement is required. As a result, GPS is not a proper option. A vehicle runs in all kinds of environment, day and night, so the detector should be robust to environment, which means that neither Sonar nor passive 3D imaging systems is the best choice. For Radar systems, the risk of ghost object makes it not suitable for long distance application on road. Furthermore, compared with Lidar systems, Radar systems have much higher cost. Finally, it turns out that Lidar is the most suitable candidate for ADAS application.

Lidar can be classified as a kind of active 3D imaging systems. The basic principle behind can be Doppler Effect, TOF measurement, etc. In this project, we will focus on a Lidar system based on TCSPC principle and solid-state imaging sensor.

1.2.2 Introduction to TCSPC System

A TCSPC 3D rangefinder often consists of four main componentsthat is, an illumination source, a SPD, a time difference detector, and a data processor. The basic setup of a TCSPC rangefinder is shown in Figure 1.1.

In this project, a similar set-up is implemented. A blue pulse laser is used as the illumination source. An array of 128 single-photon avalanched diodes (SPADs), or Geiger-mode avalanche photodiodes, is used as the SPD. Output of each SPAD is connected to the start signal input of a time-to-digital converter (TDC) that serves as the time difference detector. Control signal is given by a field-programmable gate array (FPGA). Signal processing is performed on a personal computer (PC).

Technology	GPS	Radar	Sonar	Passive 3D	Lidar
Range	Global	150 m	2 m	25 m	25 km
Advantages	Global availability	Reliability, accuracy, any weather	Under water availability	Low cost High availability	Accuracy Low cost Recognition Night-vision
Drawbacks	Inaccurate Slow	High cost Absorbents Ghost object Limited FOV	Absorbents Weather	Weather Low accuracy	Ambient Light Limited FOV

Table 1.2: Commonly used technologies for ADAS

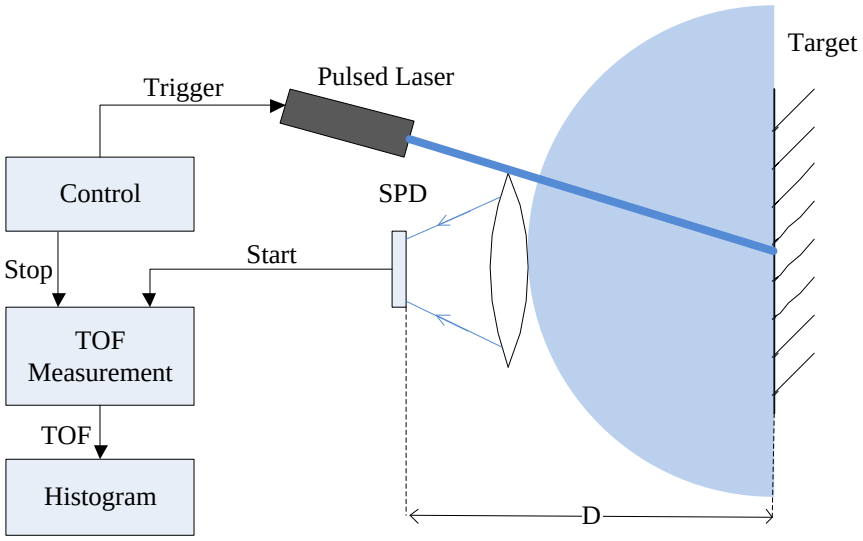

Figure 1.1: Basic Set-up of a TCSPC Rangefinder

The basic principle of TCSPC process is shown in Figure 1.2. For TOF measurements in photon-starving mode, the probability that one SPAD detects a photon in one measurement is far less than one. For the same sensing point, reflected photons generated by the laser will arrive at the SPAD at a same time in each detection cycle. In other words, arrival of signal photons is time-correlated. After a large amount of detections, a histogram can be generated based on the TOF results. With the help of the histogram, range detection can be achieved with a depth resolution beyond the limit of the TDC resolution and timing jitter of the system, which distinguishes TCSPC from direct TOF measurement.

The basic principle of utilizing TOF histogram provides TCSPC systems with not only the benefit of improved depth resolution, but also the high robustness against shot noise. This is a very important advantage, especially for the application of this project, in which long distance measurement should be reliably performed with unpredictable signal attenuation and strictly limited laser power (within eye-save region). However, potential disadvantages exist as well, including the following: limited spectral range of

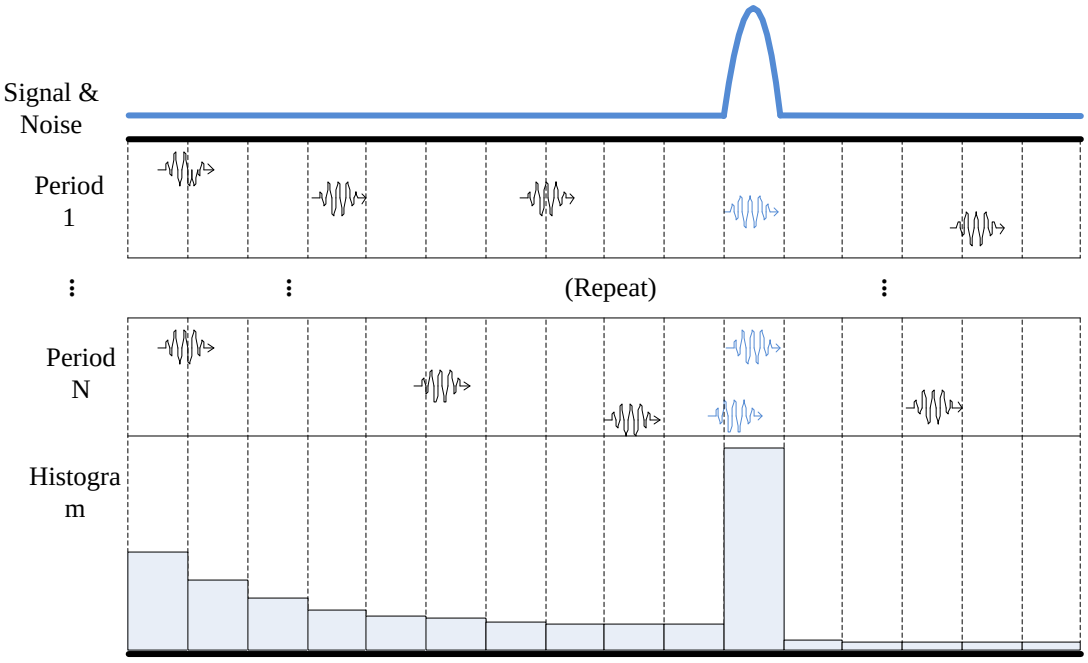

Figure 1.2: TCSPC Principle

practical SPDs; detector dead time, during which the SPD is shut down to reset after detecting an event; and issues regarding solar background events providing potential false alarms [15].

Key performance values of long-range TCSPC systems are the dynamic range, the depth resolution, and the detection speed. At present, the two most significant issues that limit these performance values are the optical signal-to-noise ratio (SNR) and the total jitter of the system.

Optical SNR affects the performance of a TCSPC system. It is initially determined by the signal photon input and the sum of all noise inputs of the SPD. Factors that affect the signal photon input are the total power of each laser pulse, the laser jitter, the reflectivity of the target, the distance, and the attenuation throughout the optical path. For noise input, two main contributors are the ambient noise and dark count (DC).

Total jitter of a TCSPC system strongly influences its depth resolution. Typical jitter of a TCSPC system is at the level of hundred picoseconds. Main sources of the total jitter are the SPD, the TDC, the TCSPC module, the laser source, and the synchronization signal of the laser [16]. Concerning that the resolution of TDC nowadays is at the level of picosecond [17] or tens of femtoseconds [18], the jitter is currently the main obstacle that blocks further improvement in depth resolution.

1.3 State-of-the-Art Long-Range TCSPC Systems

Thanks to the development of CMOS SPDs and TDCs, recent years have witnessed an acceleration in performance improvement of solid-state long-range TCSPC rangefinder.

Some of the state-of-the-art research results are shown in Table 1.3.

	Unit	Chen et al., Appl.Opt. 2013 [16]	McCarthy et al., Op.Ex. 2013 [19]	Ito et al., Ph.J, 2013 [20]	Niclass et al., JSSCC 2014 [21]
SPD	-	SNSPD [1]	SNSPD	SPAD	SPAD
Photon Detection Efficiency	%	3	18	3	2.1
Illumination Wavelength	nm	1550	1560	870	870
Illumination Repetition Rate	MHz	20	50	0.6	0.133
Illumination Power	mW	2	<12	<175	21
Illumination Power	mW	2	2	75	21
Pulse Width	ps	<1	<1	4000	4000
Background Light	klux	<10 [2]	2 [3]	10	70
Frame Rate	fps	<0.0001	0.0021	10	10
Distance Range	m	155	4400	25	100
Relative Precision	%	0.000035	0.000057	0.58	0.14

Table 1.3: Comparison of State-of-the-Art Solid-State TCSPC Systems

TCSPC systems presented in [16] and [19] are research demonstrations for the application of SNSPD. The main goal of using SNSPD is to reduce the total jitter of the system, which then produces high depth precision. Jitter of a TCSPC system can be summarized as the following equation:

$$Jitter_{system} = \sqrt{Jitter_{SNSPD}^2 + Jitter_{TCSPC}^2 + Jitter_{Laser}^2 + Jitter_{SYN}^2}. \quad (1.1)$$

The application of SNSPD (superconducting at temperature of 3 K) successfully reduces the total jitter of the system in [16] and [19], i.e. 26.8 ps and 98 ps respectively. In addition, both of them utilizes long-wavelength femtosecond laser. The choice of wavelength keeps their system away from the peak of solar spectrum. The femtosecond-level pulse width increases the time-correlation of their signal photons. As a result, compared with [20] and [21], they have much higher signal-to-background light ratio (SBR). Furthermore, long exposure time (10 s per pixel in [16] and 2 s per pixel in [19]) is applied to each single pixel of the SNSPDs. In summary, systems reported in [16] and [19] have high depth precision and detection range, but the high cost and long detection time keep them away from practical applications.

In contrast, in [16] and [19], systems in [20] and [21] are targeted on realistic applications. For TCSPC applications, the most important factor that affects performance of the system is the SBR (or optical SNR). It determines the detection time, the distance range, and the precision of the system. To improve system performance, several approaches exists. The most direct approach is to increase the signal power, however,

[1] Superconducting nanowire single-photon detector.
[2] Not mentioned in [16], optical band pass filter with Full Width Half Maximum of 6.47 nm is used.
[3] Not mentioned in [19], estimated from photos and descriptions.

considering the safety issue, it is strictly limited. On the contrary, it is also possible to reduce the background light power. This can be achieved by utilizing an optical filter and by choosing a particular wavelength. Another approach is to enhance the robustness of the system in low SBR environment, as reported in [20] and [21].

In [20], synchronized gating approach is utilized. As a result, pixels do not integrate background light when the target is not illuminated. Moreover, on top of time-gating technique, [20] applies micro-electromechanical-system (MEMS) mirrors in their design. With the driving signal synchronized with the laser diode (LD) and the sensors, the gating approach is enhanced in such a way that each single pixel is activated only when the corresponding point on the target is illuminated by the LDs.

In [21], TOF macro-pixels (also known as silicon photon multipliers) are employed as the SPD. The TOF macro-pixel comprises 24 SPADs. It generates TDC trigger signal only when two or more than two SPADs are fired within a time interval that equals to the duration of the laser pulse. In such a way, detections caused by the time-uncorrelated ambient light are suppressed. Meanwhile, an optical band pass filter and a digital FIR filter are applied to further improve the system performance against low SBR.

1.4 Contribution

This thesis project focuses on the theory, the model, the characterization, and the implementation of a TCSPC range detector with a targeted application in automotive industry.

The verified mathematical model for design assistance provides future designers with a clear orientation of system optimization.

The experience and results acquired during characterization can be applied as user-view feedback of the chip for future application-oriented design improvements.

The experimental outcomes of range detection verify the performance of the system setup and the algorithm.

As an application-oriented project, aerial view of TCSPC ranging system and system design methodology were applied. The main contributions of this thesis project are:

- Summary and verification of pervious work.
- Development of practical and flexible mathematical models for long-range TCSPC range detector systems.
    1. Theoretical model of TCSPC process.
    2. Random model based on TCSPC principle.
    3. Theoretical modeling of the signal and noise of TCSPC system.
    4. Qualitative performance prediction model.
    5. Simulation and measurement verification of the models.
    6. Special application-oriented model applications.
- Development of data acquisition (DAQ) and processing software based on MATLAB.

1. DAQ for different experiments.
2. TDC characterization based on outputs.
3. Artifact cancellation and LSB calibration.
4. Range information extraction.

- Design and implementation of a TCSPC range detector.
- Suggestions for future design from users point of view.

1.5 Overview

This thesis can be divided into two parts. The first part describes the development and verification of the mathematical model. The second part presents the implementation, characterization, and performance verification of the range detector setup. Finally the results and experience acquired throughout the project are summarized.

Organization of the thesis is as follows: Chapter 2 presents the study, development, simulation, and measurement verification of the mathematical model. Chapter 3 describes the structure and characterization results of the sensor used in this project. Chapter 4 reports the design of the setup, both the hardware design and software design. Measurement results and algorithms used in range detection are reported in Chapter 5. Finally, Chapter 6 concludes the thesis, providing summary of the results, along with possible future directions.

2 Modeling of TCSPC System

The three most crucial components of a TCSPC system are the system set-up, the input signal, and the noise. The goal of this chapter is to build a mathematical model that can predict the performance of TCSPC systems qualitatively. The model can be utilized at the beginning stage of system design, to help designers determine targeted technical indexes according to the analysis.

The organization of this chapter is the following:

The mathematical model of TCSPC process is introduced in Section 2.1. Random simulation, theoretical simulation, and model verification based on real measurement are shown in Section 2.2. Afterwards, in Section 2.3 are the model and simulation of the signal, including signal source and signal transmission. Model and simulation of the noise are described in Section 2.4. In Section 2.5, a model that can qualitatively predict the performance and feasibility of a TCSPC system is built. In Section 2.6 and Section 2.7, simulations of special applications of the model are presented. Finally, in Section 2.8, this chapter is concluded.

2.1 TCSPC Process Modeling

In 2008, Cristiano L. Niclass built a mathematical model of short range time-of-flight 3D imaging based on TCSPC principle in his Ph.D thesis, i.e. [10]. The model is easy to use and was verified with measurements. In this section, we are going to improve the model, and build a new model for long range TCSPC process.

2.1.1 Study of Previous Work

The principle of TCSPC process has been discussed in Section 1.2.2. The detector detects the arrival time of all the photons without distinction. The detection follows Poisson distribution, but after the first detection, the detector will be inaccessible for a particular period of time. After large amount of detections, a histogram of photon arrival time will be generated. The TCSPC system then calculates the TOF of signal photon base on the histogram.

Assume that a perfect laser generator generates Gaussian laser pulses at a specific wavelength λ, with perfect collimation. The target is a perfect laser mirror with 100% reflectivity. No refraction effects or scattering is occurring on the TOF path. The power distribution of the reflected light at a SPAD is described in time as

$$P_s(t) = \frac{Q_p}{\sqrt{2\pi\sigma_\tau}} exp - \frac{(t - TOF)^2}{2\sigma_\tau^2}, \tag{2.1}$$

with Q_p the total energy of one pulse, σ_τ standard deviation of the laser pulse, and TOF the time-of-flight determined by the distance between the laser and the target.

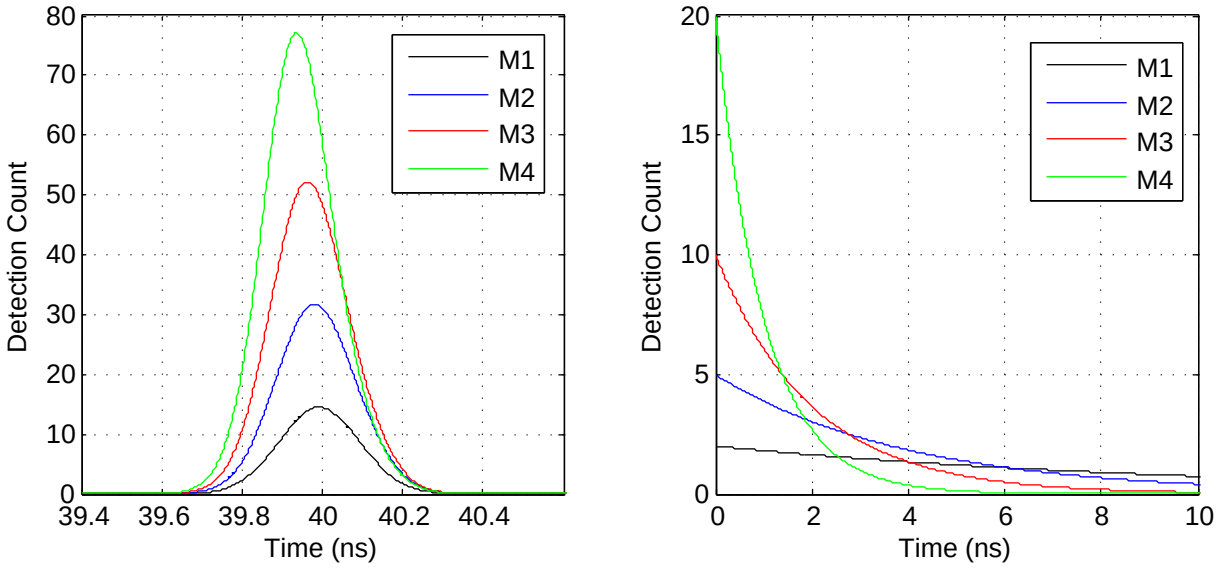

Figure 2.1: Distortion Due to TCSPC Process, Normally Distributed Signal Input and Uniformly Distributed Signal Input (M1<M2<M3<M4)

If the SPAD has a photon detection efficiency (PDE) of η_{SPAD} at wavelength λ, the expected number of photons detected per pulse is

$$M = \frac{Q_p}{Q_{photon}} = \frac{\lambda Q_p}{hc}\eta_S PAD \tag{2.2}$$

where h is the Plank constant and c is the speed of light.

Similarly, cumulative number of photons (within a pulse) at time t is

$$M_t = \frac{Q_t}{h\nu} = M\frac{Q_t}{Q_{pulse}} = \frac{M}{2}[1 + erf(\frac{t - TOF}{\sqrt{2}\sigma_\tau})], \tag{2.3}$$

with Q_t the total optical energy at time t and Q_{pulse} the total energy in a pulse.

According to the application, the TCSPC system runs in photon-starving mode, in other words, $M_t \ll 1$. Furthermore, determined by the structure of our SPAD array, only the first photon that triggers the SPAD can be detected, which means that n, the number of photon detection, is either 1 or 0. Therefore, detected optical power at time t is as follows,

$$\hat{P}_s(t) = \sum_{n=0}^{\infty} P_s(t)\frac{M_t e^{-M_t}}{n!} = P_s(t)e^{-M_t}(1+M_t) \approx P_s(t)(e^{-M_t}) = P_s(t)e^{-\frac{1}{2}M[1+erf(\frac{t-TOF}{\sqrt{2}\sigma_\tau})]}. \tag{2.4}$$

The approximation in Equation 2.4 introduces a distortion to the detected power distribution and the final TOF histogram.

As shown in Figure 2.1, the distortion caused by the TCSPC process becomes larger

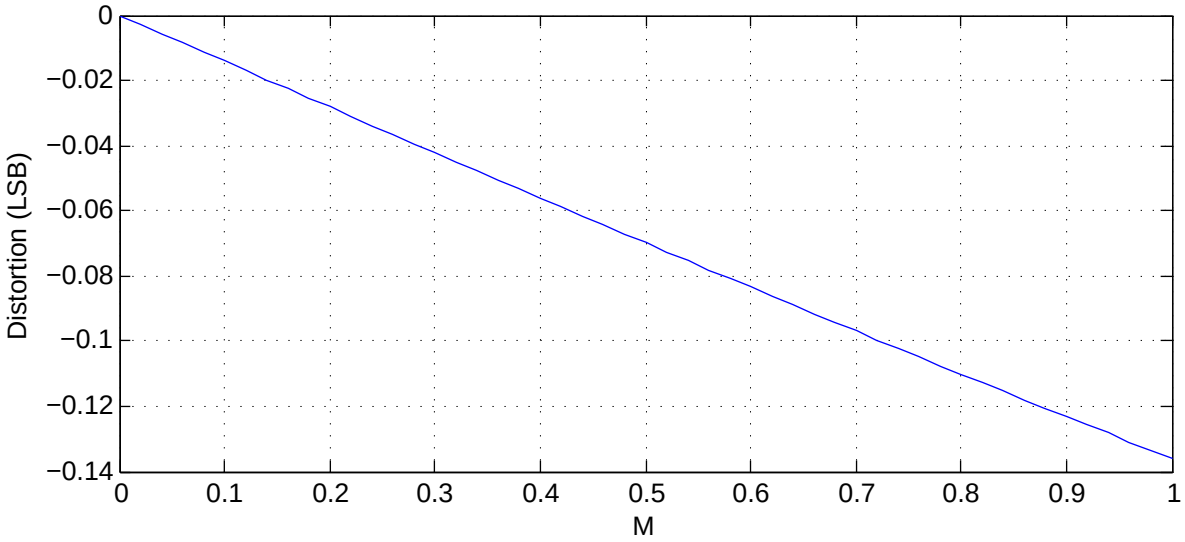

Figure 2.2: Peak Position Distortion

when M increases. By setting

$$\frac{d\hat{\mathrm{P}}_{\mathrm{s}}\left(\mathrm{t}\right)}{dt}=\frac{d\mathrm{P}_{\mathrm{s}}\left(\mathrm{t}\right)}{dt}\mathrm{e}^{-\mathrm{M_t}}+\mathrm{P}_{\mathrm{s}}\left(\mathrm{t}\right)\mathrm{e}^{-\mathrm{M_t}}(\frac{M}{\sqrt{\pi}}e^{-(\frac{t-TOF}{\sqrt{2}\sigma_t})^2})=0. \tag{2.5}$$

We have

$$\frac{t_{peak}-TOF}{\sigma_\tau^2}+\frac{M}{\sqrt{\pi}}e^{-\left(\frac{t_{peak}-TOF}{\sqrt{2}\sigma_t}\right)^2}=0. \tag{2.6}$$

It is clear that $t_{peak}=TOF$ holds only when $M=0$, and $t_{peak}<TOF$ is always true when $M>0$. By solving Equation 2.6 numerically, the distortion is calculated and plotted in Figure 2.2. However, in real range detection, the LSB of the TDC is strongly affected by the input photon intensity, which causes much worse distortion even with calibration, as shown in Appendix B Figure B.5. Furthermore, in this project, range detection will be performed under photon starving mode. Therefore, the distortion caused by TCSPC process shown in Figure 2.2 is only concerned in this section.

With the help of pixel-level TDC, photon power distribution can be translated into a TOF histogram. Typical histogram of TCSPC process can be divided into two main components, i.e. the contribution from the signal ($\mathrm{s}(\tau)$), and the contribution from background noise ($\mathrm{b}\left(\tau\right)$):

$$h(\tau)=s(\tau)+b(\tau) \tag{2.7}$$

The contribution of the signal to the final histogram at τ is proved to be

$$s(\tau)=\int_0^{\tau+\frac{\Delta t}{2}}s'(\tau)d\tau-\int_0^{\tau-\frac{\Delta t}{2}}s'(\tau)d\tau=\frac{S_RT}{2}[erf(\frac{\tau-TOF+\frac{\Delta t}{2}}{\sqrt{2}\sigma_s})-erf(\frac{\tau-TOF-\frac{\Delta t}{2}}{\sqrt{2}\sigma_s})], \tag{2.8}$$

where S_R is the detection rate of signal photons, T is the total histogram acquisition time, $\triangle$t is the bin width of the histogram, and σ_s=$\sqrt{\sigma_\tau^2+\sigma_{\text{SPAD}}^2+\sigma_{\text{TDC}}^2}$ is the standard deviation of the signal.

Contribution of background noise to the final histogram at the histogram bin of τ is proved to be

$$b(\tau) = \bar{b} = \frac{B_R T \Delta t}{T_0} \tag{2.9}$$

where B_R and T_0 are the detection rate of background noise photons and the duration of pixel illumination cycle, respectively.

Form the final histogram, TOF result can be generated as follows

$$\hat{TOF} = \frac{\sum_{\frac{TOF'}{\Delta t}-N_{HW}}^{\frac{TOF'}{\Delta t}+N_{HW}} h(i\Delta t)\cdot i\Delta t}{\sum_{\frac{TOF'}{\Delta t}-N_{HW}}^{\frac{TOF'}{\Delta t}+N_{HW}} h(i\Delta t)}, \tag{2.10}$$

with TOF$^{'}$ the peak position of the histogram and N_{HW} the half of the preset full width half maximum (FWHM). Standard deviation of $\hat{TOF}$ result is

$$\sigma_{\hat{TOF}} = \frac{1}{\sqrt{TS_R}} \frac{\sqrt{[\frac{(2N_{HW}+1)^2-1](2N_{HW}+1)\Delta t^3}{128\cdot SBR\cdot T_0} + erf[\frac{(2N_{HW}+1)\Delta t}{\sqrt{8}\sigma_s}]\sigma_S^2}}{\frac{(2N_{HW}+1)\Delta t}{SBR\cdot T_0} + erf[\frac{(2N_{HW}+1)\Delta t}{\sqrt{8}\sigma_s}]}, \tag{2.11}$$

with SBR =$\frac{S_R}{B_R}$.

2.1.2 Further Development

The goal of building the mathematical model of the TCSPC process is to generate the TOF histogram based on the information of the signal, noise, and system setup. In [10], Niclass analyzed the histogram in Equation 2.7 and the TCSPC distortion in Equation 2.4 separately. In this project, they are combined together.

Distribution of the power of all detected photons is

$$\hat{P}_s(t) \approx [P_s(t) + \bar{P_B}] \times e^{-[\frac{1}{2}M(1+erf(\frac{t-TOF}{\sqrt{2}\sigma_s}))+\bar{b}t]}, \tag{2.12}$$

with

$$P_s(t) = \frac{Q_p}{\sqrt{2\pi}\sigma_s} e^{-\frac{(t-TOF)^2}{2_s^2}}. \tag{2.13}$$

$\overline{P_B}$ is the average power of background light per unit time.

The difference between the simulation result of [10] and this work is shown in Figure 2.3. It will be proved that the model based on Equation 2.12 fits the real TCSPC detection better in a future section of this chapter with measurement results.

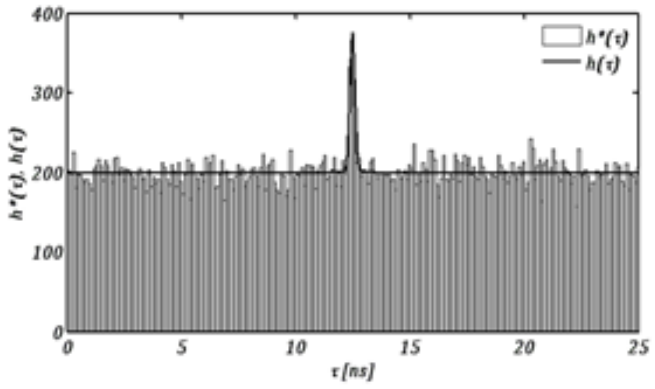

(a) Histogram in [10]

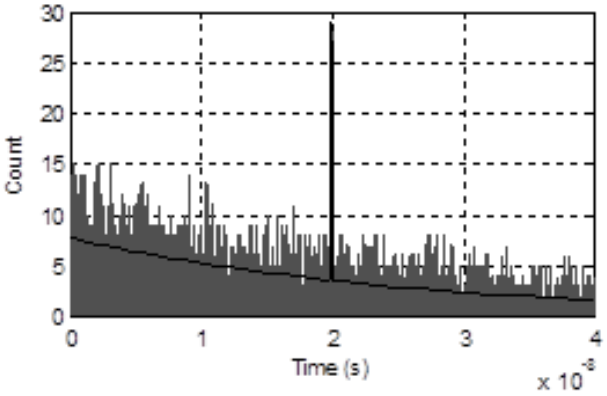

(b) Histogram Based on the Model of Equation 2.12

Figure 2.3: Histograms Based on Different Models

2.2 TCSPC Model Simulation

Simulations in this project are based on the mathematical model of Equation 2.12. Results of both the theoretical and random simulations of a single pixel will be presented in this section.

The simulation is comprised of three steps.

In the first step, ideal detector and environment is assumed, no noise is introduced. In the second step, background noise is involved, while the detector is still ideal. The goal of these steps is to see the performance of an ideal TCSPC process.

In the third step, SPAD and TDC jitter are added to the system. The goal of this step is to build up a realistic TCSPC detection model. The model can be used for range measurement prediction and proof of feasibility.

Data used in all simulations are based on the range sensor reported in [17].

2.2.1 Random Simulation Design

As discussed in the previous section, simulations in this project consist of two parts. The theoretical part is based on Equation 2.12. The random simulation is original work of this project based on the principle of TCSPC process.

The random simulation can be divided in to three parts, i.e. random photon arrival time generation, photon detection process following Poisson distribution, and histogram construction. In the first and second step of the simulation, an ideal TCSPC system model is built. Block diagram of the design of these steps is shown in Figure 2.4.

At the beginning, an ideal random photon arrival time is generated. In the first step, the simulator generates only normally distributed photon arrival time representing signal photon arrival. In the second step, uniformly distributed background photon arrival time is added. To reduce the calculation time, all time values are scaled by TDC resolution.

Since the signal photon and noise photon are uncorrelated and cannot be distinguished by the SPAD, they can be simply summed together in the same histogram. The histogram of arrival time of all photons is generated and multiplied by PDE of the SPAD. The value of each bin of the histogram is then used as the expectation value of the Poisson distributed photon detection process at the same bin. At this moment, we assume that the SPAD can detect as many photons as possible in one measurement. In other words, detection at each time bin of the histogram is independent. In a real TCSPC detection process however, the SPAD can detect only the first photon in each measurement. As a result, only the first non-zero bin of the photon detection histogram is valid.

After N measurements, the first non-zero bin in the histogram of each measurement will be collected and used to build the final histogram.

In the third step of the simulation, non-ideal factors, such as TDC jitter, dark count (DC) and SPAD jitter will be added to the system. Block diagram for the third steps is shown in Figure 2.5. First of all, a set of random arrival time of signal and background are generated, which is basically the same as previous steps. However, in this case, continuous time value has to be used, because of the introduction of jitter.

SPAD jitter and the TDC jitter are uncorrelated. To introduce these forms of jitter, we can add them to the photon arrival time separately. For the SPAD jitter, for simplicity, we assume that it follows normal distribution with a FWHM of 80 ps [22]. Then we generate new photon arrival time that follows normal distribution, with the original photon arrival time as the mean value and FWHM of the SPAD jitter as the FWHM. The same process is used to add TDC jitter.

Afterwards, histogram of the time values is generated. PDE and Poisson distributed photon detection are introduced the same as the former steps. Before generating the histogram of detection, DC should be added. DC is generated by the system itself, it can be affected by the TDC jitter, but not the PDE. In this project, DC of the sensor is low. Moreover, the active time of the sensor is at nanosecond level. So we can ignore the effect of DC. Following processes are the same as those in the first step and second step.

2.2.2 Simulation Results

In this project, all simulations are performed in MATLAB environment.

The simulation implementation of the first step is the same as the design discussed in Section 2.2.1. Flow chart of the MATBAB program for random simulation is shown

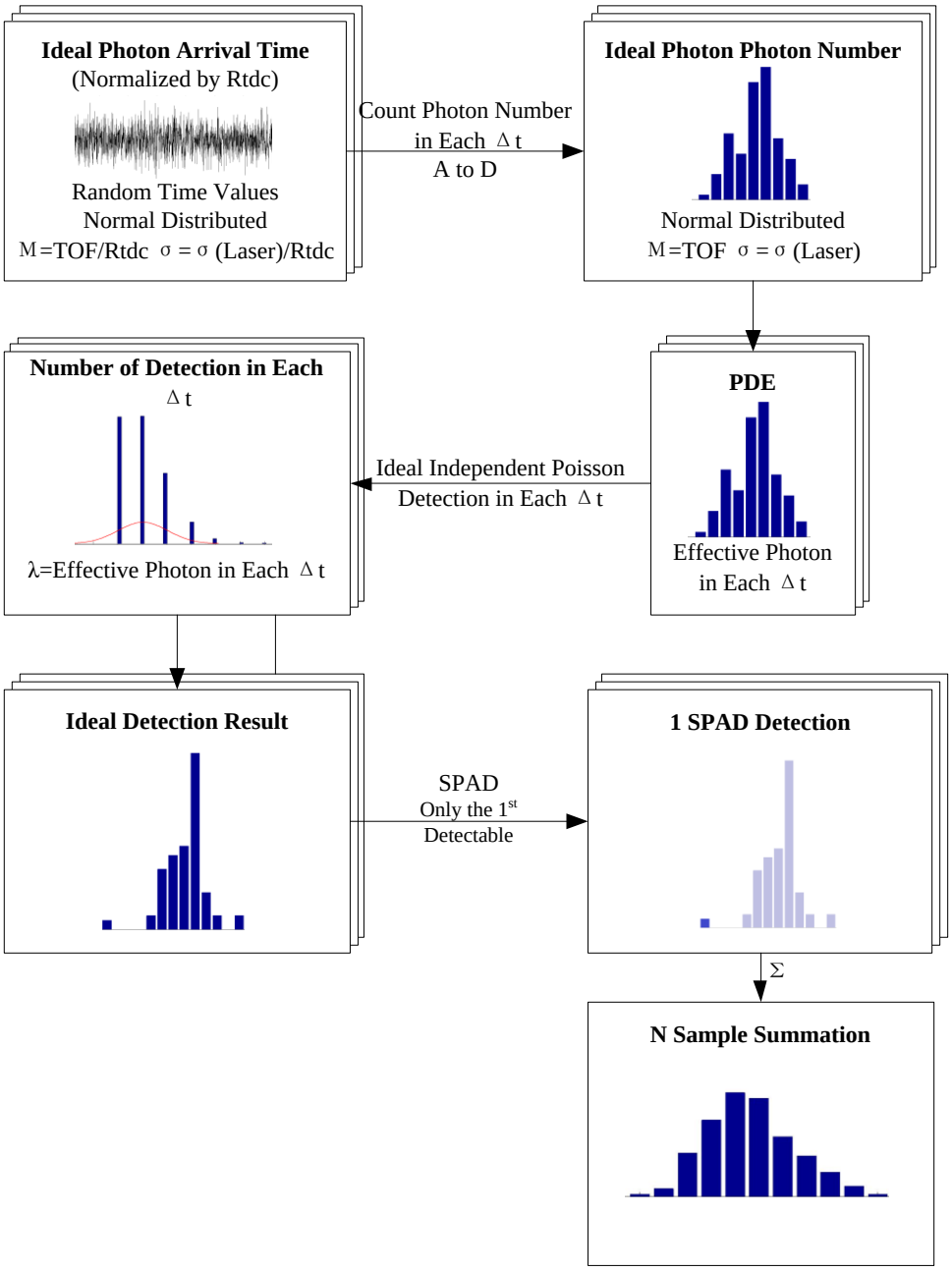

Figure 2.4: Block Diagram of Step 1 and 2

in Appendix A Figure A.1. Equation used for the theoretical simulation is based on Equation 2.12, as follows:

$$\widetilde{N}(t) = N(t) \cdot e^{-\frac{M}{2}[1+erf(\frac{t-TOF}{\sqrt{2}\sigma_\tau})]}, \tag{2.14}$$

with $\widetilde{N}(t)$ the final photon detection histogram and N(t) the number of signal photons as a function of time.

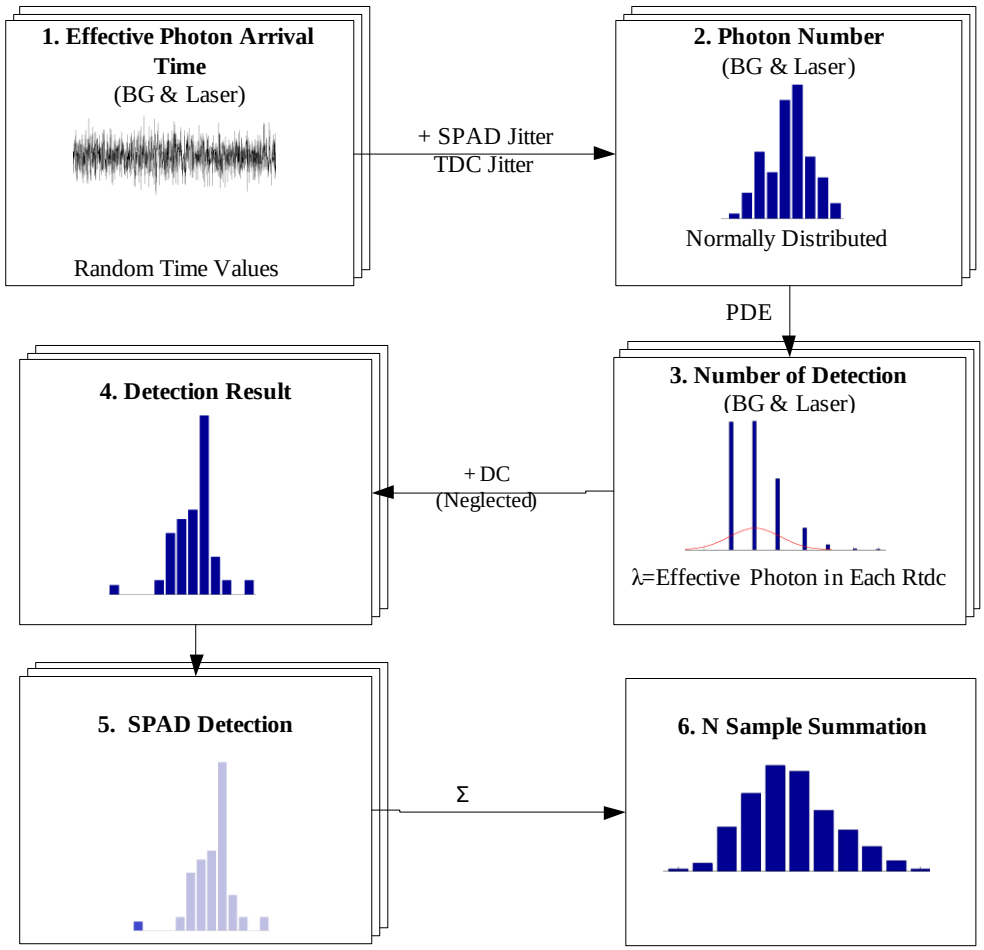

Figure 2.5: Block Diagram of Step 3

The simulation result of the first step is shown in Figure 2.6. TOF is set to 10 ns. By using different expected number of photon detected by the SPD, i.e. M, distortion caused by the TCSPC process is clearly shown in the result.

In the second step, background noise is introduced. It is assumed that the noise source is uniformly distributed solar light (100k lux). A perfect optical filter at 405 nm$\pm$ 5 nm is used. Irradiance at 405 nm sun light is 1.2 W/m^2/nm [10], taking into account atmosphere absorption, this value will be approximately 1.0 W/m^2/nm. For a 24 $\times$ 24 μm^2 pixel, optical power from background light will be 5.76 nW, in other words, about 1.17×10^{10} ambient photons arrive at the pixel every second. As discussed before, DC noise is neglected.

Part of flow chart of MATBAB program for random simulation that is different from the first step is shown in Appendix A Figure A.2. Theoretical simulation is based on the following equations:

$$Count = N \cdot N_{in} \cdot exp(-\lambda) \tag{2.15}$$

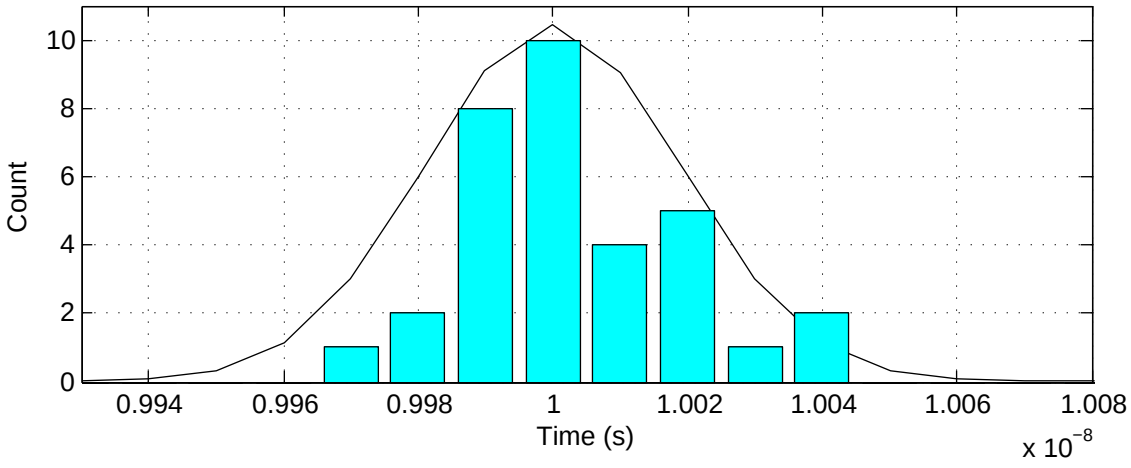

(a) M=0.01

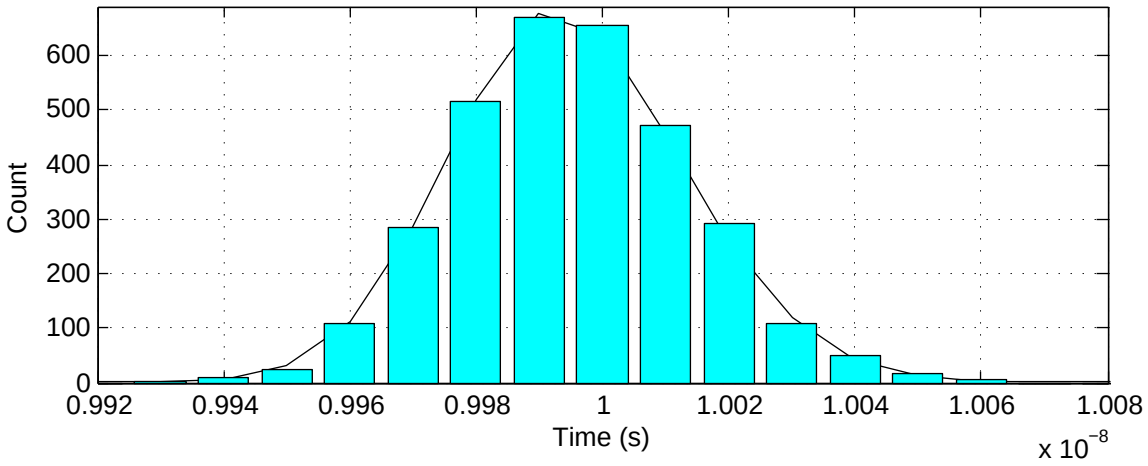

(b) M=1

Figure 2.6: Simulation Result of Step 1

$$N_{in}(t) = \frac{N_p}{\sqrt{2\pi}\sigma_\tau} e^{\frac{-(t-TOF)^2}{2\sigma_\tau^2}} + N_{BG} \tag{2.16}$$

$$\lambda(t) = \frac{N_p}{2}[1 + erf(\frac{t-TOF}{\sqrt{2}\sigma_\tau})] + N_{BG} \cdot t \tag{2.17}$$

N is the number of range detections. $N_{in}(t)$ is the number of input photons as a function of time. $\lambda(t)$ is the expectation of Poisson distributed TCSPC process at time t. N_p and N_{BG} are the effective number of signal and noise photon in one detection (detection frequency is f_0), respectively.

Simulation results with M=0.1 and M=0.01 are shown in Appendix B Figure B.1 and B.2.

SPAD and TDC used in this project are not ideal, they have jitter. In the third step of the simulation, it is assumed that both their jitter follow ideal normal distribution. Other assumptions are the same as those in the second step.

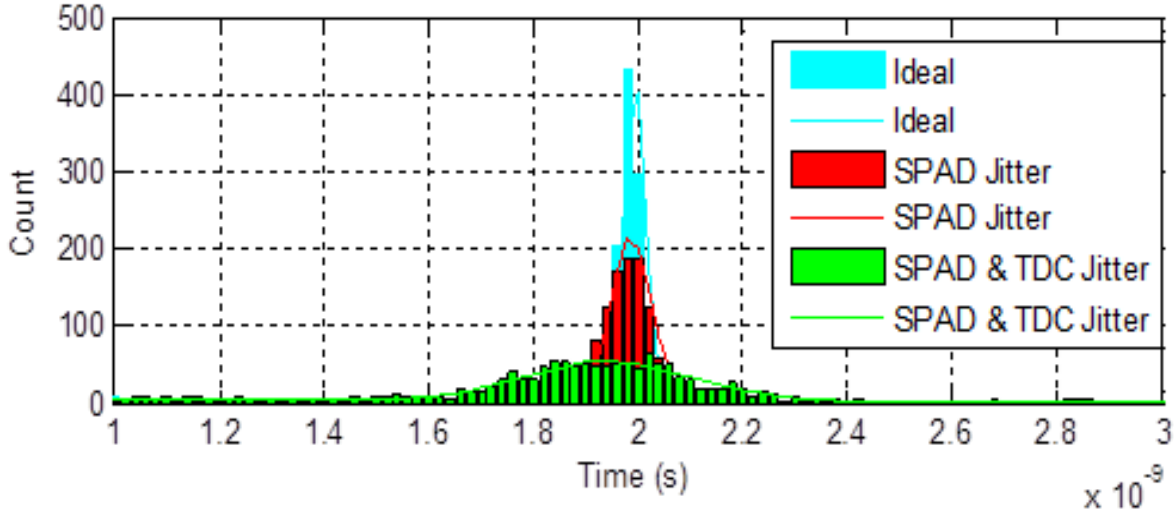

Figure 2.7: Simulation Result of Step 3

Part of flow chart of MATBAB program for random simulation that is different from the second step is shown in Appendix A Figure A.3. Theoretical simulation is based on Equation 2.15, 2.16, and 2.17. The difference is as follows:

$$\sigma = \sqrt{\sigma_\tau^2 + \sigma_{SPAD}^2 + \sigma_{TDC}^2}. \tag{2.18}$$

Simulation result with M=0.1 and M=0.01 are shown in Appendix B Figure B.3 and B.4. For a better view of the effect of jitter, a simulation with enlarged jitter variance is performed, and the result is presented in Figure 2.7.

2.2.3 Model Verification

To verify the TCSPC model built in Section 2.2.1, a 3D range detector set-up based on the range sensor reported in [17] is built in this project. Detailed introduction of the range sensor and the 3D range detector setup are presented in Chapter 3 and Chapter 4, respectively.

Basic steps of the model verification are as following:

1. TOF measurement is performed with the 3D range detector.
2. Build a histogram based on the measurement of the first pixel (for simplicity).
3. Calculate the FWHM and peak position (t_{peak}) of the histogram.
4. Perform simulation with real data.
5. Compare the histogram and results.

Verification results are shown in Appendix B Figure B.6. In Figure B.6a, only ambient light is involved in the measurement. The distortion shown in Figure 2.3b is verified. In the measurement, the SPAD output is used as the START signal of the

TDC, so the measurement result is horizontally reversed comparing with Figure 2.3b. A peak, namely the reset peak, is observed between 300 and 350 of the TDC output. The reason for this is that the SPAD is turned on to recharge before the range detection starts. In this period, the SPAD can be triggered. However, since the reset signal is high at the same time, quenching does not happen. So whenever the SPAD is triggered during this reset period, it gives a start signal to the TDC at the beginning of the range detection period. And it will not detect any photon again during that range detection period. As a result, a peak is observed and the measurement result from 0 to 300 is much lower than the simulation result.

In Figure B.6b, laser signal is added. A mismatch in the peak position of the model and the peak position of the measurement result occurs. The mean reason for this is that some delay in the system is not measurable. The estimation of TOF value used in the simulation is not accurate. FWHM of the signal peak in the measurement result is worse than the one in the simulation result, which is caused by non-ideality of the setup and optical signal. Count at the peak position of the measurement result varies from pixel to pixel. It is mainly caused by the non-uniformity of light intensity of the laser spot, which will be discussed in Section 2.3.1.

Generally speaking, the model built in this project matches the real measurement better than the model built in [10].

2.3 Model of the Signal

The signal source used in this project is a 405 nm laser diode system (Advanced Laser Diode Systems A.L.S. GmbH, Germany). The specifications of the laser system under the condition of internal trigger and normal tune value are shown in Table 2.1.

Specc.	Value
Wavelength λ(nm)	405 (FWHM=1.3)
Pulse Frequency f_0 (Hz)	40M
Pulse $FWHM_p$ (ps)	44.8
Pulse Energy E_p (pJ)	29
Focal Length (mm)	4
Jitter rms_{lj}(ps)	1.6
Beam Size (mm)	1.1×2.5 [1] ($1/e^2$)
Beam Divergence θ (mrad)	0.25×0.1 ($1/e^2$)
Emitter Size (μm)	0.8×1.8 [2] (roughly)
Delay t_L (ns)	38.9

Table 2.1: Laser Data [23]

The goal of modeling laser signal is to provide the TCSPC model built in Section 2.2 a reasonable value of signal photon amount. Output of this model is the number of photon that fall on a SPAD (24 μm × 24 μm) during illumination of one pulse from the laser.

[1] Ellipse, b×a
[2] Retangular

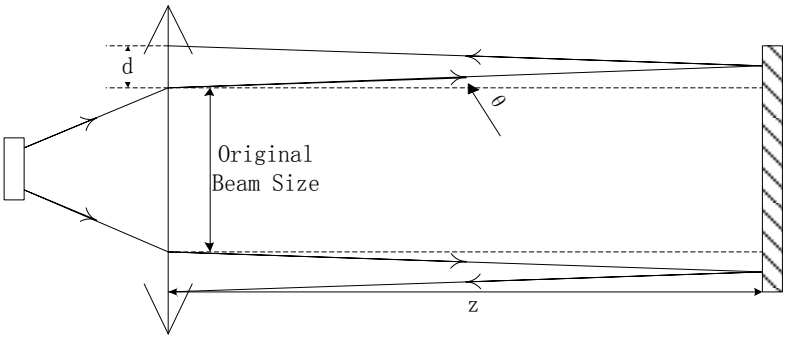

Figure 2.8: Non-ideal Collimation

2.3.1 Ideal Laser Transmission

For ideal laser transmission, following assumptions are made:

1. Ideal reflection, i.e. 0° injection angle, 100% reflectivity.
2. Ideal transmit, i.e. no optical power lose in transmit.
3. Optical power follows uniform distribution in space, normal distribution in time.
4. Beam shape is ideal ellipse.
5. No lens is used.

Under these assumptions, with an ideal mirror as the target, the only cause of laser signal attenuation in this project is non-ideal collimation. As shown in Figure 2.8 it is clear that at a distance of z,

$$FinalBeamSize = OriginalBeamSize \times Magnification, \tag{2.19}$$

$$Magnification \approx \frac{2z}{FocalLength}. \tag{2.20}$$

It is easy to see that the divergence of laser

$$d = 2 \times z \times tan(\theta), \tag{2.21}$$

with θ=0.1 mrad for semi-major axis and θ=0.25 mrad for semi-minor axis.

For original beam, semi-major axis d_{01}=2.5 mm, semi-minor axis d_{02}=1.1 mm, so

$$FinalBeamSize = \pi(d_1 + d_{01})(d_2 + d_{02}), \tag{2.22}$$

with d_1 the divergence of semi-major axis and d_2 the divergence of semi-minor axis.

Surface area of a pixel is known as $S_{Pitch} = Pitch^2 = 576 \times 10^{-6} mm^2$

When the target is 100 m away from the detector, number of photons fall on a detector is

$$N_0 = \frac{S_{pitch}}{FinalBeamSize} \cdot E_p \cdot \frac{wavelength}{hc} \approx 9.4. \tag{2.23}$$

Obviously, N_0 is the maximum number of photons input per pixel per pulse with this laser. In reality, the optical power will be attenuated by the atmosphere, the target, and the detector. Furthermore, optical power distribution in space is not uniform. Shape of the laser spot is shown in Appendix C Figure C.1. Center of the spot has the strongest light intensity.

2.3.2 Diffused Reflection

In reality, the target of the TCSPC system built in this project is not known as a priori. It is necessary to build a model that can estimate the optical output of the target based on basic information of its surface. In this section, a model based on [24] will be presented. For simplicity, only reflection is under consideration.

Existing models of reflection can be divided into two kinds, the physical model and the geometrical model. Physical model is based on Maxwell's equations and other electromagnetic wave theories. It is a general model that can be applied from perfectly smooth surface to very rough surface. However, for machine vision, geometrical model are more widely used. Geometrical model is a simplified physical model. It can only be applied when dimensions of the surface imperfections are much larger than wavelength of incident light.

In our system, the wavelength of incident light is 405 nm. The smoothest target can be glass or automotive paint, whose arithmetical mean roughness R_a can be as low as 40 nm (RMS $\approx 1.1 \times$ R_a)[25]. The roughest target can be brick wall or tree bark. As a result, both physical and geometrical model should be used.

Reflection on a surface is mainly determined by the microscopic shape characteristics of the surface. Mathematical models of surface are random models, which describe the surface either by a statistical distribution of their height or slope (surface roughness models). Study of surface roughness model is reported in Appendix D [24].

As shown in Figure 2.9, total surface reflection consists of three components. Diffuse lobe shown in the figure represents light reflected due to internal scattering mechanism. It is uniformly distributed in all directions. The specular lobe represents single reflection of incident light. It is distributed around the specular direction, but with a slightly diffused direction due to surface roughness. Specular spike describes light reflection caused by mirror-like smooth surface.

Without going into too much detail, we utilize the conclusion of [24] directly. The total image irradiance equation is

$$I_{ir} = C_{dl} + C_{sl} + C_{ss}\delta(0), \tag{2.24}$$

with C_{dl}, C_{sl}, C_{ss} the strengths of the diffuse lobe, specular lobe and specular spike components, respectively. Detail study of radiance of the reflected light is presented in Appendix E.

As discussed in Appendix E, the optical energy of specular spike and specular lobe decrease dramatically when surface roughness of the target surface increases. For simplicity, only the worst case is under consideration in this section, i.e. only the diffuse lobe exists. For long distance application, effect of non-ideal laser collimation can be

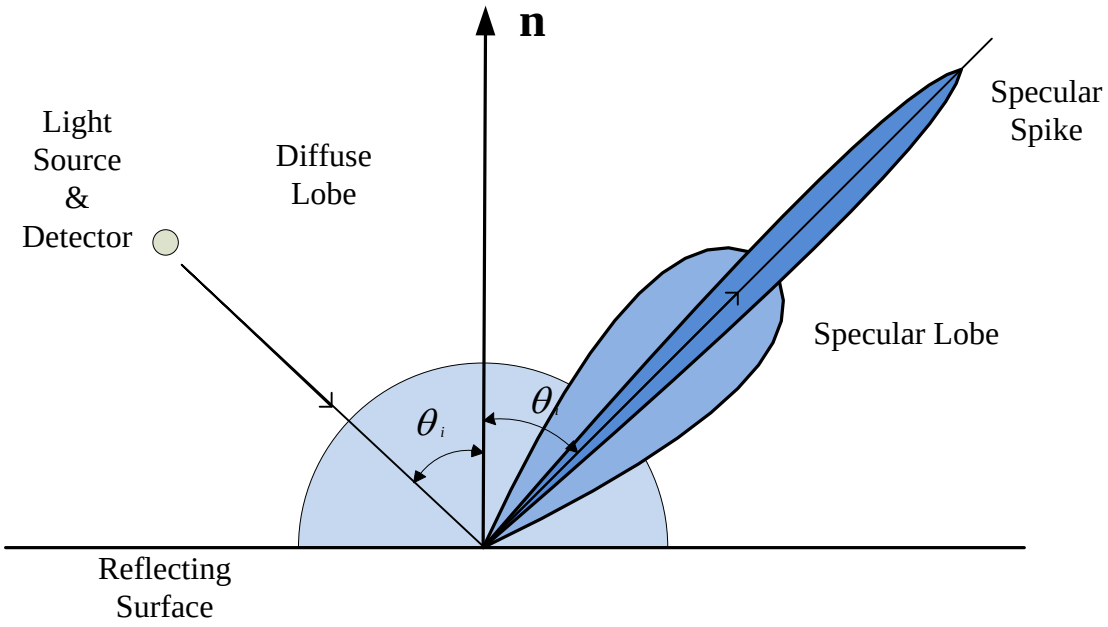

Figure 2.9: Reflection Components

ignored. Assume that reflectivity of the target surface is R_t. At a distance of z, total optical energy input of a pixel after one laser pulse is

$$E_{d0} = \frac{S_{pitch}}{2\pi z^2} Q_p R_t. \tag{2.25}$$

When z=100 m, $R_t = 50\%$, number of photon falls on one detector is

$$N_0 = \frac{E_{d0} \times Wavelength}{hc} \approx 1.25 \times 10^{-7} per\ pulse. \tag{2.26}$$

Another worst-case situation will occur when the target surface becomes too smooth. In this situation, only specular spike exists. If the injection angle $\theta_i \gg 0°$, no photon will arrive at the detector surface.

2.3.3 Atmosphere Attenuation

For long distance TCSPC application, attenuation caused by the atmosphere should be taken into account. Attenuation effect in atmosphere is caused by scattering and absorption. For light at 405 nm wavelength, the main cause is Rayleigh scattering. According to Beer–Lambert law, attenuation of light with wavelength λ is defined as

$$Absorbance_\lambda = ln(\frac{1}{T}) = -ln(\frac{I_{out}}{I_{in}}) = \sigma \cdot L \cdot N, \tag{2.27}$$

with I_{in} and I_{out} the input and output radiation intensity through a material, respectively; σ the absorption cross section; L the thickness of the material; and N the number density of absorbers.

It is easy to get the transmission as

$$Tr = e^{-\sigma \cdot L \cdot N}. \tag{2.28}$$

Number density of the atmosphere is known as

$$N = N_0 e^{-\frac{z}{H}}, \tag{2.29}$$

with N_0 the number density of atmosphere at sea level, z the altitude, $H = \frac{kT}{mg}$ the atmospheric scale height, and m the average molecule mass. From ideal gas law, it is known that $N_0 = 2.55 \times 10^{19}$ /cm^3, with pressure of 1 atm and temperature of 288.15 K [26]. Transmission in the atmosphere at a particular altitude of z and distance of L is

$$T = e^{-\sigma \cdot L \cdot N_0 e^{-\frac{zmg}{kT}}}. \tag{2.30}$$

For transmission at sea level, z=0, Equation 2.30 becomes

$$T_0 = e^{-\sigma \cdot L \cdot N} = e^{-\sigma \cdot L \cdot N_0}. \tag{2.31}$$

According to ideal gas law,

$$PV = nRT = NkT. \tag{2.32}$$

Variables are pressure P in Pa, volume V in m^3, temperature T in K, total amount of gases in number of mole n, and number of gases molecules N. Constants are universal gas constant $R = 8.3145$ J/(mol $\cdot$ K) and Boltzmann constant $k = 1.38 \times 10^{-23}$ m$^2 \cdot$ kg $\cdot$ s$^{-2} \cdot$ K^{-1}.

From Equation 2.32, it is easy to see

$$N_0 = \frac{N}{V} = \frac{P}{kT}. \tag{2.33}$$

As a result, attenuation caused by Rayleigh scattering at sea level is a function of temperature, air pressure, and distance, as follows,

$$T_0 = e^{-\frac{\sigma L \cdot P}{kT}}. \tag{2.34}$$

At a higher altitude, for instance z=2000 m, Equation 2.31 is not valid. Transmission becomes

$$T_z = e^{-\sigma \cdot L \cdot N_0 e^{-\frac{zmgM_a}{kT}}}, \tag{2.35}$$

with $m_a = 1.66 \times 10^{-27} kg$ the atomic mass.

The only factor remains unknown in Equation 2.35 is the average molecule mass, m. It is determined by the ratio of gas components, the temperature, and the air pressure. A general expression of m is derived in Appendix F. For simplicity, it is assumed that the atmosphere contains only Nitrogen, Oxygen, and water vapor. We also work on the assumption that the ratio between Nitrogen and Oxygen is identical to the ratio in ideal

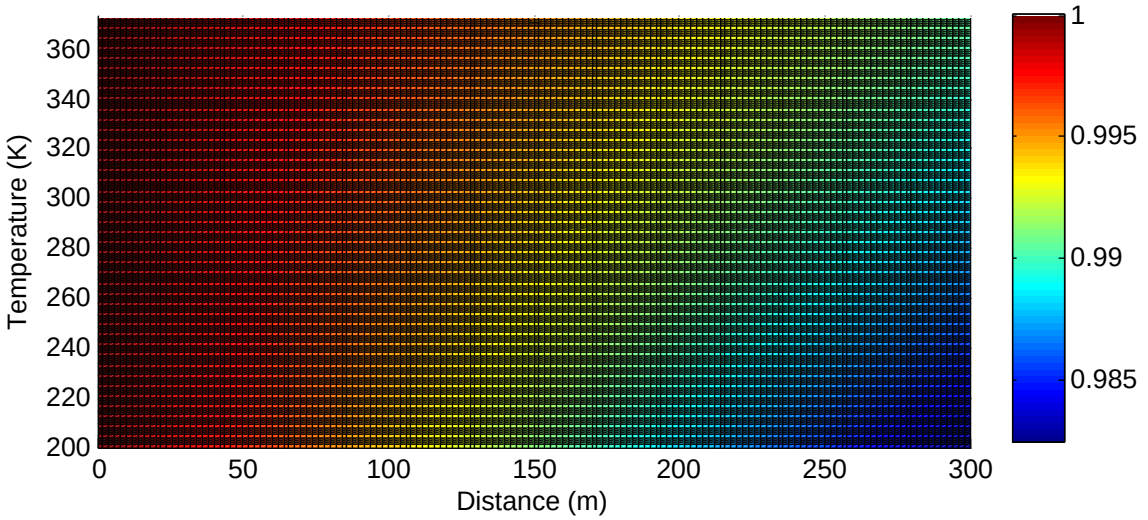

Figure 2.10: Transmission Factor at Sea Level

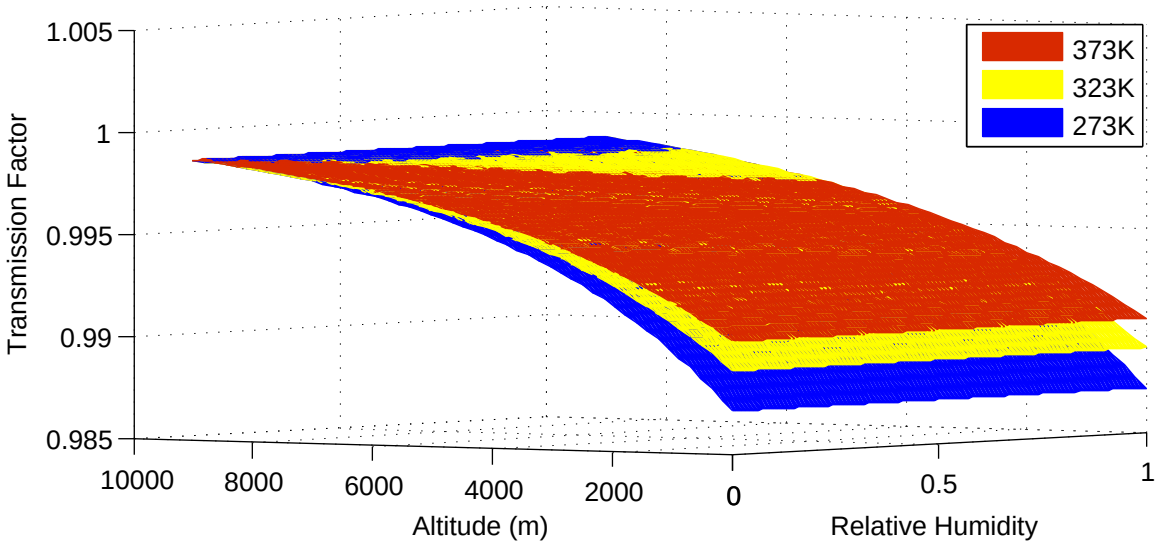

Figure 2.11: Transmission Factor for 300m Distance

dry air. The concentration of water vapor is determined by humidity. By substituting Equation F.12 into Equation 2.35, we have

$$T = e^{-\sigma \cdot L \cdot N_0 \cdot e^{-\frac{zgm_a}{kT}(29.6-\frac{11.6 \cdot RH \cdot \varepsilon_{w^*}}{P_{atmosphere}})}}. \tag{2.36}$$

Simulation results of Equation 2.31 and 2.36 are shown in Figure 2.10 and Figure 2.12.

In Figure 2.11, it is shown that the worst-case transmission attenuation always happens at sea level. Humidity affects transmission attenuation at higher altitude, the higher humidity, the higher attenuation. When temperature rises, water vapor in the atmosphere dominates. In Figure 11, it is shown that attenuation at sea level increases when temperature drops. At 273 K, transmission factor at 200 m is 99.14%. As a

result, for our project, it will be safe that we assume an atmosphere attenuation factor of 3%.

2.4 Model of the Noise

Noise sources of the TCSPC system built in this project can be the ambient light, the DC, the afterpulsing, the crosstalk, etc. However, as discussed in Section 2.2.1, DC of the SPAD can be neglected. Furthermore, afterpulsing is also negligible. Because the system works in photon starving mode and the active time of the SPAD (80 ns) is much shorter than the inactive time (¿102 μs). As a result, the ambient light is the dominant noise source.

For the targeted application, ambient light source can be either natural or artificial. After studying different light sources in this section, we will build a model that can provide the TCSPC model in Section 2.1 a reasonable value of $\overline{b}$, i.e. contribution of noise to the final histogram defined in Equation 2-9.

2.4.1 Natural Light

The natural light source under concern in this project is solar light, or the sunlight. Spectral contents of sunlight at the top of the atmosphere can be modeled with Planck's law of blackbody radiation, with emitting temperature T = 6000 K [27]. Normalized blackbody radiation expression is

$$\hat{I}(\lambda) = \frac{1}{\lambda^5(e^{\frac{hc}{\lambda kT}}-1)}[\int_0^\infty \frac{1}{\lambda^5(e^{\frac{hc}{\lambda kT}}-1)}]^{-1}. \tag{2.37}$$

For sunlight irradiance at the top of the atmosphere, we have:

$$I_s(\lambda) = \hat{I}(\lambda) I_{top}, \tag{2.38}$$

with I_{top} the sunlight irradiance at the top of the atmosphere.

According to observation data from Active Cavity Radiometer Irradiance Monitor (ACRIM), since 1980, total irradiance I_{top} of the sun varies between 1360 W/m^2 and 1363 W/m^2 [28].

I_s as a function of wavelength is plotted in Figure 2.12. In this project, the wavelength of interest is 405 nm, i.e. wavelength of the laser. Value of I_s at 405 nm at top of atmosphere is I_{s0} (405 nm) = 1711.4 W/m^2/μm.

At sea level, irradiance of sunlight is weakened, known as

$$I_{s,sea}(405nm) = I_{s0}(405nm) \cdot T. \tag{2.39}$$

T is the atmospheric transmission as a function of altitude, which describes atmosphere absorbance of sunlight at a particular wavelength. According to the calculation in Appendix G, it is known that T of 405 nm sum light at sea level is 74.20%. So it is easy to get

$$I_{s,sea\ level,subsolar\ point}(405\ nm) = I_{s0}(405\ nm) \cdot T \approx 1269.9\ W/m^2/\mu m. \tag{2.40}$$

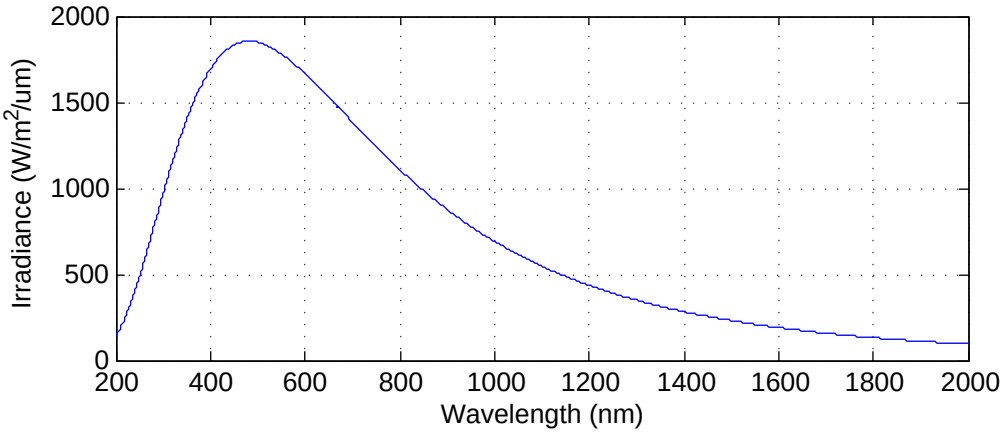

Figure 2.12: Solar Spectrum at Top of Atmosphere

Compared with the solar spectrum shown in Appendix C Figure C.2, this result of transmission factor is higher. Several reasons cause the mismatch. The first reason is that the N_0 in Equation G.2 is smaller than reality. In Equation 2.20, $N_0$is calculated based on ideal dry air, which is smaller than actual case with vapors. Moreover, the temperature used in Equation 2.20 is higher than atmosphere temperature used in Equation G.2, which also results in a smaller value of N_0. The second reason is that we only consider Rayleigh scattering in the model, while in real case, more absorptions occur. The third reason is that the atmosphere thickness we choose may be less than real case. In reality, the thickness of atmosphere varies. The maximum thickness can be about 120 km. The last reason is that we neglect exosphere and thermosphere, which strongly reduces XUV and higher frequency sunlight. They also absorb visible light. However, for worst case background light situation, our result will still be suitable for the model. In conclusion, number of photons arrive on one pixel is approximately 15×10^9 /s, with a 400 nm ~ 410 nm ideal optical filter in clear mid-day direct sunlight at sub solar point.

2.4.2 Artificial Light

Artificial light sources nowadays, such as metal-halide (MH) lamps, high-pressure sodium (HPS) lamps, high-intensity discharge (HID) lamps, and light-emitting diode (LED), can produce high intensity light. Some of them are specially made to produce blue light, which contents the wavelength of interest of this project. Furthermore, in the targeted application, artificial light sources can easily have direct injection on our SPD, even with carefully shielding.

Wavelength of interest in this project is close to ultraviolet. To guarantee safety, radiation of ultraviolet is strictly limited for artificial light sources utilized on street. For example, in Europe, it is indicated that the radiation in ultraviolet bandwidth can only be 6% of total radiation of the range 250 -780 nm, in other words, 0.004 %/nm in average [29]. With continuous spectrum, it is reasonable to assume that in range 400 - 410 nm, radiation is 0.8 % of the total's.

The spectrum of MH lamps and HPS lamps are shown in Appendix C Figure C.3.

MH lamps are widely used in vegetation, with strong radiation in UVA bandwidth. However, products for lighting also exist. HPS lamps and LED lamps are always used in street lighting. However, as shown in Figure C.3b and Figure C.4, radiation in our wavelength of interest from these lamps is negligible. HID lamps are being utilized in automotive industry as vehicle headlamps, though they are more discomforting than other light sources. As shown in Figure C.5, HID lamps have higher radiation in UVA bandwidth and our bandwidth of interest. Moreover, utilized as headlamps, there will be more chances of direct injection.

All artificial light sources under our consideration share one common characterization. They are all divergent. For lighting light sources, they often have a divergent angle larger than θ_{l}= 90°, and for vehicle headlights, their divergent angle is about θ_{h}= 45°. As a result, in a distance s, their illuminance is

$$I = \frac{Luminous\ Flux}{\Omega s^2}, \tag{2.41}$$

with Ω= $2\pi(1 - \cos\theta)$ the solid angle of light source.

Consider a MH light produced by LunarLighting, with 1.5Mlm output, at a distance of 10 m, illuminance becomes

$$I_{MH} = \frac{Luminous\ Flux_{MH}}{\Omega_{MH} s^2} = \frac{1.5 \times 10^6}{2\pi[1 - cos(90°)] \cdot 10^2} \approx 2.389\ k \cdot lx. \tag{2.42}$$

Consider a HID lamp produced by Xenon, with 3200 lm output, at a distance of 5 m, illuminance becomes

$$I_{HID} = \frac{Luminous\ Flux_{HID}}{\Omega_{HID} s^2} = \frac{3200}{2\pi[1 - cos(45°)] \cdot 5^2} \approx 69.6\ lx. \tag{2.43}$$

In conclusion, compared with solar illuminance studied in previous section (100 k·lx), it is clear that ambient light caused by artificial light sources is much weaker.

2.5 Performance Prediction Model

As discussed at the beginning of this chapter, the main goal of developing the mathematical model is to qualitatively predict the performance of a TCSPC system. The prediction can help designers set up targeted specifications of each part of a TCSPC system at the starting point of their design. Optimization of performance and reduction of cost can be expected.

2.5.1 Basic Principle

Range detection result of a TCSPC system is a statistical result based on large number of measurements with random outcomes. According to principles of TCSPC, TOF measurement is reliable only when the signal peak can be discriminated from the noise [10]. As a result, worst-case photon count at the peak position should be larger than the maximum photon count caused by noise at the same position, i.e.

$$h(TOF') - \alpha_h \sigma_h > b(TOF') + \alpha_b \sigma_b, \tag{2.44}$$

with α_h the confidence interval coefficient of the histogram, α_b the confidence interval coefficient of the noise, σ_h the standard deviation of the histogram, and σ_b the standard deviation of the noise.

The number of detected photons follows Poisson distribution. In the histogram, after large amount of samples, the expectation value of the Poisson distribution becomes so large that we can approximate it with normal distribution with the same mean value and standard deviation. Define P as the probability of successfully distinguishing the signal peak from the histogram, [10] has proven that

$$\alpha_h = \sqrt{2} \cdot erf^{-1}(P), \tag{2.45}$$

$$\alpha_b = \sqrt{2} \cdot erf^{-1}(1 - \frac{1-P}{\frac{T_0}{\Delta t} - 1}), \tag{2.46}$$

$$\sigma_h = \sqrt{h(TOF')}, \ and \tag{2.47}$$

$$\sigma_b = \sqrt{\bar{b}}, \tag{2.48}$$

with T_0 the window size, $\triangle t$ the TDC resolution, and $\bar{b}$ the average count of noise.

In Inequality 2.44, information of the signal, noise, and setup are all included. h(TOF') is the total number of photon count at the peak position. It is determined by the number of signal photon counts. As shown in Equation 2.2 and 2.3, the signal photon counts are determined by the laser and the SPAD. Taking into account a more realistic situation, i.e. diffuse reflection at the target, it is also a function of the reflectivity and distance of the target.

The $\bar{b}$ contains all information of the noise caused by ambient light, which is known as the dominant noise source. T_0 is defined in the DAQ setup. $\triangle t$ is the most important character of the TDC.

As a result, with Inequality (2.44), most of the specifications of the TCSPC system can be linked to P. Prediction of the performance can then be used to figure out the optimized trade-off of all the specifications.

2.5.2 Simulation Results

Based on Inequality (2.44), simulations that predict the P of TCSPC systems with different specifications are performed. Basic steps of the simulation are as follow:

1. Input specifications of the system;
2. Generate histograms of a set of target distance based on Equation 2.12;[1]
3. Extract photon count information from the histograms;
4. Find out the maximum P in each histogram using Inequality 2.44;
5. Plot the maximum P as a function of distance.

Eight simulations are performed in total. Specifications used in each simulation are presented in Table 2.2. Simulation results are plotted in Figure 2.13.

	1	2	3	4	5	6	7	8
Pulse Energy (nJ)	100						400	0.029
Ambient Light (Lux)	100					400	100	100
Number of Samples	10000				40000	10000		40000
TDC Resolution (ps)	200			50	200			200
PDE (%)	2		8	2				1.3
Total Jitter Standard Deviation (ps)	200	800	200					666

Table 2.2: Specifications Used in Performance Prediction Simulation

As shown in Table 2.2 and Figure 2.13, performance of a TCSPC system, represented by the value of P, drops when the total jitter (as defined in Equation 2.18), the TDC resolution, or the ambient light intensity increases. On the contrary, the performance is improved when the number of sample, the power of the signal source, or the PDE increases.

In the second, third and sixth simulation, a sharp decrease of P occurs and P stays at zero afterwards. Reasons for this sharp decrease are the algorithm of peak detection and the TCSPC distortion. In this model, peak detection algorithm looks for the peak in the whole histogram. When distance increases to a particular value, as shown in Figure 2.14, the signal peak is no longer the highest point of the histogram. As a result, though the signal peak is still distinguishable in the histogram, the system gives a wrong result. One possible solution to this effect is known as gating. The effect of gating will be discussed in Section 2.7.

Simulation 8 in Figure 2.13 is based on the specifications of the TCSPC system setup of this project. Detailed characterization of the system is presented in Chapter 3 and Chapter 4.

2.5.3 Measurement Verification

To verify the performance prediction model, a set of measurements was performed. Since only one setup of TCSPC system is available, the verification in this section can only confirm that the result of the eighth simulation in Section 2.5.2 is reasonable.

Definition of P in the simulation is the probability of successfully detecting the signal peak. In measurement, however, histograms of range detection are random, especially when the amount of signal photon is limited. Success in detecting a peak is not equivalent to success in range detection. Therefore, P should be redefined as the probability of generating a range detection result within a preset error tolerance range. Results of the simulations in Section 2.5.2 are the optimum of it.

Basic steps of measurement variation are as follow:

1. Range detection with mirror as the target, use the results as ideal results;

[1]In this step, it is assumed that reflectivity of the target is 1 and reflection on the surface of the target is ideal diffuse reflection. Number of reflected signal photons fall on one pixel (24 μm $\times$ 24 μm) with the target at a distance of x is N =$N_0 \times \frac{576\times10^{-12}}{2\pi x^2}$.

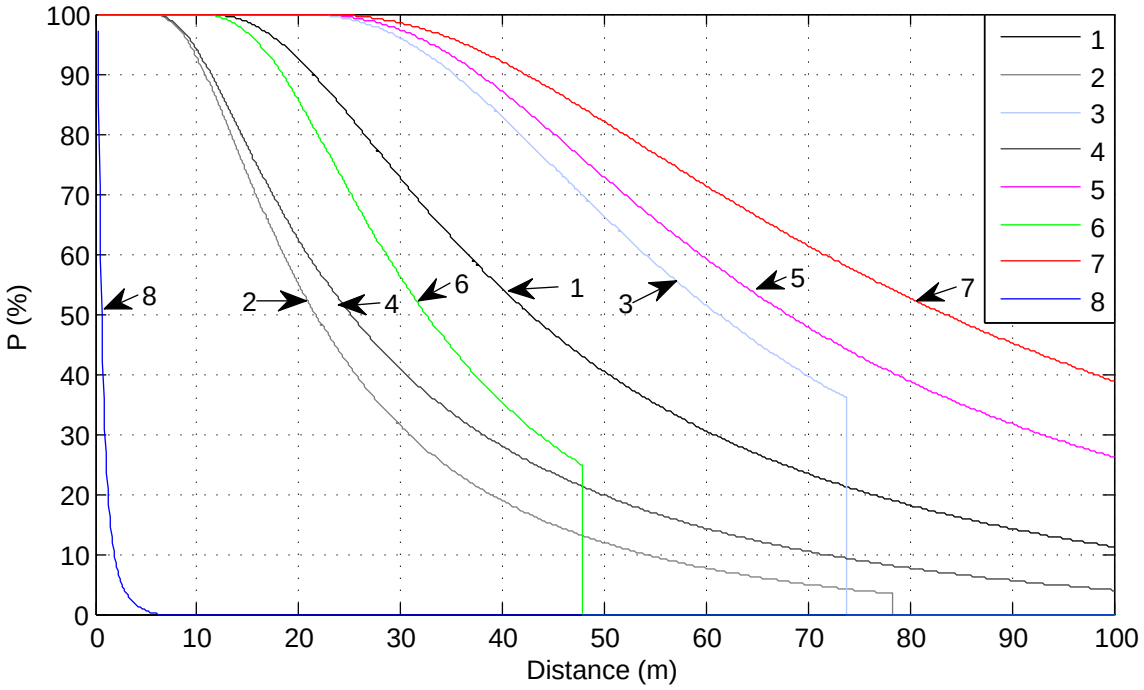

Figure 2.13: Peak Detection Probability Prediction

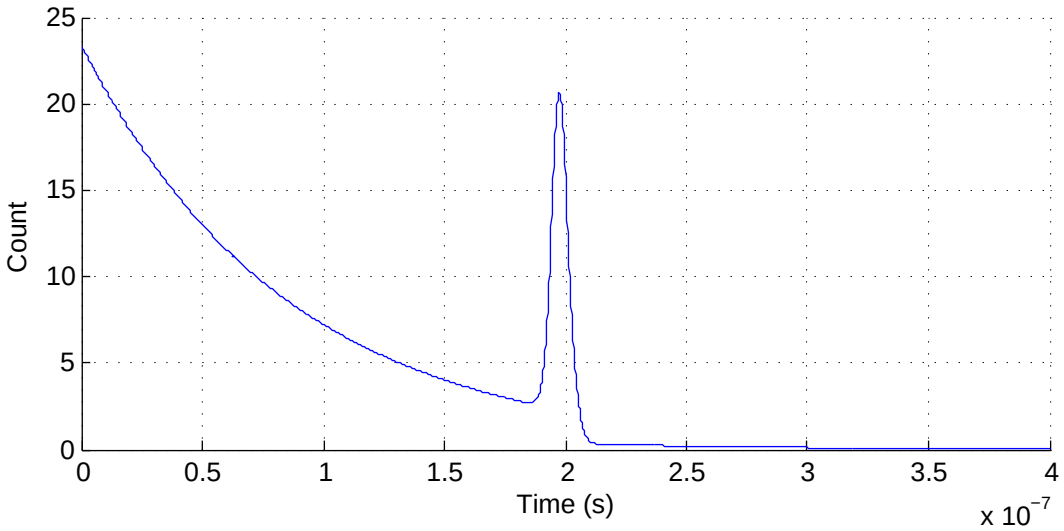

Figure 2.14: Histogram at Long Distance

2. Range detection with white paper as the target;

3. Calculate the range detection error of the second step;

4. Calculate the percentage of measurements that have an error within ±2 LSB;

Output of the fourth step will be used as the P of measurement. Five range detec-

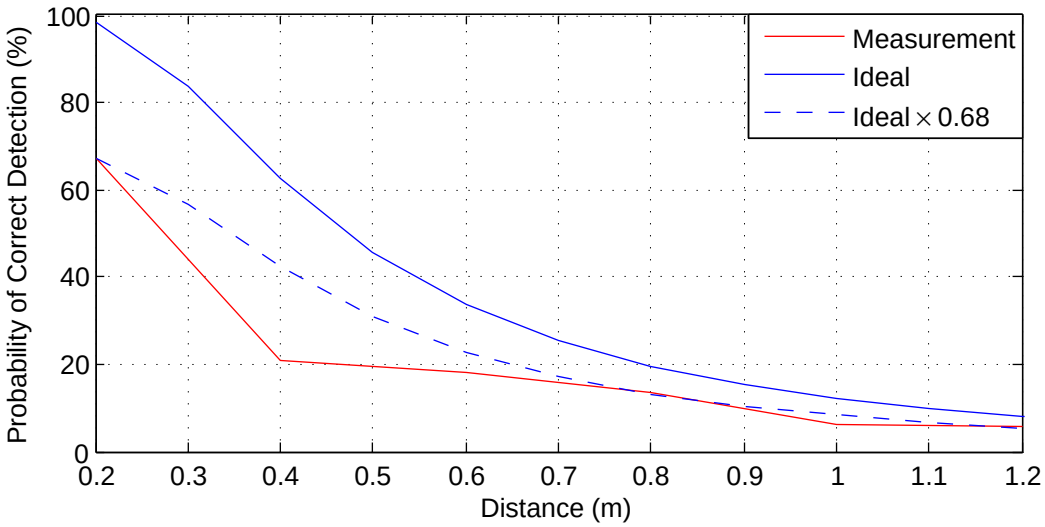

Figure 2.15: Measurement Verification of Performance Prediction

tions were performed at each distance. Results are shown in Figure 2.15.

According to the result shown in Figure 2.15, curve of the prediction shares the same trend with measurement result. The performance of the system in real measurement is worse than the prediction. This mismatch is reasonable. The main causes can be the difference of the definition of P, the error in system characterization, and error of the specifications, such as ambient light intensity, used in the model. By multiplying a non-ideality factor of 0.68, the results of measurements match well with the prediction.

2.6 Model Application: Moving Target

To further verify the model, in this section, an application of the model is presented. For automotive applications, the detector always has a state of motion relative to the target. For realistic application, it is necessary to study the performance of the system in such a state.

For the laser utilized in this project, FWHM of the pulse is 44.8 ps. When one pulse hit the target, in 44.8 ps, the target will move 2.24 nm, which generates a TOF difference of 7.45 attosecond, which is far less than the TDC resolution. So it will be reasonable to assume that reflection happens instantly.

Assume that the sampling rate of a TCSPC is 1 MHz, which is much better than the state-of-the-art TCSPC system.[22] Assume that 2000 samples are required for one range detection. When the target is moving towards the detector at a relative speed of v, distance difference of TOF measurement results of the first and the last sample will be 2 ms $\times$ v. Based on the model built in Section 2.1, the histograms at relative velocity of 0 m/s, 50 m/s, and 100 m/s are shown in Figure 2.16.

As shown in Figure 2.16, when relative velocity increases, variance of the histogram increases. With $v > 0$, the TOF measured in each sample increases. To reduce the

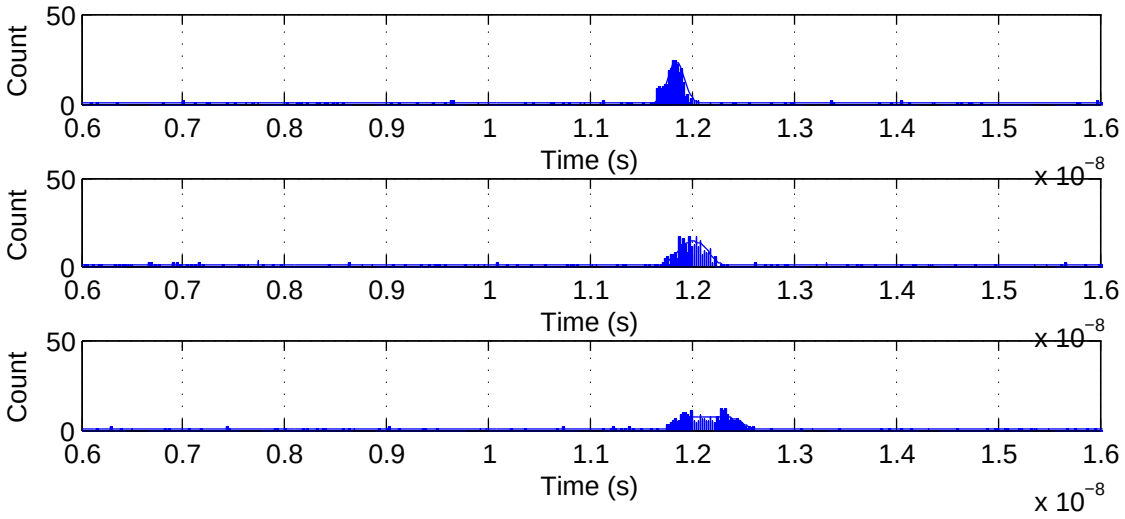

Figure 2.16: Moving Target Detection Histogram with Relative Speed of 0, 50 m/s, and 100 m/s

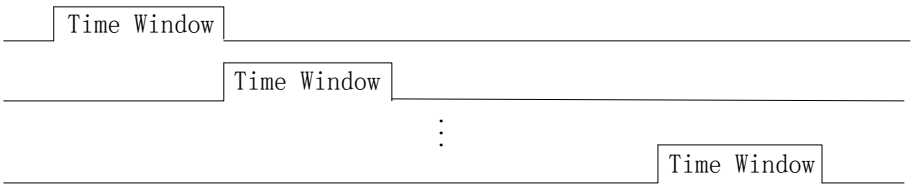

Figure 2.17: Gating Principle

effect of relative velocity, the most significant approach is to lower the range detection time, which can be achieved by decreasing the time of each sample, or by cutting the number of samples.

2.7 Model Application: Effect of Gating

In this project, gating technology is used in long-distance range detection. The principle of gating is shown in Figure 2.17. The time window is the time during which the SPADs and TDCs function and TOF measurement is performed. For gating technology, a short time window is used and shifted to extend the maximum detection range. As a result, only a specific range of distance, determined by the window size, is detectable in each measurement. The positive effect is that noise photons that arrive outside the window do not have any effect on the TOF detection, which is a significant improvement for long-distance range detection.

The effect of gating is shown in Figure 2.18. In Figure 2.18a, three histograms are presented, with TOF value of 60 ns, 120 ns, and 180 ns. When TOF value is 120 ns, it is shown that signal count at the TOF peak is already lower than the maximum count caused by noise signal when time is zero. When TOF value is 180 ns, the result is even worse. In 2.18b, gating technique is used. The window size is chosen as 50 ns.

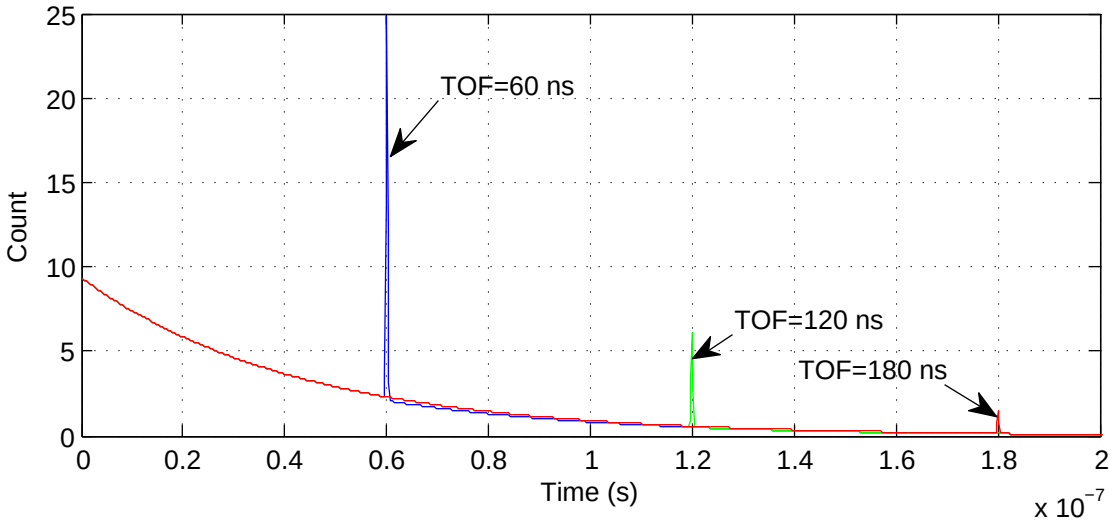

(a) Without Gating

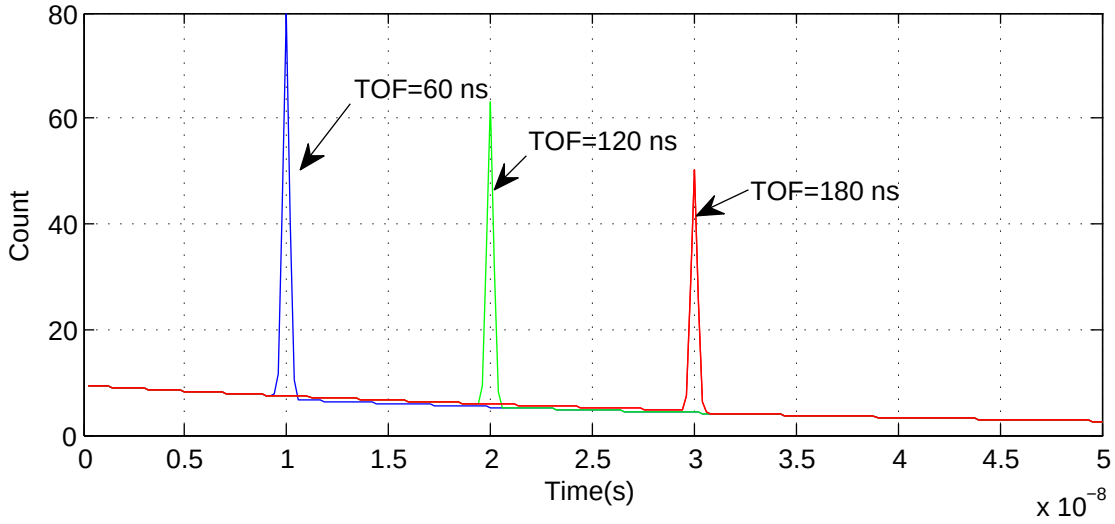

(b) With Gating

Figure 2.18: Effect of Gating

Compared with Figure 2.18a, signal count at the TOF peak is much higher. Signal count attenuation due to increase of TOF is much less than the previous case.

2.8 Summary

A complete model of TCSPC range detector is presented in this chapter. The model of the TCSPC process is built on top of the previous work reported in [10]. Improvement of introducing the distortion caused by the detection mechanism leads to better performance than the original work, which has been confirmed by random simulations and actual measurements. The attempt of modeling the behavior of optical signal of the

TCSPC system generates a reasonable estimation of input optical signal intensity. The study and model of the noise sources of the TCSPC system has proven that the sunlight causes the worst-case ambient noise, while artificial light sources can be neglected.

From all the models summarized before, it can be concluded that performance values of the TCSPC system cannot be optimized all at the same time. A trade-off of accuracy, speed, robustness, cost, and maximum range should be made. To help future designers make a better trade-off, a performance prediction model is built. Verification base on measurements has shown that output of this model is reasonable.

Finally the models are applied to analyze the performance of the TCSPC system under specific conditions. The application of analyzing moving target shows what the relative speed between the detector and the target has jitter-like effect on range detection. The application of analyzing the effect of gating shows that gating technology improves performance in long-range detection significantly.

3 The Sensor

The sensor utilized in this project for range detection was reported in [17]. It was fabricated in 0.35-μm CMOS technology. It has a 128-channel column-parallel two-stage TDC, with each channel of TDC connected to a pixel based on the SPAD reported in [22].

In this Chapter, a study of the TDC, SPAD, and operation are presented in Section 3.1, 3.2, and 3.3, with characterization results based on literatures and measurements. In Section 3.4, an artifact discovered during the measurement is reported, analyzed, and successfully removed.

3.1 The Pixel

Structure of the pixel is shown in Figure 3.1 [22]. The pixel employs a SPAD designed in [22], with both passive and active recharge circuitries controlled by VB and RST signal, relatively. A buffer is used to pulse-shape the output from the SPAD to the TDC. An off transistor controlled by OFF signal is used to disable the SPAD.

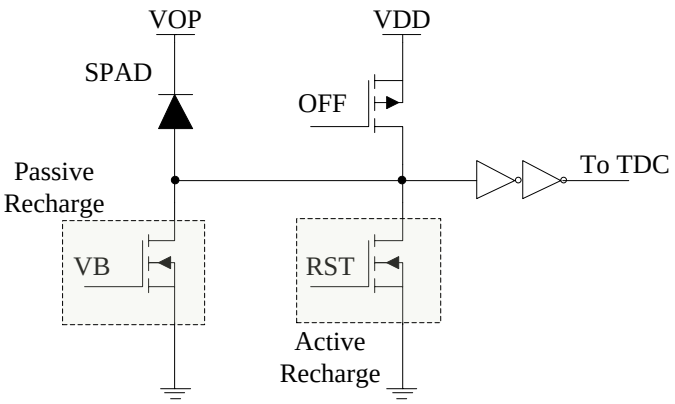

Figure 3.1: Pixel Structure [17]

From a system point of view, only breakdown voltage, photon detection probability (PDP), fill factor (FF), DCR, and jitter are relevant SPAD parameters in this project. A summary of these parameters is shown in Table 3.1.

Breakdown Voltage V_{BD}	19.4	Fill Factor FF (%)	4.9
DCR Level (Hz)[1]	100	PDP (%)	25

Table 3.1: SPAD Characters

The timing jitter of the SPAD is measured by illuminating the SPAD array with the laser discussed in Section 2.3. The measurement is performed under the condition that ambient light is negligible. With the laser trigger signal rises at the same time relative to the starting point of the time window, ideally, the SPAD output should rise at the same time relative to the laser trigger signal. By measuring the time difference between the rising edge of the SPAD output and the laser trigger signal, SPAD jitter can be acquired. In the sensor used in this project, only the output of the 128th SPAD is accessible. Therefore, the jitter measurement is based on this SPAD. Furthermore, by using the laser, jitter from the laser is also introduced to the measurement result. Therefore, the jitter measured here is actually the combination of laser jitter and SPAD jitter. After 12295 effective measurements, standard deviation of the SPAD output is 178.2 ps, which is also the standard deviation of the jitter. A plot of the measurement results is shown in Appendix H Figure H.2.

3.2 TDC

The TDC designed in [17] is a two-stage TDC based on voltage controlled oscillator (VCO) and time-to-digital amplifier (TDA). The resolution of the first-stage TDC is about 200 ps. The second-stage TDC has almost the same structure as the first-stage TDC. With the help of the TDA in between, overall TDC resolution becomes

$$LSB_{two\_stage} = \frac{LSB_{first\_stage}}{G}, \tag{3.1}$$

with G the gain of the TDA.

With a tunable gain, the TDC resolution can be set at any value between 8.9 ps and 21.4 ps.

In Section 2.5, it has been proven that a higher TDC resolution requires either higher optical SNR or longer detection time. For the targeted application, detection reliability, dynamic range, speed, and robustness against relative motion are more important than positional accuracy. As a result, in this project, we only use output of the first-stage TDC for distance calculation. In case of a timing resolution of 200 ps, the ideal special resolution of the system for range detection is 3 cm, which is acceptable for long-range detection in automotive applications.

The block diagram of the first-stage TDC is shown in Figure 3.2 [17]. It contains a dual-rail VCO, a VCO phase detector, a VCO cycle counter, and a synchronizer. In the TCSPC system of this project, the START signal is generated by the SPAD output. The STOP signal is generated by the FPGA. At the beginning of time conversion, START, STOP, SYNC and EN are low. After the START signal rises, EN becomes high, the VCO starts running freely. Meanwhile, the VCO phase detector and the VCO cycle counter start measuring the VCO output. When the STOP signal rises, the phase detector and cycle counter are frozen immediately. After two VCO cycles, the SYNC will rise, and the VCO will be disabled. According to [10], total conversion time is 320 ns, including the conversion time of the second stage TDC. After a conversion, for each

[1]DCR plot is shown in Appendix H Figure H.1. Effect of artifact is discussed in Section 3.4

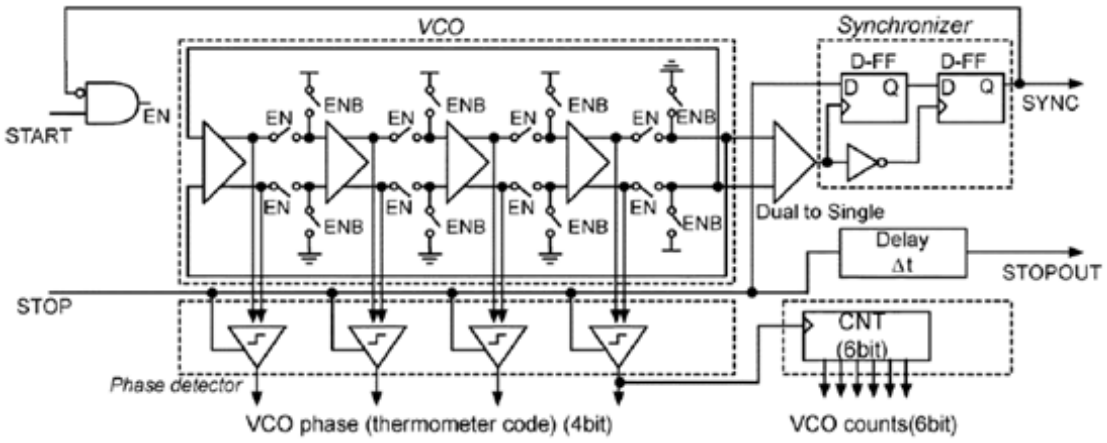

Figure 3.2: Block Diagram of the First-Stage TDC [17]

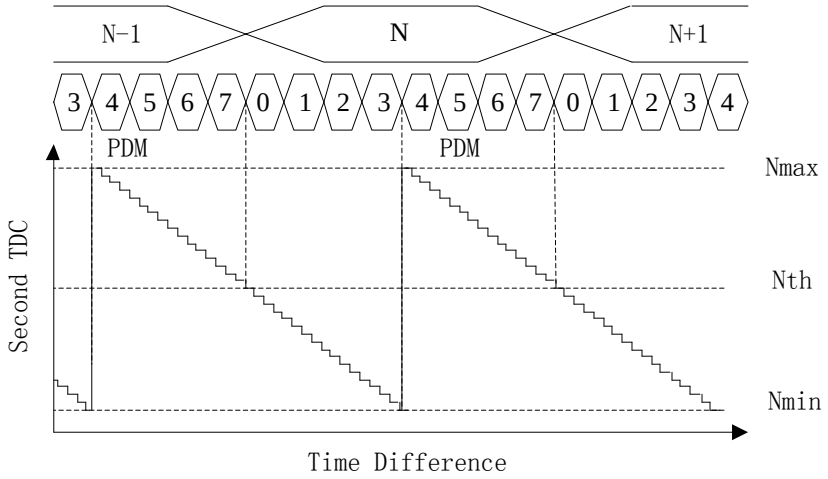

Figure 3.3: Second Stage TDC Output Calculation

TDC, the output data will be latched. The data contains a four-bit first-stage VCO phase detector output, a six-bit first-stage VCO counter output, a four-bit second-stage VCO phase detector output, a five-bit second-stage VCO counter output, and one extra bit. In total, each TDC output has twenty bits.

Output of the phase detector is encoded into thermometer code. Define the first-stage VCO phase detector output after decoding as P_{1st} and the first-stage VCO cycle counter output as C_{1st}, the raw digital code from the first-stage TDC D_{1st} is as follows:

$$D_{1st} = C_{1st} \times 8 + P_{1st}. \tag{3.2}$$

The relation between the first-stage TDC and second-stage TDC outputs is shown in Figure 3.3 [17]. To compute the second-stage TDC code, N_{min}, N_{th}, N_{max}, and PDM should be determined from TDC density test. Basically, N_{min} and N_{max} are the minimum and maximum output of the second-stage raw digital code, known as

$$D_{2nd} = C_{2nd} \times 8 + P_{2nd}, \tag{3.3}$$

with C_{2nd} the second-stage VCO counter output and P_{2nd} the second-stage VCO phase detector output. N_{th} is the minimum second-stage TDC raw digital code when $P_{1st} = 0$. PDM is the minimum second-stage TDC raw digital code when $P_{1st} = 4$. Theoretically, all D_{2nd} results should be within the range from N_{min} to N_{max}. Modified second-stage TDC output is

$$D_{2nd,mod} = \begin{cases} N_{max} - D_{2nd} + (N_{th} - N_{min} + 1), \ P_{1st} > PDM - 1 \ and \ D_{2nd} > N_{th} \\ N_{th} - D_{2nd}, \ else \end{cases} \tag{3.4}$$

The total TDC code is calculated as

$$D_{total} = C_{1st} \times (N_{max} - N_{min}) + D_{2nd,\ mod}. \tag{3.5}$$

The TDC characterization is performed using TDC density test. The SPAD array is used to generate random START signal. Measurement results of differential nonlinearity (DNL) and integral nonlinearity (INL) of a randomly chosen TDC are shown in Appendix H Figure H.3. Worst case DNL and INL result of all TDCs are shown in Appendix H Figure H.4 and Figure H.5.

The TDC resolution is estimated with density test as well, the result of the estimation is shown in Appendix H Figure H.6. However, the TDC resolution varies with total amount of injection photons. The variation can be calibrated. More discussion will be presented in Chapter 5.

The TDC jitter is measured in a similar way as the SPAD jitter. A START-STOP signal pair with fixed time difference is generated by the FPGA and used as the input of the TDCs. A histogram of TDC output is generated after large amounts of measurements. The FWHM of the histogram measured in this project is 1.2 LSB, which is then used as the FWHM of the TDC jitter.

The dynamic range of the TDC is determined by the TDC resolution and the counter size. For this TDC, the VCO counter has six bits. The VCO phase detector generates four bit thermometer code. As a result, output of the TDC has nine bits. The dynamic range of the TDC is $DR_{1st} = LSB_{1st} \times 2^9$, with LSB_{1st} the TDC resolution of the first-stage TDC.

3.3 The Operation

The sensor is mounted on a printed circuit board (PCB) designed by Dr. Shingo Mandai and controlled by an FPGA. Output of the sensor is collected by the same FPGA and sent to the host personal computer (PC) through Ethernet connection. Within the sensor, an integrated digital controller is implemented to control the TDC and the SPAD. Pin location of the sensor is shown in Figure 3.4 [30]. Some important signals for this project are as fillow:

Vdd! and Vdda are 3.3 V voltage supplies;

Vop: operation voltage for the SPAD;

clk: 3.3V, 25 MHz clock signal generated by the FPGA;

rst: reset the digital controller

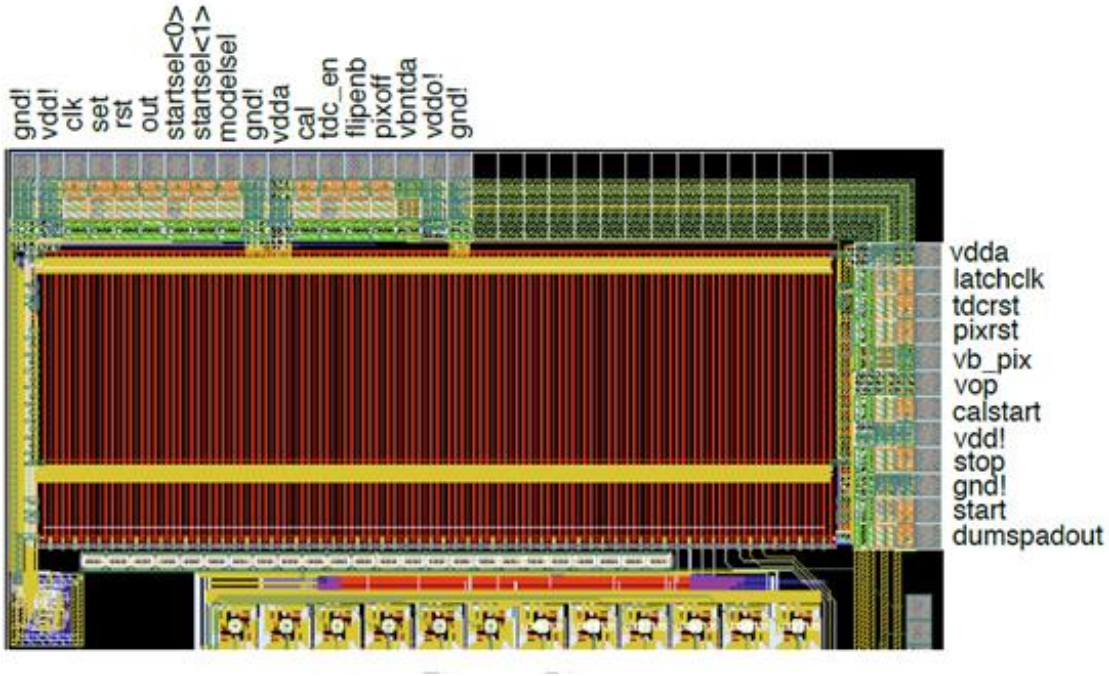

Figure 3.4: Pin Location

latchclk: latch output of the TDC;
set: set the output of the TDC;
tdcrst: reset the TDC;
pixrst: reset the SPAD, the RST shown in Figure 3.1;
vb_pix: bias voltage for the quenching resistor, the VB shown in Figure 3.1;
startsel<0>, startsel<1>: select the input to the TDC, from the SPAD, pin or other source;
flipenb: use the input to the TDC as START or STOP of the TDC;
modelsel: select the readout method, only the 127^{th} TDC or all the TDCs;
tdc_en: enables the TDC;
pixoff: disable the SPAD, the OFF shown in Figure 3.1;
out: output of the digital controller;
dumspadout: output of the dummy SPAD.

Dumspadout is the only pin that is connected to a SPAD output directly. And that SPAD is the only SPAD in the SPAD array whose output is accessible, i.e. the 128th TDC output used to measure SPAD jitter.

Vb_pix is controlled by a trimmer on the PCB for this sensor. Voltage of vb_pix can be tuned between 0 V to 3.3 V. For this project, it is kept to be 0. As a result, resistance of quenching resister is high, and the quenching time will be short. The quenching resistor is also used as the passive recharging circuit. Since the resistance is high, the recharging period is long. In all, with proper design, output of the SPAD rises fast and becomes stable after avalanche happens.

After a conversion, output of each TDC is latched and stored in a shift-register. Afterwards, the data is read out bit by bit by the FPGA from pin out mentioned above. For each TDC, its output contains 20 bits. Dependent on the frequency of the

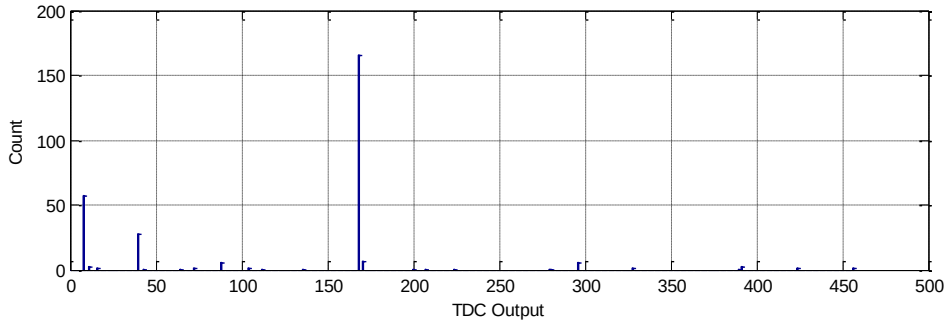

Figure 3.5: DCR Measurement with Artifact

clk signal, total data transmission time is at the level of hundred-microsecond (102 μs is reported in [17] with 25 MHz clock frequency), which is much longer than the TDC conversion time (320 ns).

3.4 Output Artifact

During DCR characterization, an artifact was detected. Since only the 128th SPAD is accessible, DCR measurement in this project is carried out by measuring the TDC output after large number of samples in a completely dark environment. With the presence of TDCs, measurement results are expected to be worse than the real DCR of SPADs. First-stage TDC output histogram of one of the TDCs after DCR measurement is shown in Figure 3.5.

The total count shown in Figure 3.5 is 298. The measurement was performed with a SPAD active time-window size of 80 ns. Total number of measurement was 10^6. DCR result is

$$DCR = \frac{1}{80 \times 10^{-9} \times 10^6} \times 298 = 3725\ Hz, \tag{3.6}$$

which is much higher than the characterization result reported in [17], i.e. < 100 Hz. It is clearly shown in the histogram that output of TDC only occurs at some particular positions. Furthermore, count of the TDC output does not decrease when V_{op} falls, even when V_{op} is set to be 0V. Therefore, it is reasonable to conclude that the measurement result is not correct.

By plotting the DCR measurement result of all SPADs in one figure, as shown in Figure 3.6, it turns out that the incorrect TDC output is not uniformly distributed throughout the SPAD array. The amount of incorrect output is constant from the first SPAD to the sixtieth SPAD. From the sixtieth SPAD, the incorrect count starts decreasing. For the SPADs at the end of the array, the counts become constant again. The amount of the artifact turns out to be related to the position of the SPAD. It is logical to suspect that the artifact is caused by a signal that propagates throughout the SPAD-TDC array.

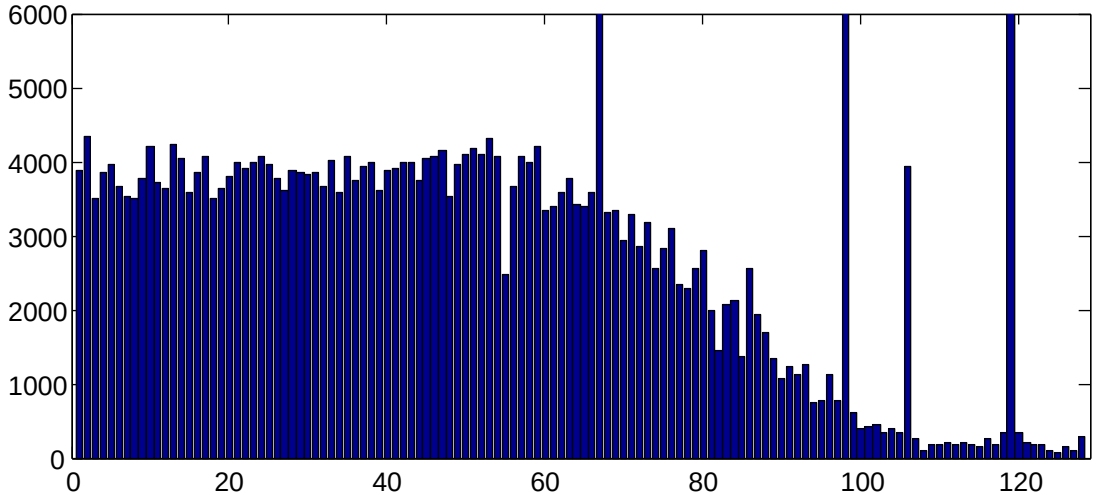

Figure 3.6: DCR Summary with Artifact

The reason that causes the artifact can be figured out with the help of the design and layout of the sensor. However, in this project, it is impossible to redesign the sensor. Thus, emphasis is put on artifact cancellation.

After further exploration, it turned out that for those incorrect counts, the second-stage TDC outputs are wrong. As discussed in Section 3.2, second-stage TDC output D_{2nd} should be less than N_{max} and larger than N_{min}. However, for those incorrect counts, D_{2nd}>N_{max}. Therefore, by filtering out outputs with incorrect D_{2nd}, the artifact can be removed. DCR measurement results after artifact removal are shown in Figure 3.7.

Total count of the same SPAD shown in Figure 3.5 now becomes 6, which generates a DCR of 75. DCR of all SPADs shown in Figure 3.7b are reasonable comparing with the report in [22]. The 67th, 98th, 106th, and 119th SPAD are the SPADs that generates large amount of DC. Their DCR results are removed from the figure. Similar effect of artifact cancellation also appears in the histogram in TDC density test, as shown in Figure 3.8.

3.5 Summary

Relevant specifications of the chip is summarized in Table 3.2. Study of the design of the chip is crucial for the setup design reported in Chapter 4. The discovery and cancellation of the artifact during chip characterization make the range detection and model verification presented in Chapter 5 and Chapter 2 possible.

SPAD	
Jitter	178.2 ps
DCR	<350 Hz

TDC			
LSB	200 205 ps	DNL	<0.6 LSB
Jitter	1.2 LSB (FWHM)	INL	<3 LSB

Table 3.2: Summary of Characterization

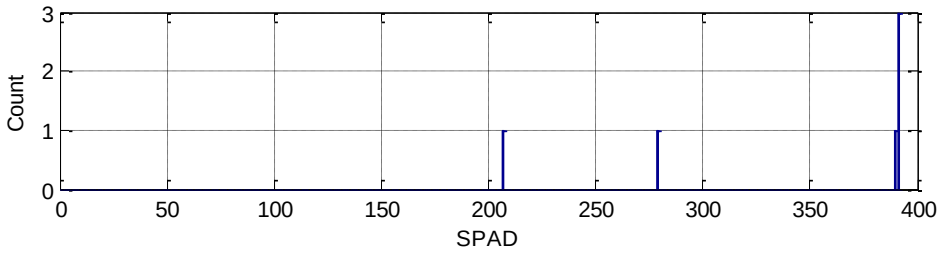

(a) DCR Measurement Histogram of One SPAD

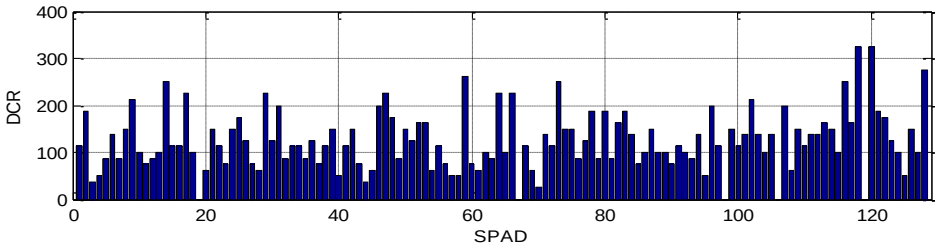

(b) DCR Measurement Result of All SPAD

Figure 3.7: DCR Measurement Result after Artifact Cancellation

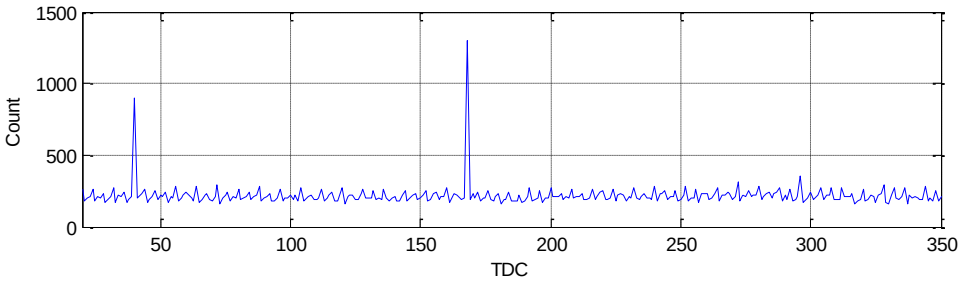

(a) Density Test Histogram Before Artifact Cancellation

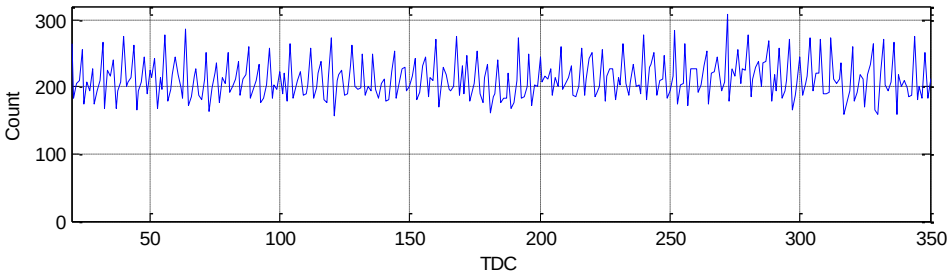

(b) Density Test Histogram After Artifact Cancellation

Figure 3.8: Effect of Artifact Cancellation on Density Test Histogram

4 Range Detector Setup

To apply the sensor discussed in Chapter 3, an electro-optical setup is required. The main goal of implementing this setup is to build a platform on which TCSPC ranging can be performed. In other words, the setup is built for principle verification. With the help of this platform, the model built in Chapter 2 can be verified; the sensor studied in Chapter 3 can be characterized.

The detector setup consists of three parts, i.e. the DAQ system, the data processing procedures, and the optical-mechanical structures. In this chapter, the design of each part will be presented in Section 4.1, 4.2, and 4.3, respectively.

4.1 Data Acquisition

The DAQ of the 3D range detector was designed by Dr. Shingo Mandai based on a Xilinx Virtex 5 FPGA. Data transmission from the FPGA to the PC is based on Ethernet connection and the Power PC Core in the FPGA. In this section, however, the Ethernet connection will not be covered. The focus is put on the DAQ between the sensor and the FPGA.

A simplified block diagram of the VHDL program for the DAQ from the sensor is shown in Figure 4.1. The DAQ is basically execute by a state machine. The states are the Reset State, the Start State, the Evaluate State, the Latch State, the Getdata State, the Readout State, the Wait State, the Synchronization States, and the Set State. Waveform of the signals after stabilization is shown in Figure 4.2.

After the first DAQ cycle, the DAQ process becomes stable. For each DAQ cycle, the first state is the Start State, in which the TDCs and SPADs are turned on and reset. The following state is called the Evaluate State. This state contains several clock cycles. After the first clock cycle, SPADs are ready to work. The second and third clock cycles are the sampling cycles, or the time window, chosen as 80 ns in this project. At the end of the third clock cycle, STOP signal rises, for the first stage TDC, the VCO phase detector and counter are frozen by the STOP signal. For the second-stage TDC, data conversion starts and the conversion time costs 320 ns. After the Evaluation State, the Latch signal rises and Latch State starts. The TDC output is stored. With the ChipSet signal rises one clock cycle afterwards, data of the chip is frozen. The Readout State comes right afterwards.

During the Readout State, the FPGA reads out the data from the sensor bit by bit. After finishing reading out all the data of one TDC, the system sends the data to the PPC core. Meanwhile, the system goes into Wait State until the feedback from the PPC core indicates that the data transmission is finished. At the end of the Wait State, the system checks the address of the TDC. Before finishing reading all the 128 TDCs, the system will go back to the Readout State. After all the 128 TDCs have been read,

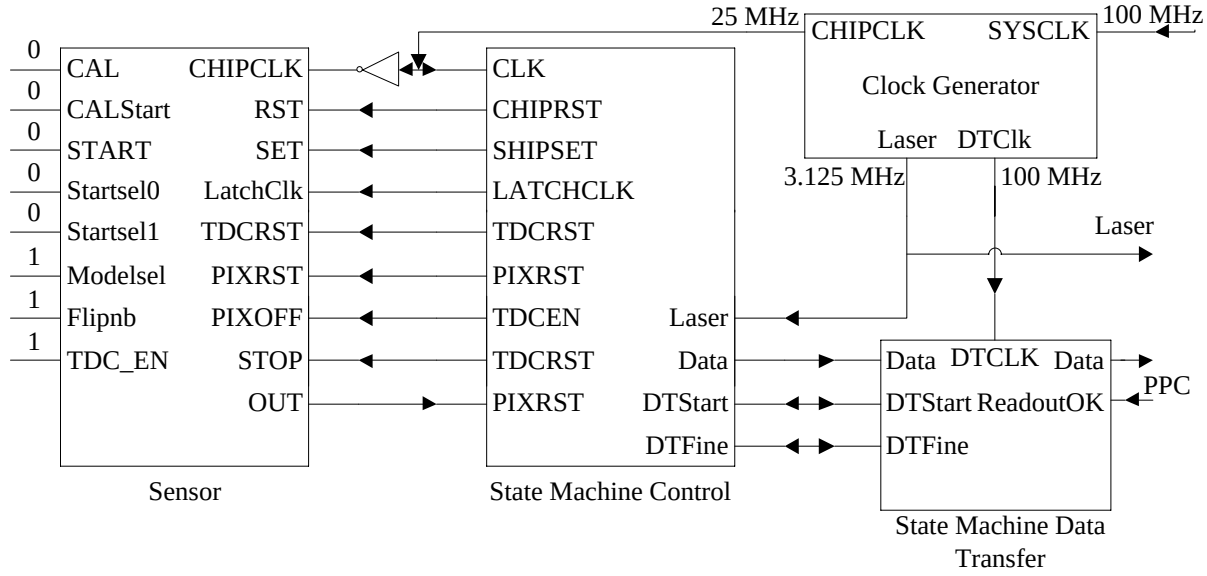

Figure 4.1: Block Diagram of DAQ from Sensor to FPGA

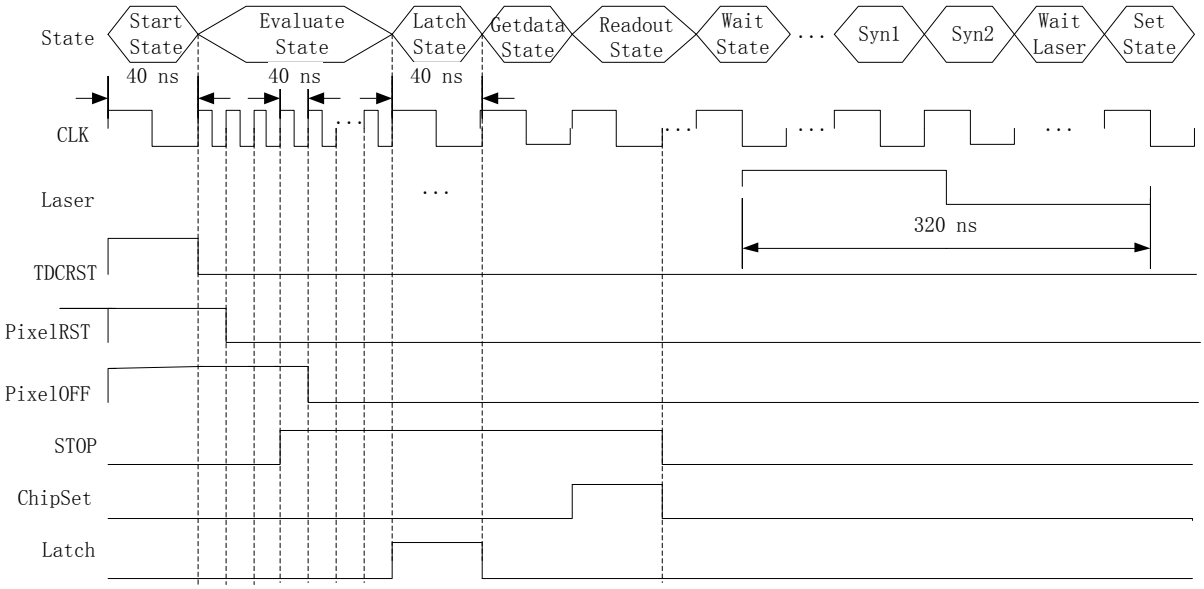

Figure 4.2: DAQ Waveform

the system goes into the Synchronization State, so that time window of each DAQ cycle opens at the same time relative to the laser trigger. The state contains the Syn1 state, the Syn2 state, and the Wait Laser state shown in Figure 4.2. The Syn1 and Syn2 states detect the falling edge of the laser trigger signal. In the Wait Laser state, a delay is set according to target distance based on the gating principle discussed in Section 2.7. The last state of a DAQ cycle is the Set State, in which signals are initialized. The DAQ cycle will continue until the Ethernet connection is stopped by the user, since the PPC core will not generate ReadoutOK signal anymore.

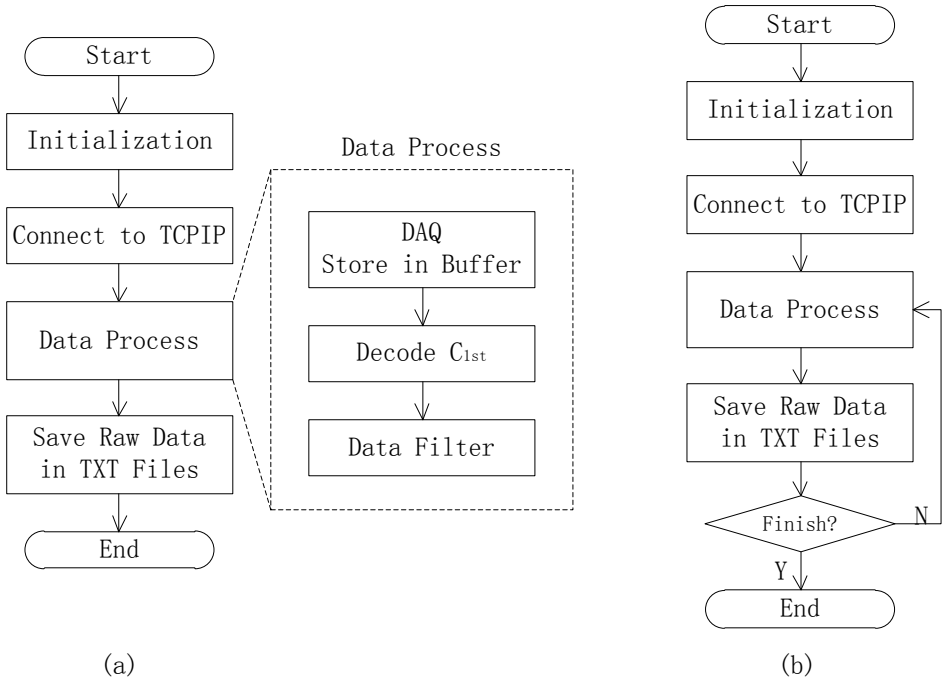

Figure 4.3: Flow Chart of PC DAQ

4.2 PC Data Acquisition

TDC output is transmitted through Ethernet from the FPGA to the PC. The data is decoded and stored on PC. Several processing steps are performed afterwards. In this project, PC DAQ and data processing are separated. In this section, only the DAQ process is presented. The data processing procedures are reported in Chapter 5.

Two main concerns in the design of the PC DAQ are as follows:

1. The DAQ should not cause any error in range detection or system characterization.

2. The DAQ results should be easily accessed by processing procedures afterwards.

Other concerns are the DAQ speed, data size, simplicity, etc.

Based on the application, two PC DAQ methods are designed. Flow chart of PC DAQ for normal range detection is shown in Figure 4.3 (a). After initialization process, the software is connected to Ethernet card. All data received will be put into a buffer. The buffer size is determined by the number of samples required for the range detection. After all the data are collected, a simple data processing procedure will be performed to filter the data. In this step, output of the first-stage TDCs' VCO counter will be calculated. Data will be filtered base on the calculation results. The reason is that the system runs in photon starving mode, only very few of the TDC output results represent the TOF, while all the rest are just the initial value of the TDC output. The filtering process effectively reduces the size of data. After filtering, all effective outputs are stored in TXT files.

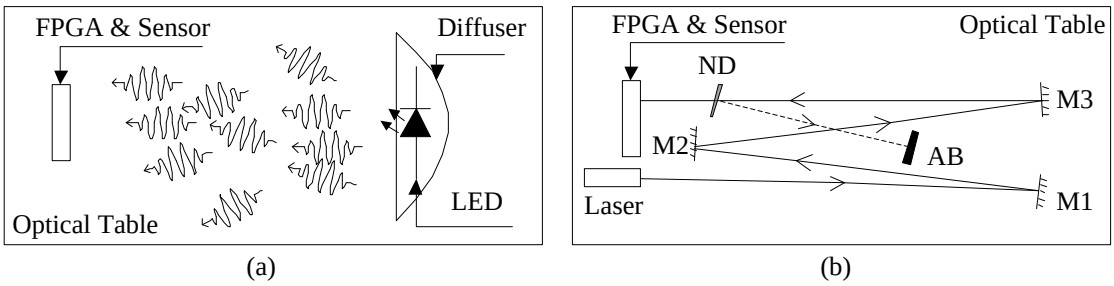

Figure 4.4: Light Path of TDC Density Test and Shout-distance Range Detection

The flow chart of PC DAQ for TDC density test is shown in Figure 4.3 (b). For TDC density test, large amount of samples are required. However, the space available for the buffer is limited. So data should also be filtered and stored separately during the DAQ. To acquire stable result and high efficiency, the buffer size should be as large as possible. But for the sake of convenient operation, small buffer sizes are preferred. In this project, the buffer size is chosen as 500000. By changing the number of sampling cycle, users can acquire as much data as they want.

Since the purpose of implementing this range detector setup is principle verification, speed of the DAQ is not optimized in this project. In normal situation, the DAQ collect, process, and store 40000 TDC data in about 40s.

4.3 Optical and Mechanical System

As a principle verification setup, the optical-mechanical system utilized in this project are designed to be compact. The optical system contains several laser mirrors, a neutral density filter, and an optical table. The mechanical system is introduced in long-distance range detection, the main equipment are tripods. Top view of optical system setups used in TDC density test and short-distance range detection are shown in Figure 4.4.

For TDC density test, low-irradiance uniformly distributed light is used. In this project, a blue light emission diode (LED) is employed as the light source. For simplicity, it is assumed that light generated by LED is uniformly distributed in time. However, LED photon generation cannot be regarded as uniform in space. Therefore, a diffuser made by aluminum foil is used to unify the light, so that all SPADs in the sensor have the same amount of photon injection.

In short-distance range detection measurement, distance varies between 20 cm to 300 cm. However, length of the optical table is only 178 cm. So two more mirrors are used to fold the light path with extra reflections for distance longer than 178 cm, as shown in Figure 4.4 (b). To keep the sensor functions in photon starving mode, a neutral density filter is placed in front of the sensor to reduce the light intensity, shown in Figure 4.4 (b) as ND. To avoid the photon reflected by the neutral density filter injecting on the sensor, a light absorber, the AB in Figure 4.4 (b), is placed in the light path of the filter-reflected light to absorb the reflected photons. Photos taken during the measurement that show the actual optical system used in short-distance

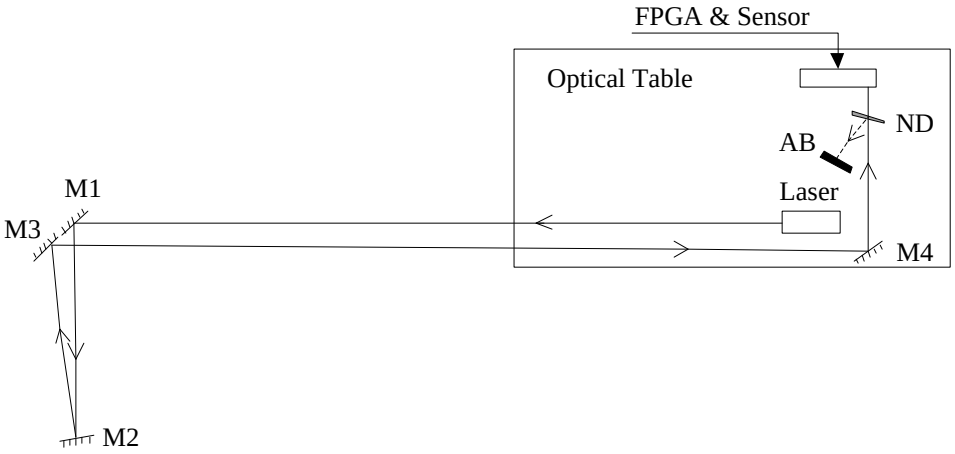

Figure 4.5: Set-up for Long-distance Range Detection

range detection are shown in Appendix I Figure I.1, Figure I.2, and Figure I.3.

For long-distance range detection measurement, i.e. from 3.5 m to 60 m, dimension of the optical table is far less than enough even with extra reflections. However, for the sake of stability against vibration of the ground, key components of the system, i.e. the laser and the sensor, should be placed on the optical table. Since it is not practical to move the optical table, to get extra space for long-distance detection, three tripods are used to build the light path. Top-view and light path of long-distance range detection are shown in Figure 4.5.

With the set-up in Figure 4.5, distance measurement can be extended up to 60 m. The limitations for the distance are the length of the building where the measurement took place and the non-ideal laser collimation. Mirror M1, M2, M3 are mounted on three different tripods. Mirror M4 is mounted on the optical table. M1 and M3 are placed close to each other. Distance between M1 and M2 can vary from 0.1 m to about 54 m.

The set-up can be further simplified by removing M4 and putting the FPGA and sensor board right next to the laser as it is in short-distance detection. However, for long-distance detection with laser and mirrors, this simplification is not preferable. Because the most difficult and time consuming work during measurement is to align the laser spot on the sensor. Size of the detector is 2.45 mm $\times$ 3.65 mm, according to the design document written by Dr. Shingo Mandai, while the distance between the laser and M1 is about 6 m. With the help of M4, the distance between the last mirror and the sensor becomes 1.2 m, which makes the alignment much easier. The neutral density filter ND and absorber AB play the same role as they do in short-distance detection. Photos taken during the measurement of the setup are shown in Appendix I Figure I.4.

5 Range Detection Results

One of the main targets of this project is to implement a 3D range detector that utilizes TCSPC principle. Measurement results of the detector have been used in Chapter 3 to verify the model and in Chapter 3 to perform chip characterization. In those sections, TOFs are not calculated and the TDC outputs are used directly. In this chapter, the detector is used to perform range detection. Therefore, the TDC outputs are converted distance.

For range detection, TOF requires precise TDC LSB values. For the TDC used in this project, the LSB should be calibrated. The calibration method is presented in Section 5.1. Afterwards, TOF values are calculated from the histogram obtained during the measurement, which directly leads to range information. The algorithm for extracting range information from the histogram is presented in Section 5.2. Finally, short-distance and long-distance range detection are presented and analyzed in Section 5.3 and 5.4.

5.1 TDC LSB Calibration

In Section 3.2, the estimation of TDC LSB has been discussed. However, in the range detection measurement, we cannot use the TDC LSB estimation results directly. The reason is that the TDC LSB varies significantly when input light intensity changes.

The LSB variation is mainly caused by the design of power distribution in the chip. When large volume of photons impinge the sensor, including both the signal photons and noise photons, more SPADs are triggered. Since the SPADs' outputs are connected to the start signal of the TDCs, more TDCs operate in this case. As a result, more current is needed for the VCOs to run. However, current capability of the chip is limited. Moreover, resistance of the power supply network is not negligible. Therefore, when the light intensity rises, IR drop increases, which reduces the voltage supply to each TDC. As a result, the frequency of the VCO reduces and so does the TDC resolution.

TDC LSB variation is shown in Figure 5.1. As it is shown in the figure, when light intensity increases, TDC LSB variation can be more than 40 ps. Moreover, LSB variation of those TDC located in the middle of the TDC array is higher than those at both ends, which is an expected behavior caused by IR drop.

With the reason of LSB variation found, it is possible to predict and calibrate the LSB during range detection. In this section, the LSB variation is emulated with a third-order polynomial fit function. To derive the correct fit function, a set of measurements were performed to measure the LSB of each TDC under different light intensities.

After the measurements, a third-order polynomial fit is performed to each TDC based on its LSB results. Measurement results and plot of the fit function of the first

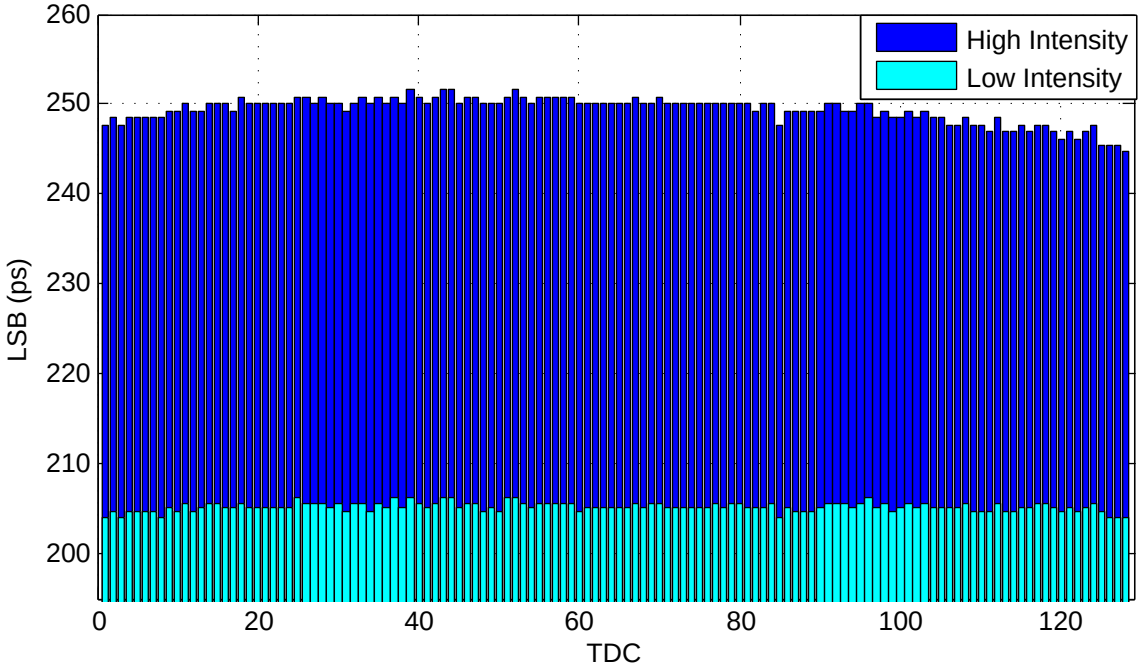

Figure 5.1: TDC LSB Variation

TDC is shown in Figure 5.2. During the range detection, total number of detected photons of all TDCs is counted. Number of detection per pixel per sample is

$$N_{per\ pixel\ per\ sample} = \frac{N_{total}}{N_{pixel} \cdot N_{Samples}}. \tag{5.1}$$

It will be used as the input of the third-order polynomial function to calculate the LSB of each TDC. For the targeted application, the range detector works in photon-starving mode. IR drop variance caused by photon intensity difference is not significant. Therefore, LSB has a constant value, which is clearly shown in Figure 5.2.

5.2 Range Calculation

The ultimate goal of implementing the range detector is, indeed, to detect the distance. However, the distance calculation is much more complicated than simply multiplying the TDC output with the speed of light. In this project, range calculation procedure is summarized in the flow chart shown in Figure 5.3. The procedure can be divided into three main processes, i.e. TDC output processing, LSB calibration, and total delay measurement. The results of all these processes are then used to calculate the distance. In this project, all of these procedures are performed with MATLAB off-line, however, a real-time version of the data process could be envisioned.

The most important process in range detection procedure is to find out the TOF position from TDC output histogram. According to Section 4.2, raw TDC outputs acquired by the PC DAQ program are stored in TXT files on the PC. To calculate

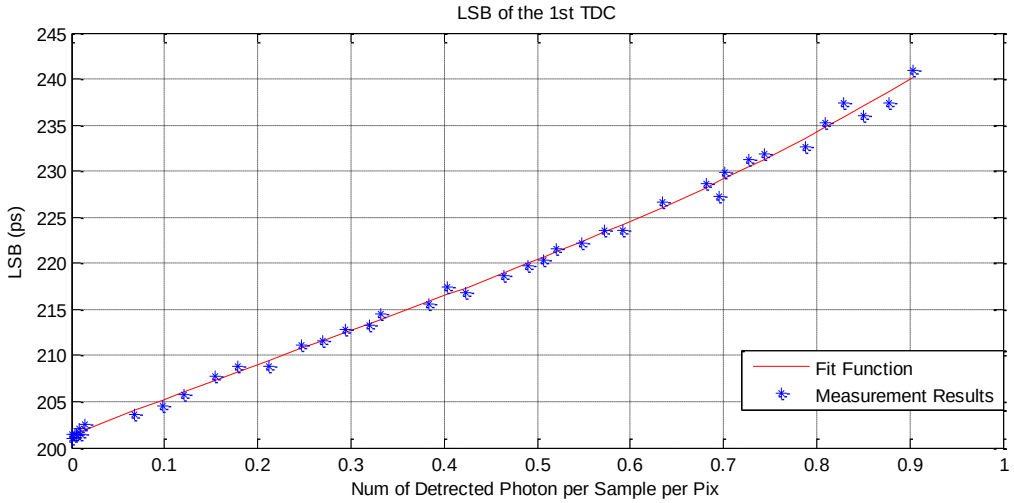

Figure 5.2: LSB Variation of the First TDC and Third Order Polynomial Fit

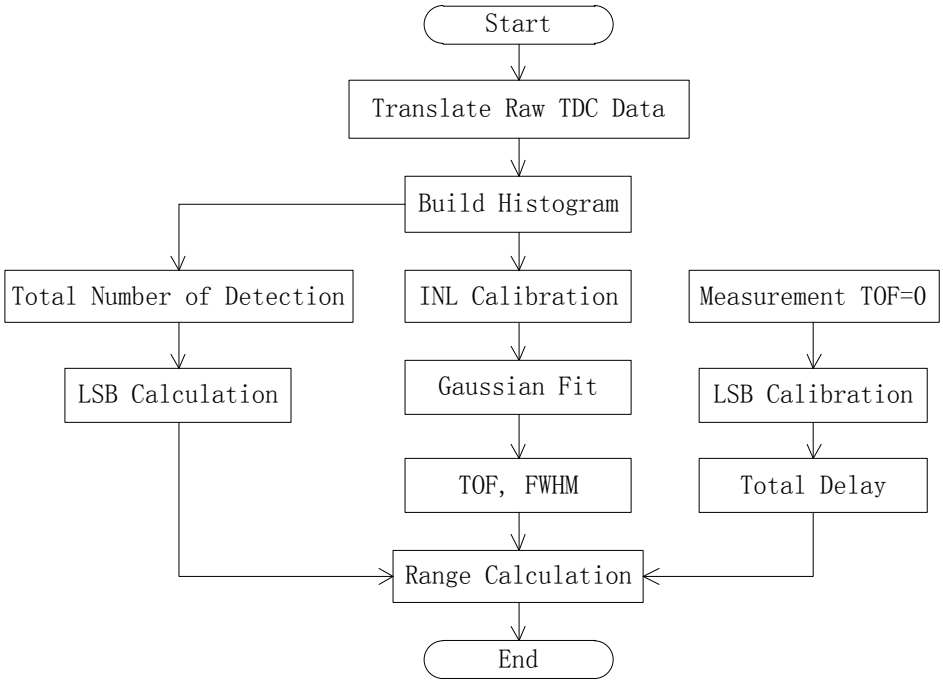

Figure 5.3: Flow Chart for Range Calculation

the TOF, the first step is to read and transform these raw data into number of TDC LSBs. Output of each TDC contains 32 bits. Define the i th bit of the output of the first-stage VCO counter as $C_{1st,i}$. Similarly, define the i th bit of the first-stage VCO phase detector, the second-stage VCO counter, the second-stage VCO phase detector, and the address of TDC as $P_{1st,i}$, $C_{2nd,i}$, $P_{2nd,i}, A_i$, respectively. Format of data of one

of the TDCs is shown in Table 5.1.

	1	2	3	4	5	6	7	8
1	0	$C_{2nd,4}$	$C_{2nd,3}$	$C_{2nd,2}$	$C_{2nd,1}$	$C_{2nd,0}$	$P_{2nd,3}$	$P_{2nd,2}$
2	$P_{2nd,1}$	$P_{2nd,0}$	$C_{1st,5}$	$C_{1st,4}$	$C_{1st,3}$	$C_{1st,2}$	$C_{1st,1}$	$C_{1st,0}$
3	$P_{1st,3}$	$P_{1st,2}$	$P_{1st,1}$	$P_{1st,0}$	0	0	1	A_7
4	A_6	A_5	A_4	A_3	A_2	A_1	A_0	0

Table 5.1: Data Storage Format

After data translation, output of the first-stage TDC is calculated as follows,

$$TDC_{1st} = 8 \times C_{1st} + P_{1st}, \tag{5.2}$$

with C_{1st} the decimal value of first-stage TDC VCO counter and P_{1st} decimal output of the first-stage VCO phase detector thermometer code.

Histogram of each TDC is built based on the results of TDC_{1st}s. INL results acquired from the density test are then applied to the TDC_{1st}s for calibration. Afterwards, a Gaussian fit is performed to all the histograms. The peak position of the Gaussian fit functions will be used as the TOF positions. The FWHMs of the Gaussian fit function will be used as the FWHMs of the TOF detections.

Before calculating the distance, two more procedures are required. The first one is to calculate the LSB of each TDC. As discussed in Section 5.1, a polynomial fit function has been generated from special measurements of LSB. The information required for LSB calculation are the N_{total}, N_{Sample}, and N_{pixel} in Equation 5.1. N_{total} is the total number of counts of all TDCs, which can be calculated from the histograms. N_{Sample} is the number of samples during the measurements to build the histograms. It is set as a constant before range detection measurements. N_{pixel} is the number of pixels that operates during the measurement. In this project, $N_{pixel} = 128$. From Equation 5-1, $N_{per\ pixel\ per\ sample}$s can be calculated. Each TDC then has its own calibrated LSB.

The second procedure required is to measure and calculate of total delay of the system. The result will be used to find out the TDC output that corresponds to zero distance. The measurement is performed by placing the laser so close to the sensor that the TOF can be neglected. With the same process of TOF calculation and LSB calibration mentioned in previous paragraphs, the total delay will be calculated as follows:

$$T_{delay} = T_{Laser-Win} - TDC_{out} \times LSB, \tag{5.3}$$

with $T_{Laser-Win} = 140\ ns$ the and TDC_{out} output of the TDC.

Finally, with the TOF position, the calibrated LSB, and the total time delay, distance of the target is calculated as follows:

$$distance = \frac{c}{2}(T_{Laser-Win,i} - T_{delay} - TDC_{out} \times LSB), \tag{5.4}$$

with $T_{Laser-Win,\ i}$ the time interval between the laser trigger signal and the end of time window, which varies from 140 ns to 500 ns depending on the preset time delay in the Synchronization State discussed in Section 4.1.

A remark in distance calculation is that in this project, the SPAD output is connected to the start signal of the TDC. So TDC output is actually $T_{Window} - TOF$.

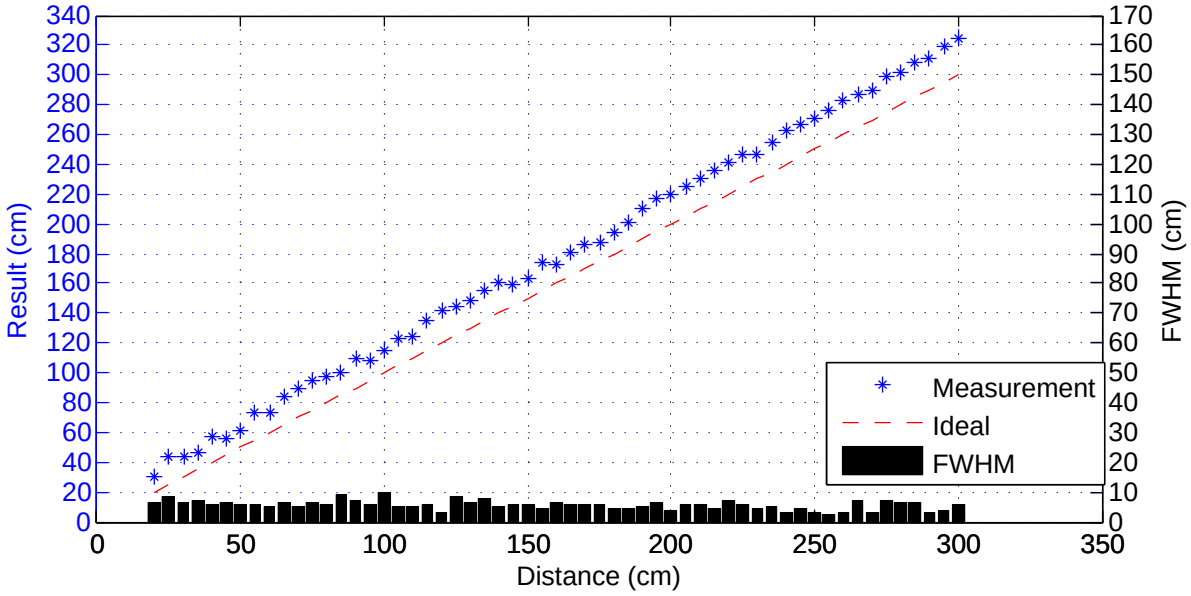

Figure 5.4: Short Distance Measurement Result of the First Detector

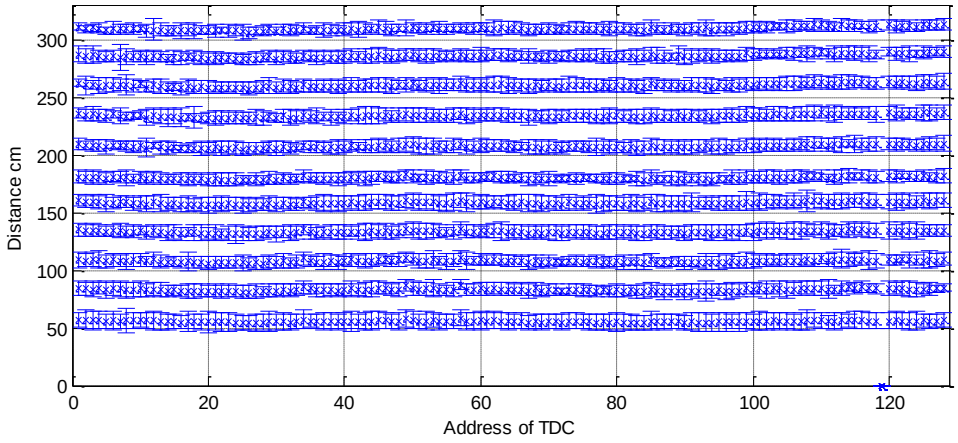

Figure 5.5: Short Distance Measurement FWHM of All Detectors

5.3 Short-distance Measurement

Short-distance range detection was performed with the setup shown in Figure 4.4 (b). Distances from 20 cm to 300 cm with an interval of 5 cm were measured. Reference of the measurement used as the actual distance was measured by a PLR 15 laser rangefinder produced by BOSCH. Accuracy of the rangefinder is 1 mm. Measurement result of the first detector (SPAD-TDC unit) as a function of actual distance is plotted in Figure 5.4.

As shown in Figure 5.4, the measurement result of the first detector matches with the ideal curve. However, an offset exist in the measurement. The reason can be the error in delay measurement or setup. The FWHM of the first detector is between 2.1

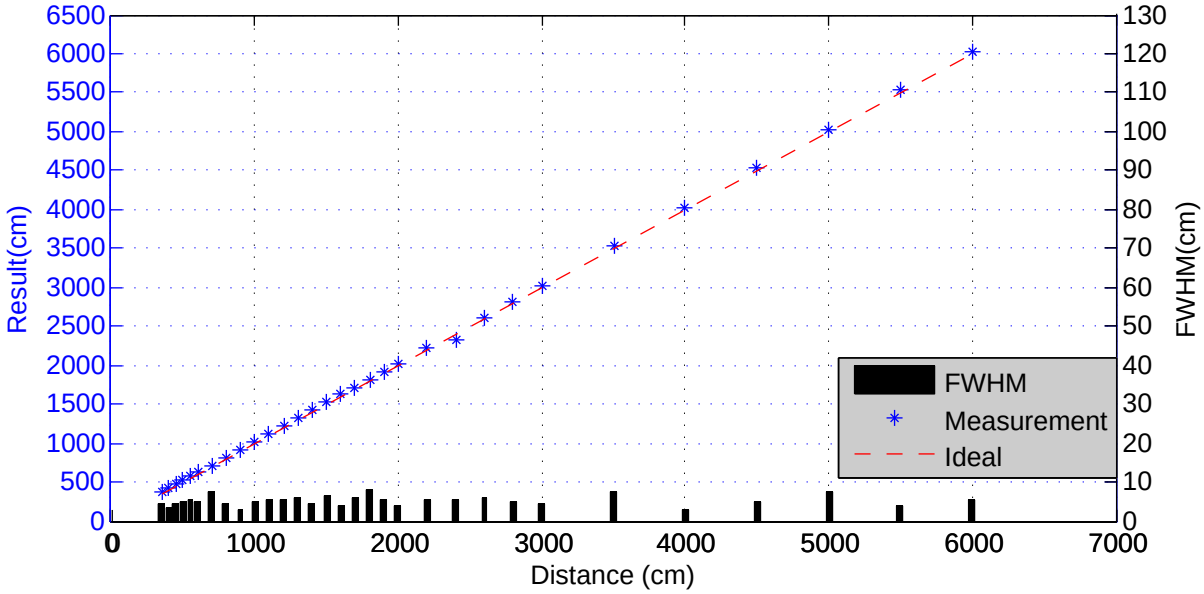

Figure 5.6: Long Distance Range Detection Result of the First Detector

cm and 10.0 cm, with a mean value of 5.2 cm, which is actually worse than the special resolution calculated with TDC LSB. Furthermore, mean value of the FWHM of the result is already larger than the special interval used in the measurement. As a result, only a set of measurements are used in Figure 5.5 to show the uniformity of the detector array.

As shown in Figure 5.5, range detection results of the detectors in the array are uniform. The worst-case distance result mismatch among all the detectors is measured to be 7.2 cm, with a mean value of 5.6 cm.

5.4 Long-distance Measurement

The setup of long-distance range detection has been reported in Section 4.3. Distance measurements from 3.5 m to 60 m were performed. As reference of the measurement we used the BOSCH PLR 15 laser rangefinder introduced in Section 5.3. The accuracy of the range finder is 1 mm. However, in long-distance range measurement, the actual accuracy of the reference is worse than 1 mm. The reason is that the physical alignment at long distance is very difficult with the current setup. Measurement results of the first detector with FWHM are shown in Fig 5.6.

As shown in Figure 5.6, measurement results match the ideal distance value. The FWHM of the measurement error varies between 3.0 cm and 7.9 cm with a mean value of 5.1 cm. Range detection performance is constant throughout the distance range, which verifies the effect of gating technology discussed in Section 2.7. Confirmation of range detection uniformity is shown in Figure 5.7. As shown in the figure, the range detection results of all the detectors are uniform. The worst-case mismatch among all range detection results is 11.6 cm. A offset caused by setup error can be observed from Figure 5.7b.

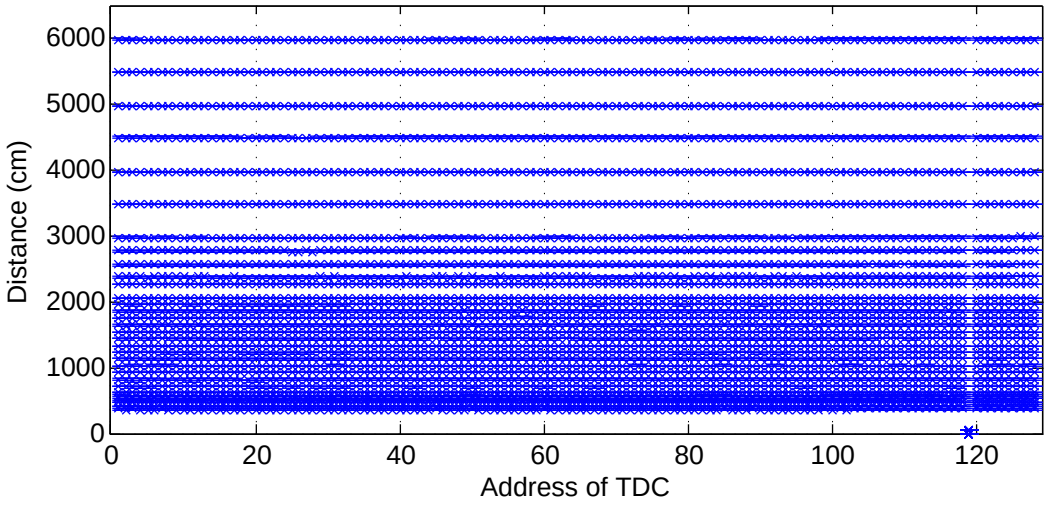

(a) Detection Result at All Distance

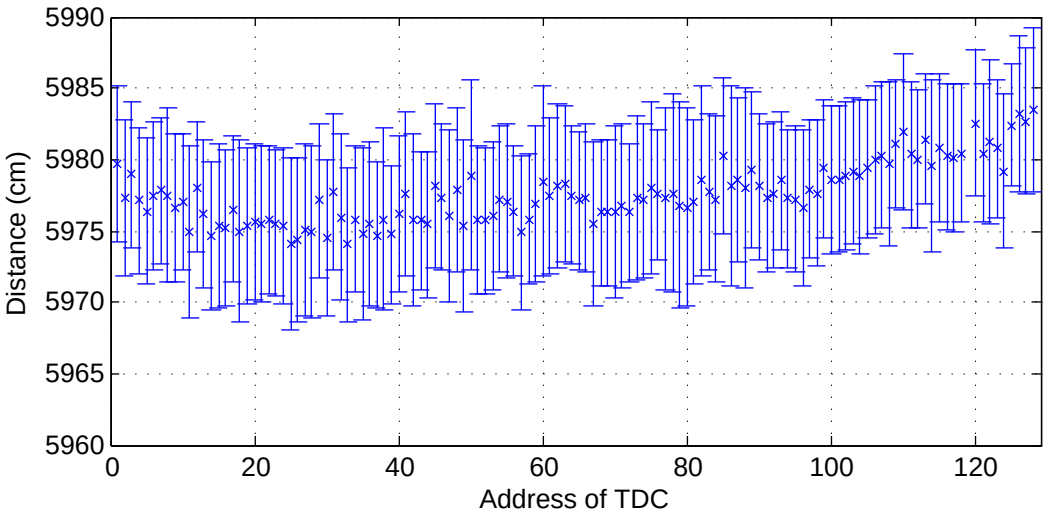

(b) FWHM of All Detectors at 60 m

Figure 5.7: Long Distance Range Detection Results of All Detectors

5.5 Summary

Range detection measurement results reported in this chapter proves that the principle and design of the setup is correct. The sensor can uniformly generate reliable distance measurement results with accuracy at the level of 10 cm. However, for TCSPC systems, theoretically, special precision is higher than the accuracy calculated based on TDC resolution, which is about 3 cm in this project. In the setup of this project, issues that cause the non-ideality are as follows:

1. The sensor chip is not specially designed for range detection. Power supply rejection ratio, according to the designer, is low. Temperature variance is not negligible. Both of them were not calibrated in this project.

2. External trigger is used for the laser, which generates unknown jitter behavior of the optical signal. The laser is used as a black box. No optical measurement equipment is available to characterize it in this project.

In all, as discussed before, the setup in this project is built for principle verification, sensor characterization, and model confirmation. More detailed design should be done in the future to optimize the performance of range detection, which is not included in this project.

6 Conclusion

6.1 Summary

In the course of this thesis project, a TCSPC range detector was modeled, characterized, implemented, and operated.

Models built in this project are the theoretical model, the random model, and the performance prediction model. The theoretical model is based on [10]. By introducing the distortion caused by the TCSPC principle, the model has a better consistency with the real measurement than the original one. The random model is based on the statistical behavior of the TCSPC process. In this model, data is processed only by random number generators. The output of this model represents the behavior of the ideal TCSPC range detector. The performance prediction model is designed on top of the theoretical model. It produces the probability of correctly detecting a signal peak from the histogram at a particular distance. The result can be used to qualitatively describe the system performance. All these models have been verified with measurements. The verification results show that the theoretical model and the random model match the reality. The performance prediction model matches the behavior of the setup implemented in this project. However, verifications with more degree of freedom should be performed for thorough verification.

The characterization mainly focuses on specifications that are related to the application. Restricted by the available equipment and information accessibility, characterization of the laser and the SPAD was mainly based on user manual and literature. Only the timing jitter was obtained from measurement. DNL, INL, and LSB characterization of the TDC was done using TDC density test. However, as discovered in the project, the TDC output should be filtered and calibrated. An artifact caused by an unknown signal that propagates through the chip was founded and successfully removed. LSB variation under different light injection intensity caused by the layout of the chip was measured and roughly calibrated. The characterization results are proved to be correct.

The setup implementation can be divided into two parts, i.e. the hardware and the software. Hardware setup in this project is basically used to construct the optical path, which was designed to be concise. Software design includes DAQ and data processing. Major part of the DAQ was designed by the original designer of the sensor, while the data processing part is the original work of this project. Data processing starts from collecting data from the Ethernet, followed by data filtering and data storing. TDC output artifact cancellation and TDC LSB calibration mentioned in the previous paragraph are also included. Finally, range information is extracted from the TDC outputs by one of the data processing software. By checking the original data received at the Ethernet interface, the DAQ was confirmed to be correct. By comparing the range extracted information with distance measured by reference instruments, data

processing part was verified.

Operation of the range detector was carried out in the form of distance measurement. The measurement is composed of short-distance and long-distance range detection, from 0.2 m to 60 m. Distance accuracy achieved during the measurement was at level of five to ten centimeter. Performance of the detector thorough out the distance under detection was constant. Behavior of each SPAD-TDC component was observed to be uniform. As the final test of the range detector, results of the measurement prove that the model and the implementation of the setup were correct.

6.2 Future Work

After the study of the whole system of TCSPC rangefinder, complete knowledge and experience has been acquired. Potential future improvement based on current system is limited. Future work should be focused on re-design the whole system. According to the results of this thesis, experience acquired in [10], [21], and knowledge summarized in [2], suggestions for future design are the followings:

For the sensor, the one used in this project was not designed for the application. It was designed as a new TDC array. The SPADs were designed to be used as the random signal generator of the TDCs. Only one pin was designed for data transmission, which has become the bottle neck of the speed of detection. Power distribution of the chip was not optimized, resulting in low PSRR and VCO frequency variation. For future design of the sensor, suggestions are as follows:

1. TDC design can be simplified. One-stage TDC with LSB of 200 ps is enough for automotive long-distance range-finding applications. PLL is preferred.
2. A D flip flop should be placed between the TDC and the SPAD output to make the TDC edge-triggered rather than level-triggered. This will help remove the reset peak and reduce the power consumption.
3. FF of the SPAD should be increased. Peak of PDP should be placed far from the peak of solar spectrum. For applications with 100-m range, wavelength region with all solar radiation absorbed by the atmosphere can be used, as shown in Appendix C Figure C2.
4. Silicon photon multiplier (SiPM) is preferred to be used as the SPD.
5. On-chip digital signal processor (DSP) should be implemented to compress the data and perform real-time control.
6. More pins should be added for data transmission.
7. Power distribution should be carefully designed.

For the laser, the one used in this project is not preferable. The wavelength is near ultra violet, which is dangerous to use. The optical energy of each laser pulse is low. The timing jitter is not negligible when external trigger is used. In future design, selection of the laser should concern the followings:

1. Wavelength should be chosen within infrared region. In this region, the laser is much safer to use and the wavelength is far from the peak of solar spectrum.
2. Energy of each pulse should be high enough. Repetition rate of the laser should match the sampling rage of the detector.
3. Pulse width of the laser pulse should be much higher than the SPAD jitter. So the SiPM can filter out the time-uncorrelated photon arrival.
4. Jitter of the laser should be low.

For the setup, the implementation in this project is a concise version. In future design, more elements should be added. The most important component is the lens. For a detector array, cylindrical lens should be used. In the simplest setup, a lens adapter should be design. Possible design of lens adapter is shown in Appendix H Figure H1. Another important component of the setup is the optical filter. A band-pass optical filter should be selected according to the center and deviation of the laser bandwidth. Last but not least, a new PCB should be designed for the sensor for better performance.

Simulation Flow Charts

A

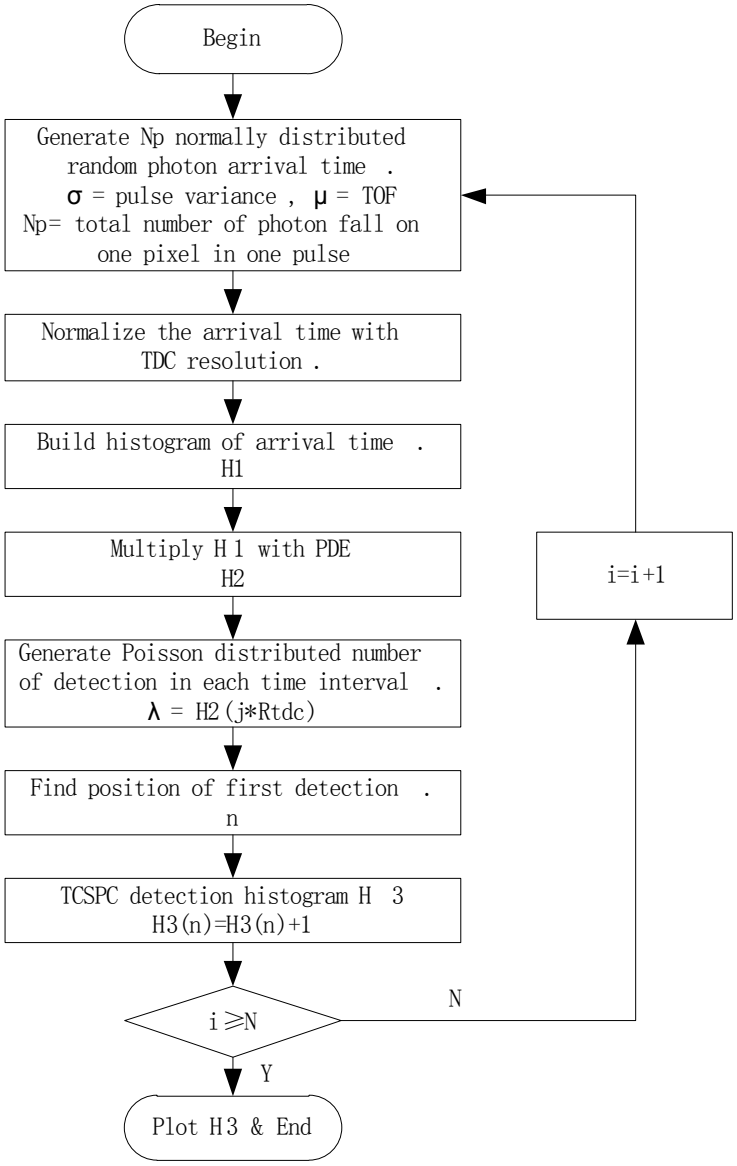

Figure A.1: Flow Chart for Random Simulation in Step 1

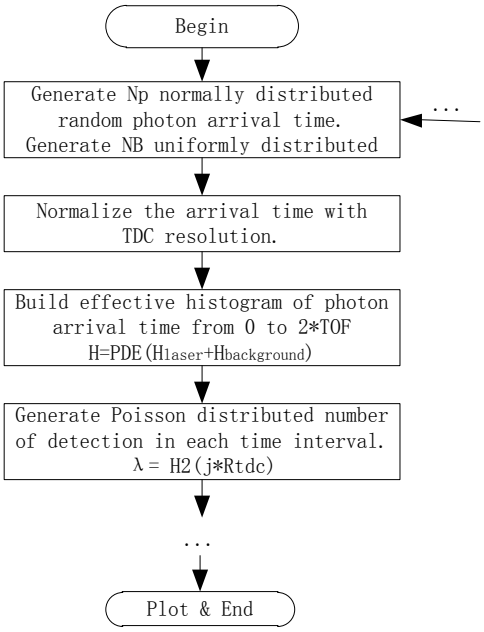

Figure A.2: Flow Chart for Random Simulation in Step 2

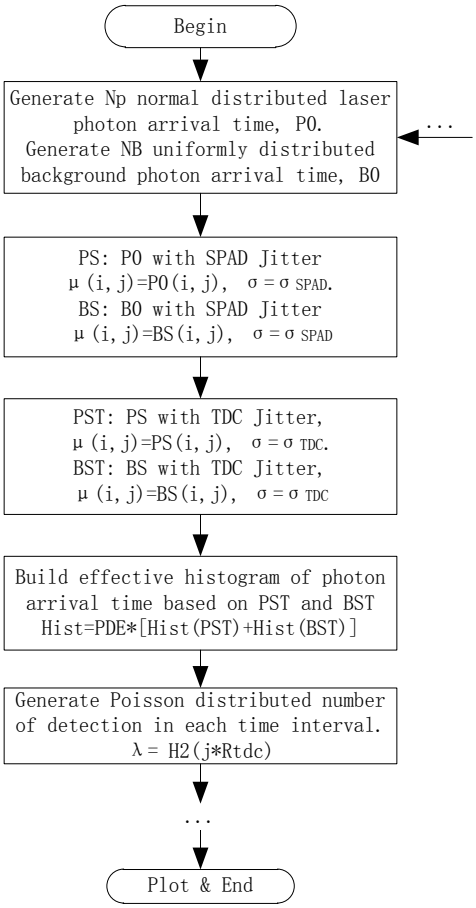

Figure A.3: Flow Chart for Random Simulation in Step 3

Simulation Results and Verification

B

Note: Simulation results in Figure B.1 to B.4 are performed with the following specifications: TDC Resolution = 20 ps, PDE=1%, number of detection = 2000, detection duration = 500 ns, signal wavelength = 405 nm, signal FWHM=44.8 ps, ambient photon rate = 1.17×10^{10}. For results in Figure B.3 and Figure B.4, jitter of the SPAD and TDC are set to be 80 ps (FWHM)

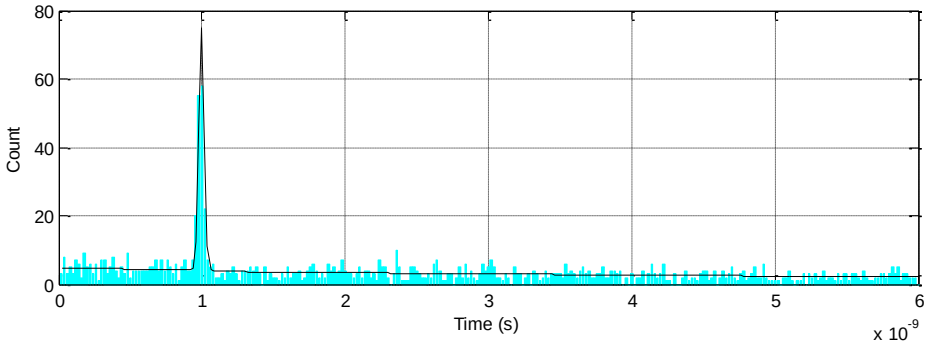

(a) TOF=1 ns

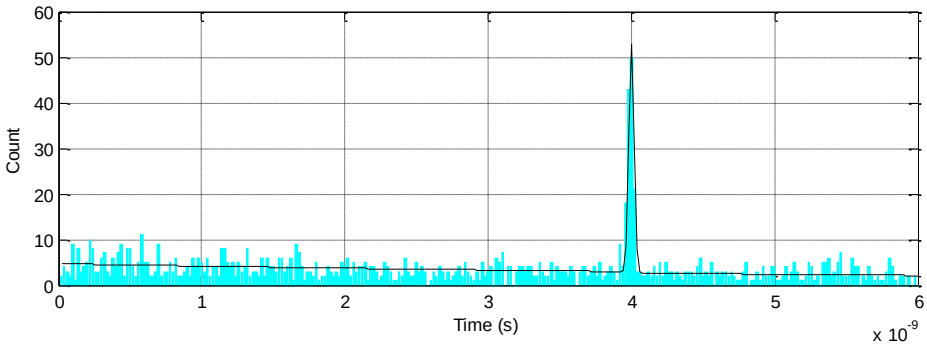

(b) TOF=4 ns

Figure B.1: Simulation Result of Step 2, M=0.1

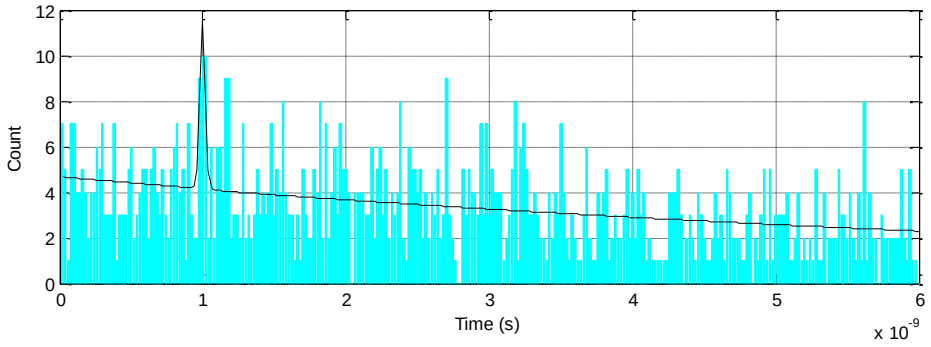

(a) TOF=1 ns

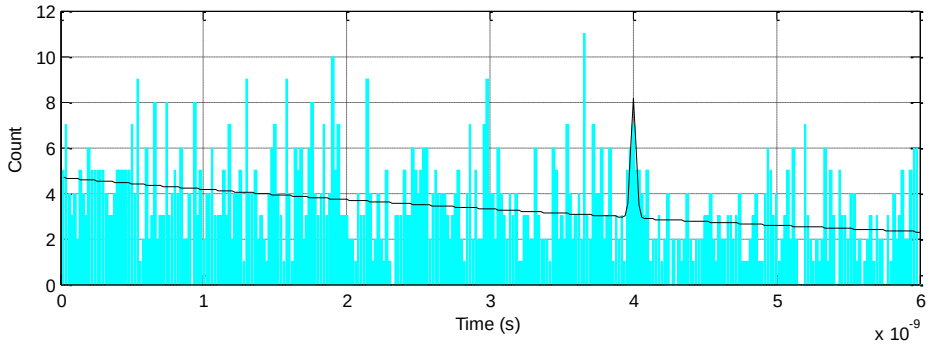

(b) TOF=4 ns

Figure B.2: Simulation Result of Step 2, M=0.01

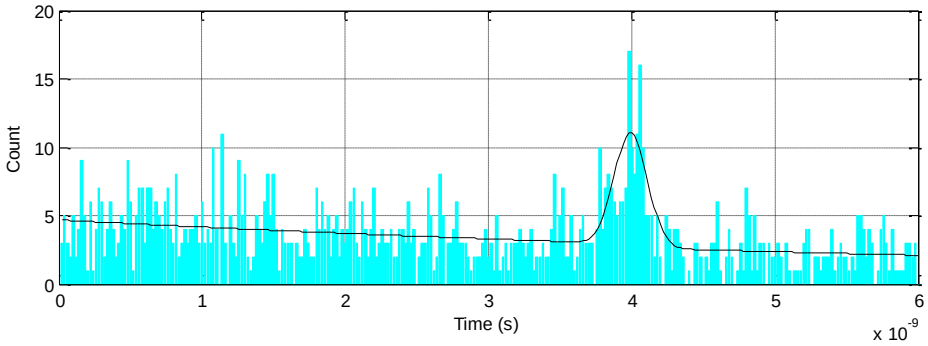

Figure B.3: Simulation Result of Step 3, M=0.1

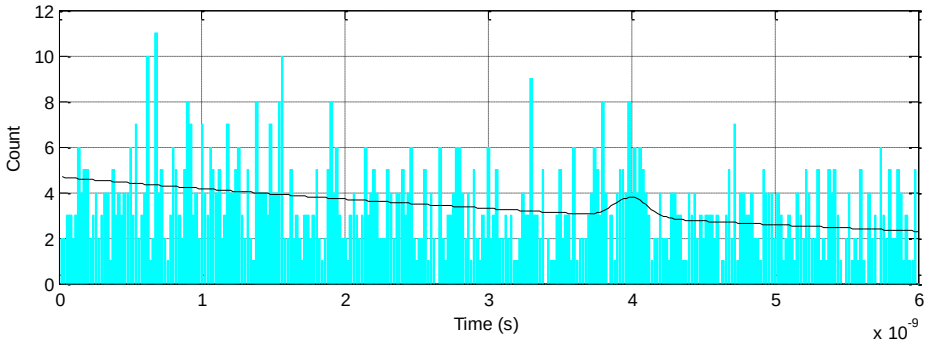

Figure B.4: Simulation Result of Step 3, M=0.01, TOF=4 ns

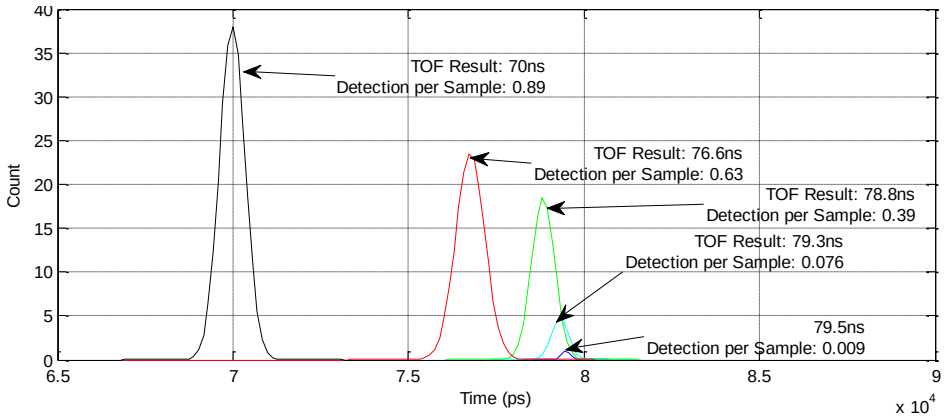

Figure B.5: Measurement Result of Distortion Caused by Input Photon Intensity Variation

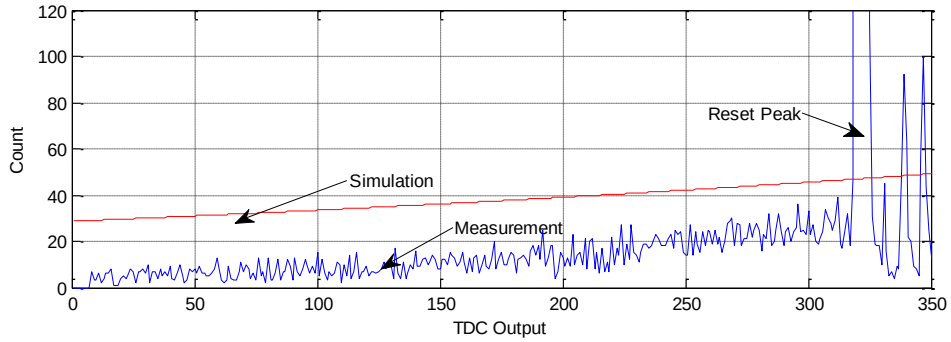

(a) Ambient Light

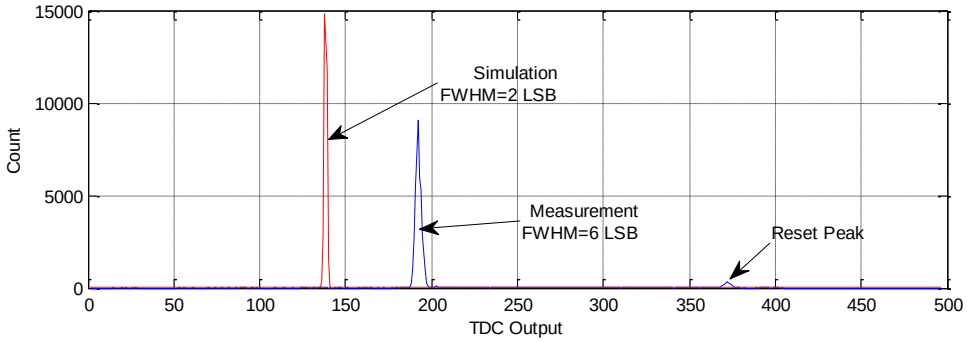

(b) Laser Signal

Figure B.6: TCSPC Model Verification

Signal and Noise Optical Information

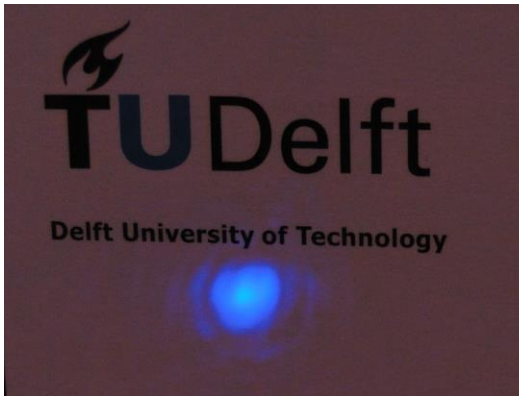

Figure C.1: Laser Spot

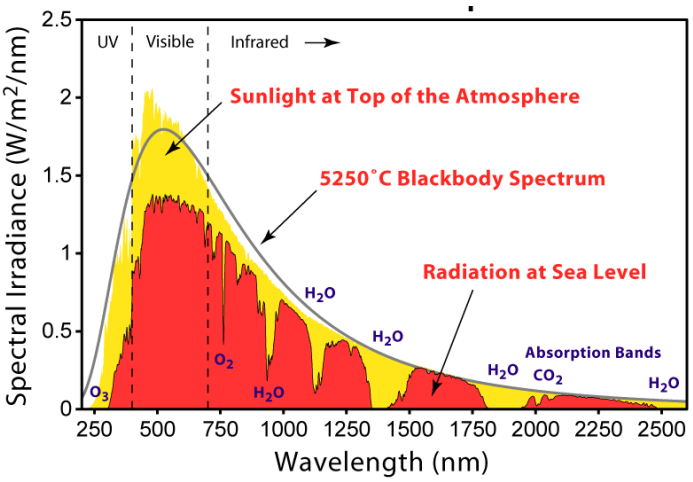

Figure C.2: Solar Spectrum [31]

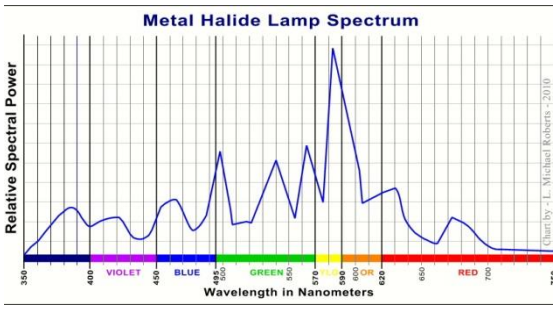

(a) Spectrum of MH Lamps [32]

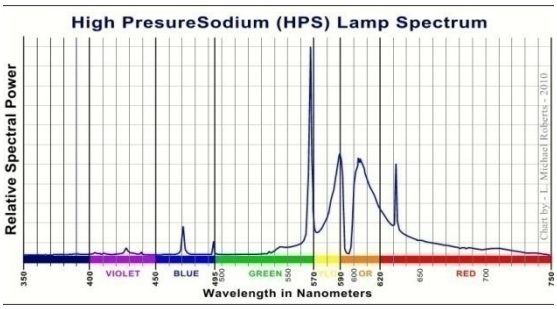

(b) Spectrum of HPS Lamps [33]

Figure C.3: Spectrums of MH Lamps and HPS Lamps

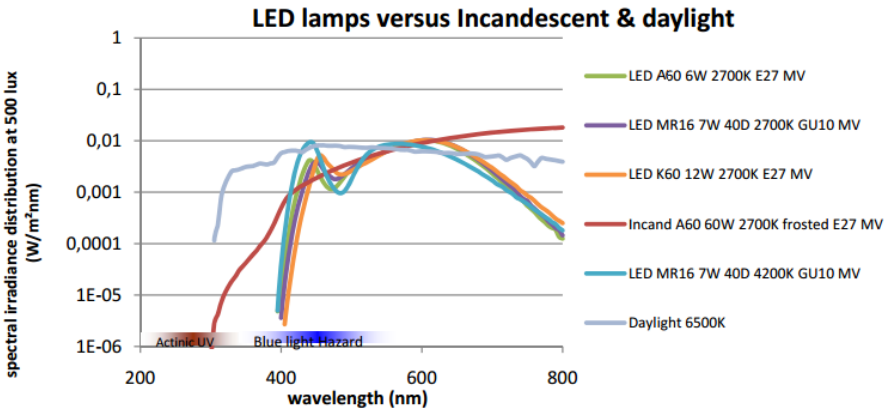

Figure C.4: Spectrum of LED lamps [34]

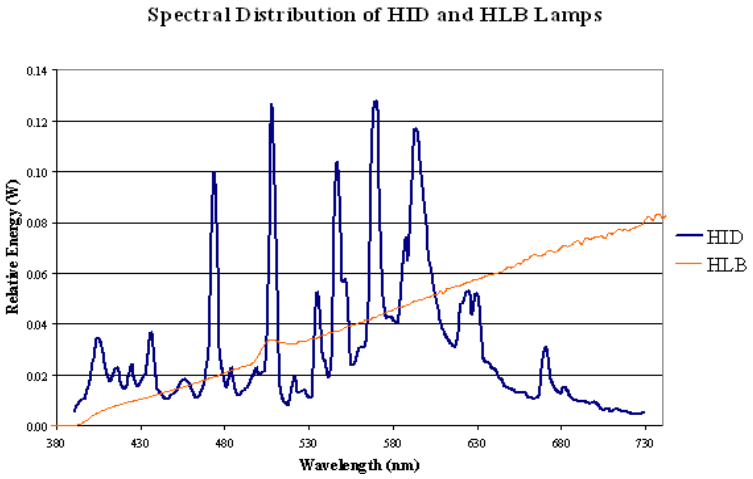

Figure C.5: Spectrum of HID Lamps [35]

Surface Roughness

D

As discussed in Section 2.3.2, model of surface roughness can be divided into height model and slop model. In a height distribution model, height of each point of the surface h is expressed as a random function. Assume that h is normally distributed, with a mean value of 0, and root-mean-square of h or standard deviation σ_{h}, we have

$$h = \frac{1}{\sqrt{2\pi}\sigma_h} e^{-\frac{h^2}{2\sigma_h^2}}. \tag{D.1}$$

This is a simple model, and σ_{h} is popular in industry describing surface roughness. However, this model has its draw back. When two surface share the same mean value and variance, their correlation distances can be different. It means that one model can describe surfaces with different reflection manners. One direct way of solving this problem is to introduce an autocorrelation coefficient

$$C(\tau) = e^{-\frac{\tau^2}{T^2}}, \tag{D.2}$$

with τ the distance between two points, and T the correlation distance.

In modeling of reflection, what people concern more about is the angle that light is reflected, which is determined by the slope of the micro-facets rather than the height. As a result, the model based on slope of the surface is more popular in surface reflection analysis. In this model, normal vector at each point of the surface is considered as random variables. With a given mean angle of α, and a standard deviation of σ_α, we have

$$\rho_\alpha = \frac{1}{\sqrt{2\pi}\sigma_\alpha} e^{-\frac{\alpha^2}{2\sigma_\alpha^2}}. \tag{D.3}$$

We can also draw a relation between height distribution model and slope distribution model. From [24], it is proved that

$$\sigma_\alpha = \frac{1}{\sqrt{2}} tan^{-1} \frac{2\sigma_h}{T}. \tag{D.4}$$

Radiance of Diffused Reflection

E

In [24], Beckmann-Spizzichino model is utilized for specular spike modeling, Torrance -Sparrow model is used for specular spike modeling, Lambertian model is applied in modeling of diffuse lobe.

It is reported that specular spike decreases rapidly when $\sigma_{\mathrm{h}}/\lambda 0.025$. And when $\sigma_{\mathrm{h}}/\lambda 1.5$, specular spike will disappear. For Torrance -Sparrow model, it is stated in the original model that it only valid when $\sigma_{\mathrm{h}}/\lambda 1$. For simplicity, we will neglect specular spike when $\sigma_{\mathrm{h}}/\lambda 1$. When $\sigma_{\mathrm{h}}/\lambda < 1$, we will only consider ideal specular spike. Typical example targets with surface roughness around RMS $\sigma_{\mathrm{h}}=\lambda= 0.405$ μm will be something like burnished metal, plastics spoon, or polyolefin coated paper, etc.

For $\sigma_{\mathrm{h}}/\lambda 1$, according to [24], radiance of reflected light will be

$$L_r = \kappa_{diff} max[0, (L_i d\omega_i cos\theta_i)] + \kappa_{spec} \frac{L_i d\omega_i}{cos\theta_r} e^{-\frac{\alpha^2}{2\sigma_\alpha^2}}, \tag{E.1}$$

with the fraction of incident energy reflected by specular mechanism

$$\kappa_{spec} = \frac{c a_f F' G}{4}, \tag{E.2}$$

$$c = \frac{1}{\sqrt{\frac{\pi}{2}} erf(\frac{\pi}{2\sqrt{2}\sigma_\alpha})}, \tag{E.3}$$

$$G = min[1, \frac{2cos\alpha \cdot cos\theta_i}{cos\theta_i'}], \tag{E.4}$$

with θ_r the reflection angle, θ_i the injection angle, and

$$\theta_i' = \frac{1}{2} cos^{-1}(cos\theta_i \cdot cos\theta_r - sin\theta_i \cdot sin\theta_r). \tag{E.5}$$

It is proved that slope of facet on the target surface α is

$$\alpha == cos^{-1}(cos\theta_i \cdot cos\theta_i' - sin\theta_i \cdot sin\theta_i'). \tag{E.6}$$

Similar as κ_{spec}, κ_{diff} is the fraction of incident energy that are reflected by the diffuse mechanism. It is a 3×3 matrix that describes the absorption characteristics of red, blue, and green light of the surface. For simplicity, we assume that the color either ideal white or black. Such that κ_{diff} becomes a constant, and $\kappa_{\mathrm{diff}}= 1$ or $\kappa_{\mathrm{diff}}= 0$, respectively.

$\mathrm{a_f}$ represents the area of each small facet utilized in the slope model of target surface. α is the angle between the normal vector of these facet and the normal vector of the

surface, with an expected value of 0 and standard deviation of σ_α. $d\omega_i$ is the solid angle from the target to our detector. It can be proved that α=θ_i.

L_i is the radiance of incident light. It is a matrix that describes light radiance of red, green and blue components. Since we are using laser with a well defined wavelength, we can consider it as a constant.

F' is the Fresnel reflection coefficient. With its present, all target can be modeled, including conductors and dielectrics. Also, all kinds of inject light can be modeled. However, since reflection light that falls on our detector is too week, we can make an approximation. In the following simulation, we will replace F' with the total reflectance of the surface at angle θ_i, $R(\theta_i)$.

For $\sigma_h/\lambda < 1$, since we only consider ideal specular spike, according to [24], radiance of reflected light will be

$$L_r = R_0 \cdot L_i. \tag{E.7}$$

In this case, reflected light is limited in a small angle around normal vector of target surface following ideal law of reflection. The angle is determined by laser divergence and target distance.

Average Molecule Mass

F

Relative humidity is defined as

$$RH = \frac{\varepsilon_w}{\varepsilon_w^*} \times 100\%, \tag{F.1}$$

with ε_{w} the partial pressure of water vapor in the mixture, $\varepsilon_{\mathrm{w}}^*$ the saturated vapor pressure of water, which is described as

$$\varepsilon_w^* = (1.0007 + 3.46 \times 10^{-6} P) \times (6.1121) e^{\frac{17.502 T_c}{240.97 + T_c}}, \tag{F.2}$$

with P the total air pressure in hPa, and $\mathrm{T_c}$ the temperature in degrees Celsius.

So partial pressure of H_2O is

$$\varepsilon_{w,H_2O} = RH \cdot \varepsilon_w^*. \tag{F.3}$$

According to Dalton's law of partial pressure, total pressure of a mixture of gases equals to the summation of partial pressure of all individual gases, i.e.

$$\varepsilon_{w,total} = \sum \varepsilon_{w,i}. \tag{F.4}$$

Atmosphere pressure as a function of altitude z is known as

$$p_{at} = 101325(1 - 2.2557 \times 10^{-5} z)^{5.25588}. \tag{F.5}$$

At 2000 m, atmosphere pressure will be 79495 Pa or 596 mmHg.

From Equation F.4, we have

$$p_{at,2000m} = \varepsilon_{w,H_2O} + \varepsilon_{w,O_2} + \varepsilon_{w,N_2}. \tag{F.6}$$

From Equation 2.33, it is clear that when temperature is constant, molecule number of the gas is proportional to the pressure. As a result, we have

$$N_{H_2O} : N_{O_2} : N_{N_2} = \varepsilon_{w,H_2O} : \varepsilon_{w,O_2} : \varepsilon_{w,N_2}. \tag{F.7}$$

In 1 mol air at 2000 m altitude,

$$\frac{N_{H_2O}}{1mol} \times 100\% = \frac{\varepsilon_{w,H_2O}}{p_{at,2000m}} \times 100\%, \tag{F.8}$$

$$\frac{N_{O_2}}{1mol} \times 100\% = \frac{\varepsilon_{w,O_2}}{p_{at,2000m}} \times 100\% = \frac{p_{at,2000m} - \varepsilon_{w,H_2O}}{p_{at,2000m}} \times 20\%, \tag{F.9}$$

$$\frac{N_{N_2}}{1mol} \times 100\% = \frac{\varepsilon_{w,N_2}}{p_{at,2000m}} \times 100\% = \frac{p_{at,2000m} - \varepsilon_{w,H_2O}}{p_{at,2000m}} \times 80\%. \tag{F.10}$$

Finally, we have the average molecule mass of air at 2000 m as

$$m_{2000} = 29.6 - \frac{11.6\varepsilon_{w,H_2O}}{p_{at,2000m}} = 29.6 - \frac{11.6 \cdot RH \cdot \varepsilon_w^*}{p_{at,2000m}}. \tag{F.11}$$

A more general result is

$$m = 29.6 - \frac{11.6 \cdot RH \cdot \{1.0007 + 3.46 \times 10_{-4}[101325(1 - 2.25577 \times 10^{-5}z)^{5.25588}]\}}{101325(1 - 2.25577 \times 10^{-5}z)^{5.25588}} \times 6.1121 \times e^{\frac{17.502(T-273)}{T-32.03}}. \tag{F.12}$$

Atmospheric Transmission

G

For light with 405 nm wavelength, the absorbance is mainly caused by Rayleigh scattering. Rayleigh scattering cross section of 405 nm is $1.6 \times 10^{-26}\ cm^2$ [36]. Ignore the scattering and absorption effect on visible light in the exosphere and the thermosphere. Thickness of atmosphere is about 96.56 km, i.e. sea level to top of mesosphere [37]. For the atmosphere region under study, mean temperature T=250 K, molecular mass $m = 28.964 \times 1.660 \times 10^{-27} = 4.808 \times 10^{-26} kg$, $g = 9.81 m/s^2$, $k = 1.38 \times 10^{-23} J/K$, which yields the atmosphere scaled height

$$H = \frac{kT}{mg} = 7314.5m. \tag{G.1}$$

Substitute Equation G.1 and 2.29 into Equation 2.28, total atmospheric transmission becomes

$$Tr(z) = \prod_{i=1}^{\frac{96.56km}{dz}} e^{-\sigma \cdot dz \cdot N_0 e^{-\frac{izmg}{kT}}}. \tag{G.2}$$

The result is plotted in Figure G.1.

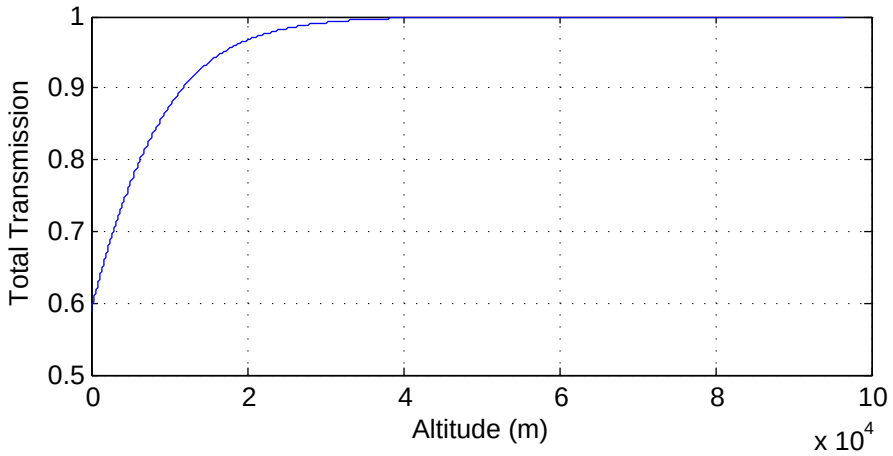

Figure G.1: Atmosphere Transmission Factor Caused by Rayleigh Scattering (λ=405 nm,dz=1m)

Measurement Results

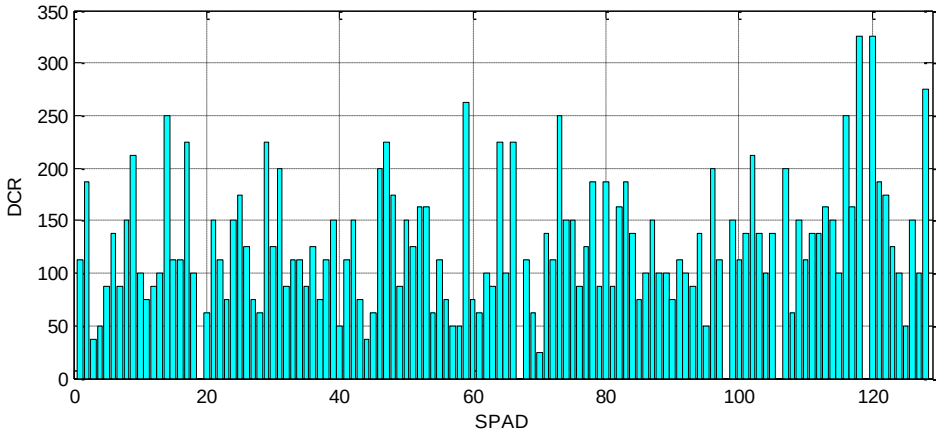

Figure H.1: DCR of All Pixels

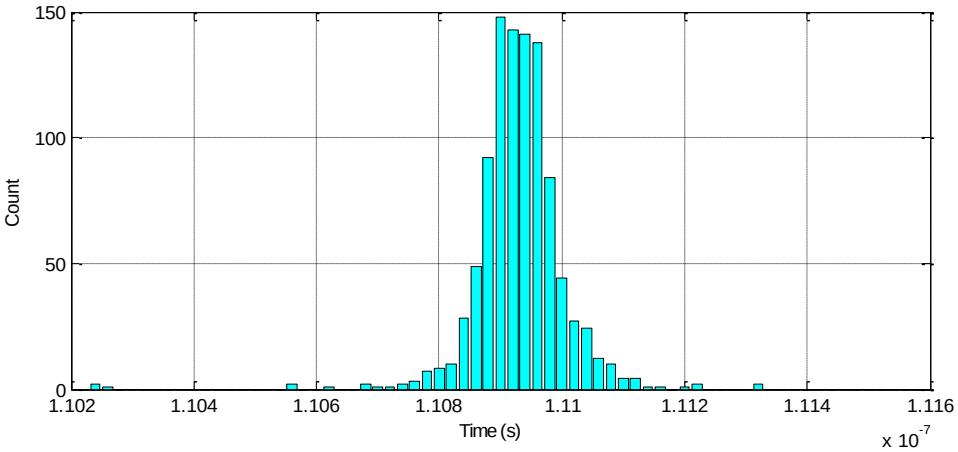

Figure H.2: SPAD Jitter

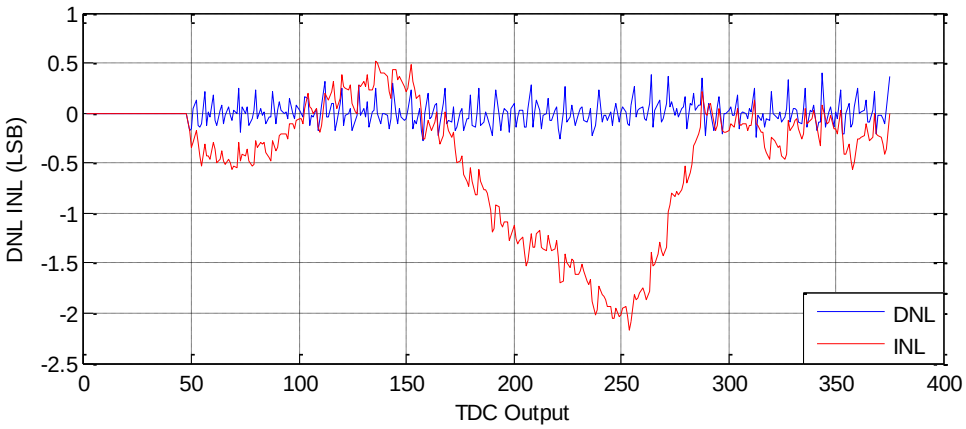

Figure H.3: DNL INL Results of the 43rd TDC

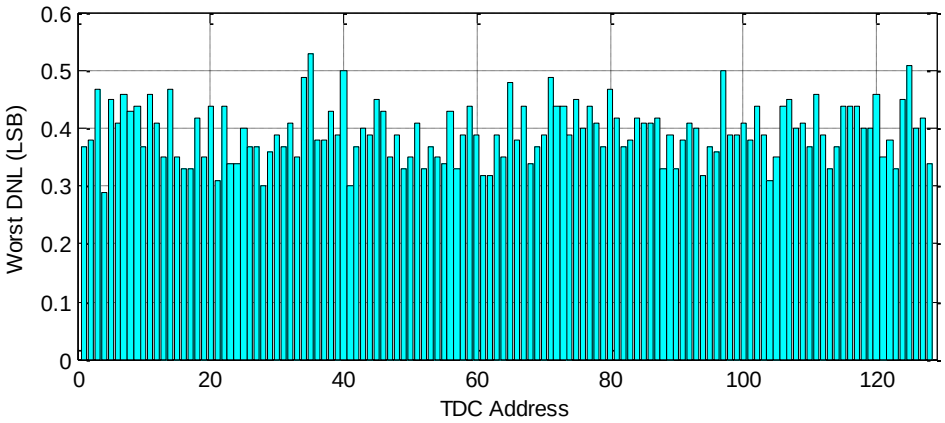

Figure H.4: Worst DNL of All TDCs

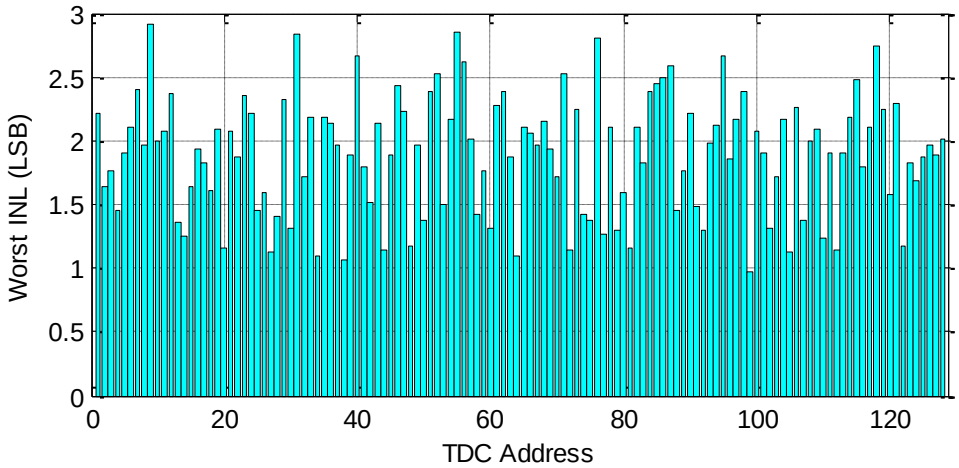

Figure H.5: Worst INL of All TDCs

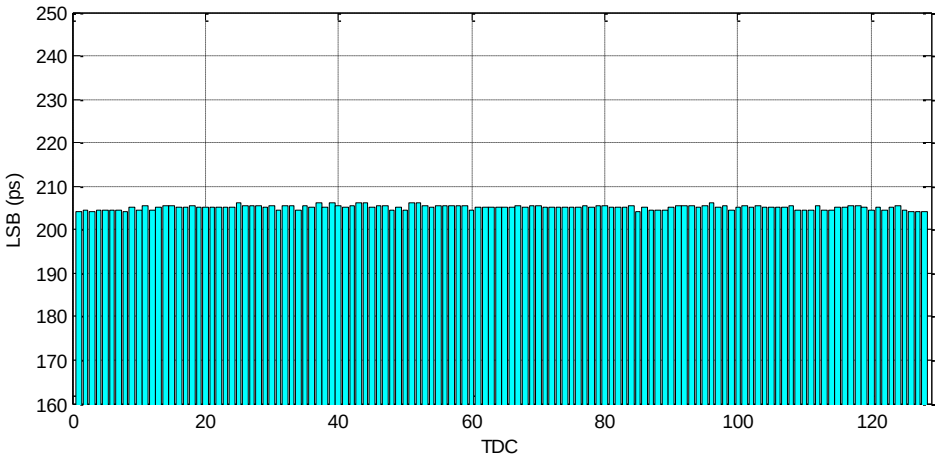

Figure H.6: LSB Estimation of All TDCs

I Measurement Setup

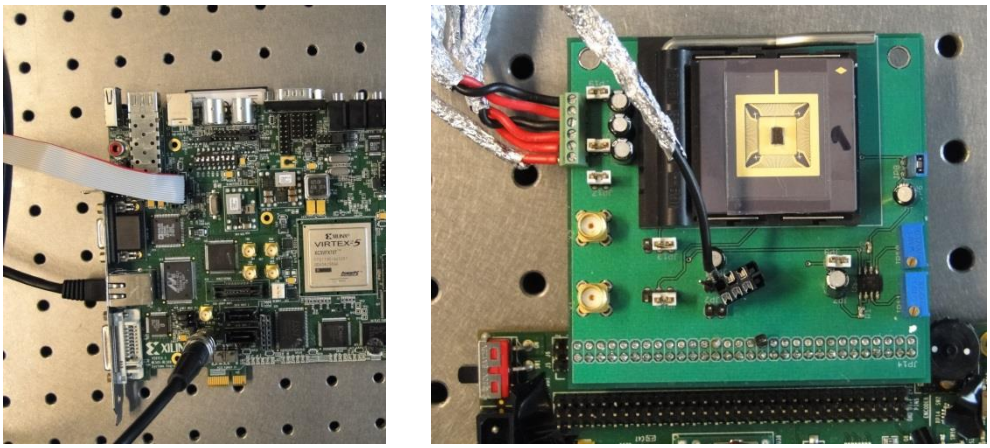

(a) (b)

Figure I.1: Set-up of FPGA Board (a) and Sensor PCB (b)

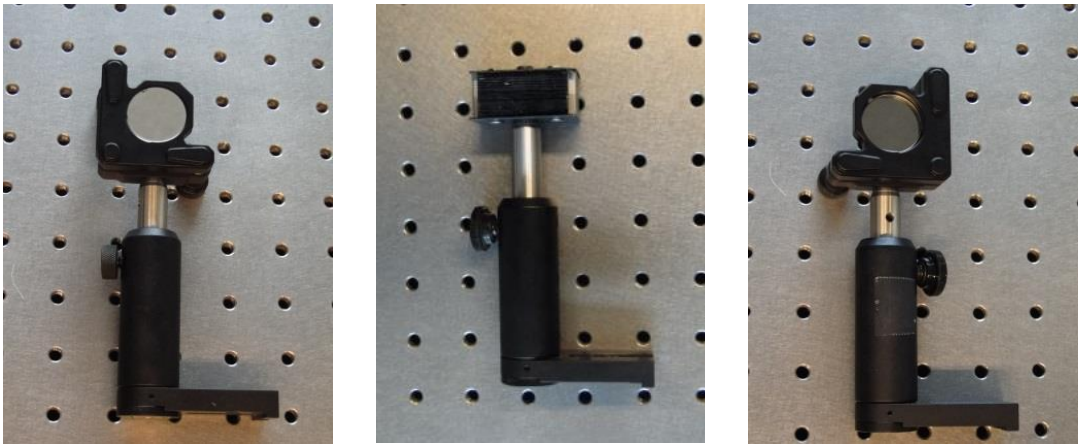

(a) (b) (c)

Figure I.2: Optical Elements Used in the Set-up: (a) the Mirror, (b) the Dark Absorber, and (c) the Neutral Density Filter

(a) (b)

Figure I.3: Set-up of Short-distance Range Detection: (a) 20 cm to 170 cm Range, (b) 170 cm to 300 cm Range

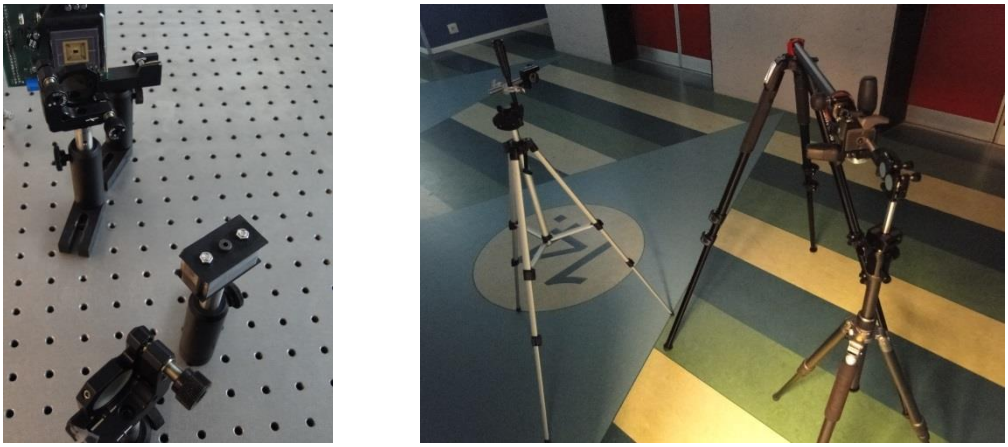

(a) (b)

Figure I.4: Set-up of Long-distance Range Detection: (a) On Optical Table, (b) Tripods

Mechanical Design

J

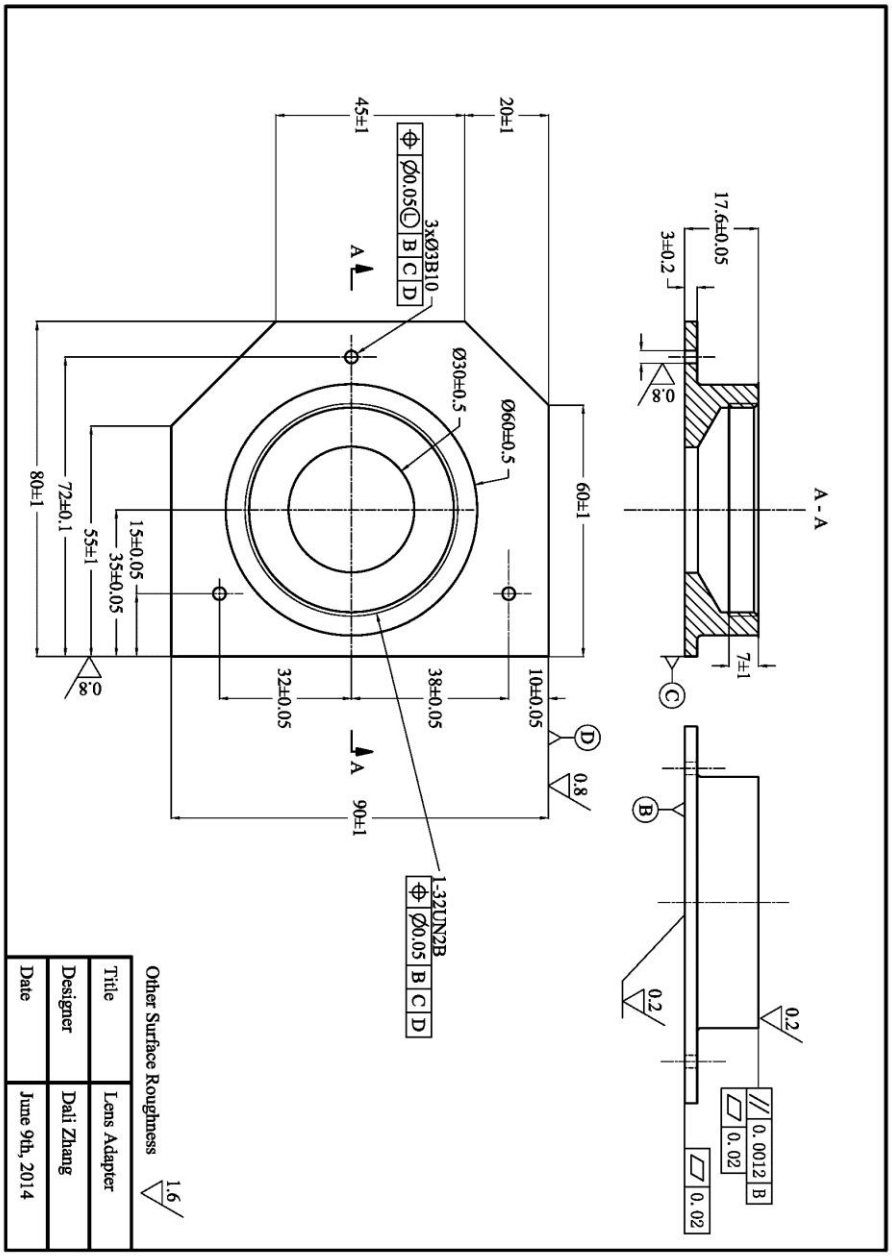

Figure J.1: Lens Adapter

Bibliography

[1] Martin S Banks, Richard N Aslin, and Robert D Letson. Sensitive period for the development of human binocular vision. *Science*, 190(4215):675–677, 1975.

[2] Nick Pears, Yonghuai Liu, and Peter Bunting. *3D imaging, analysis and applications*. Springer, 2012.

[3] François Blais. Review of 20 years of range sensor development. *Journal of Electronic Imaging*, 13(1), 2004.

[4] C. Niclass, E. Charbon, M. Soga, and H. Yanagihara. Pulsed light optical rangefinder, March 29 2012. US Patent App. 13/376,336.

[5] Harmen Menninga, Claudio Favi, Matthew W Fishburn, and Edoardo Charbon. A multi-channel, 10ps resolution, fpga-based tdc with 300ms/s throughput for open-source pet applications. In *Nuclear Science Symposium and Medical Imaging Conference (NSS/MIC), 2011 IEEE*, pages 1515–1522. IEEE, 2011.

[6] J Kittler, A Hilton, M Hamouz, and J Illingworth. 3d assisted face recognition: A survey of 3d imaging, modelling and recognition approachest. In *Computer Vision and Pattern Recognition-Workshops, 2005. CVPR Workshops. IEEE Computer Society Conference on*, pages 114–114. IEEE, 2005.

[7] Andreas Koschan, Marc Pollefeys, and Mongi Abidi. *3D imaging for safety and security*, volume 35. Springer, 2007.

[8] G Yahav, GJ Iddan, and D Mandelboum. 3d imaging camera for gaming application. In *Consumer Electronics, 2007. ICCE 2007. Digest of Technical Papers. International Conference on*, pages 1–2. IEEE, 2007.

[9] Guy Godin, J-Angelo Beraldin, John Taylor, Luc Cournoyer, Marc Rioux, Sabry El-Hakim, Réjean Baribeau, François Blais, Pierre Boulanger, Jacques Domey, et al. Active optical 3d imaging for heritage applications. *IEEE Computer Graphics and Applications*, 22(5):24–36, 2002.

[10] Cristiano L. Niclass. *Single-photon image sensors in CMOS*. PhD thesis, STI, Lausanne, 2008.

[11] Giovanna Sansoni, Marco Trebeschi, and Franco Docchio. State-of-the-art and applications of 3d imaging sensors in industry, cultural heritage, medicine, and criminal investigation. *Sensors*, 9(1):568–601, 2009.

[12] Olaf Gietelink, Jeroen Ploeg, Bart De Schutter, and Michel Verhaegen. Development of advanced driver assistance systems with vehicle hardware-in-the-loop simulations. *Vehicle System Dynamics*, 44(7):569–590, 2006.

[13] Karel A Brookhuis, Dick De Waard, and Wiel H Janssen. Behavioural impacts of advanced driver assistance systems–an overview. *European Journal of Transport and Infrastructure Research*, 1(3):245–253, 2001.

[14] Muhammad Akhlaq, Tarek R Sheltami, Bo Helgeson, and Elhadi M Shakshuki. Designing an integrated driver assistance system using image sensors. *Journal of Intelligent Manufacturing*, 23(6):2109–2132, 2012.

[15] Aongus McCarthy, Robert J Collins, Nils J Krichel, Verónica Fernández, Andrew M Wallace, and Gerald S Buller. Long-range time-of-flight scanning sensor based on high-speed time-correlated single-photon counting. *Applied optics*, 48(32):6241–6251, 2009.

[16] Sijing Chen, Dengkuan Liu, Wenxing Zhang, Lixing You, Yuhao He, Weijun Zhang, Xiaoyan Yang, Guang Wu, Min Ren, Heping Zeng, et al. Time-of-flight laser ranging and imaging at 1550 nm using low-jitter superconducting nanowire single-photon detection system. *Applied optics*, 52(14):3241–3245, 2013.

[17] Shingo Mandai and Edoardo Charbon. A 128-channel, 8.9-ps lsb, column-parallel two-stage tdc based on time difference amplification for time-resolved imaging. *Nuclear Science, IEEE Transactions on*, 59(5):2463–2470, 2012.

[18] A. Ravi, O. Degani, H.S. Kim, H. Lakdawala, Y.W. Li, and P. Madoglio. Sub-picosecond resolution segmented re-circulating stochastic time-to-digital converter, March 5 2013. US Patent 8,390,349.

[19] Aongus McCarthy, Nils J Krichel, Nathan R Gemmell, Ximing Ren, Michael G Tanner, Sander N Dorenbos, Val Zwiller, Robert H Hadfield, and Gerald S Buller. Kilometer-range, high resolution depth imaging via 1560 nm wavelength single-photon detection. *Optics express*, 21(7):8904–8915, 2013.

[20] Kota Ito, Cristiano Niclass, Isao Aoyagi, Hiroyuki Matsubara, Mineki Soga, Satoru Kato, Mitsutoshi Maeda, and Manabu Kagami. System design and performance characterization of a mems-based laser scanning time-of-flight sensor based on a 256 64-pixel single-photon imager. *Photonics Journal, IEEE*, 5(2):6800114–6800114, 2013.

[21] C. Niclass, M. Soga, H. Matsubara, M. Ogawa, and M. Kagami. A 0.18 μm cmos soc for a 100-m-range 10-frame/s 200×96-pixel time-of-flight depth sensor. *Solid-State Circuits, IEEE Journal of*, 49(1):315–330, Jan 2014.

[22] Cristiano Niclass, Maximilian Sergio, and Edoardo Charbon. A single photon avalanche diode array fabricated in 0.35-μm cmos and based on an event-driven readout for tcspc experiments. In *Optics East 2006*, pages 63720S–63720S. International Society for Optics and Photonics, 2006.

[23] Advanced Laser Diode Systems A.L.S. GmbH. Picosecond injection laser (fast pilas) owner's manual, 2004.

[24] Shree K Nayar, Katsushi Ikeuchi, and Takeo Kanade. Surface reflection: physical and geometrical perspectives. *IEEE transactions on pattern analysis and machine intelligence*, 13(7):611–634, 1991.

[25] New Zealand Institute of Chemistry. The surface coating of car bodies. `http://nzic.org.nz/ChemProcesses/polymers/10F.pdf`. Accessed: 2013-10-17.

[26] Andrew M Davis. *Meteorites, Comets, and Planets: Treatise on Geochemistry*, volume 1. Elsevier, 2005.

[27] William Ross McCluney. *Introduction to radiometry and photometry*. Artech House, 1994.

[28] Claus Fröhlich. Total solar irradiance observations. *Surveys in geophysics*, 33(3-4):453–473, 2012.

[29] Intertek. Energy related products: Street and office lighting 245/2009 implementing measure. ErP DirectiveREG. 2009.

[30] Shingo Mandai. Design document. 2010-11-11.

[31] Wikipedia. Sunlight. `http://en.wikipedia.org/wiki/Sunlight.` Accessed: 2013-09-27.

[32] L. Michael Roberts. Metal halide lamp spectrum. `http://i239.photobucket.com/albums/ff17/mattweiland/Metal_Halide_Lamp_Spectrum.jpg.` Accessed: 2013-09-30.

[33] L. Michael Roberts. High presuresodium (hps) lamp spectrum. `http://i239.photobucket.com/albums/ff17/mattweiland/High_Pressure_Sodium_Lamp_Spectrum.jpg.` Accessed: 2013-09-30.

[34] European Lamp Companies Federation. Opticalsafety of led lighting. 1st Edition, July, 2011.

[35] MF Trentacoste. Comparison of near infrared, far infrared, and halogen headlamps on object detection in nighttime rain. *U.S. Department of Transportation*, 2005.

[36] Richard B Miles, Walter R Lempert, and Joseph N Forkey. Laser rayleigh scattering. *Measurement Science and Technology*, 12(5):R33, 2001.

[37] NASA. Earth atmosphere. `http://www.grc.nasa.gov/WWW/k-12/airplane/atmosphere.html`. Accessed: 2013-10-19.